The Dissertation Committee for Dongbing Shao Certifies that this is the approved version of the following dissertation:

Sub-wavelength Optical Phenomena and Their Applications in Nano-fabrication

Committee:

Shaochen Chen, Supervisor

Sanjay Banerjee

John Howell

Li Shi

Gennady Shvets

Sub-wavelength Optical Phenomena and Their Applications in Nano-Fabrication

by

Dongbing Shao, B.E.; M.S.

Dissertation

Presented to the Faculty of the Graduate School of
The University of Texas at Austin
in Partial Fulfillment
of the Requirements
for the Degree of

Doctor of Philosophy

The University of Texas at Austin
December 2006

Dedication

To my parents and family

Acknowledgements

First, I would like to express sincere thanks to my supervisor, Professor Shaochen Chen for his guidance and support during my study at UT. I would especially thank him for his encouragement, understanding and open-mindedness. Without his support and help, my PhD study would not be successful and enjoyable.

My appreciations also go to all the committee members, Professors Sanjay Banerjee, John Howell, Li Shi and Gennady Shvets for serving on my dissertation committee and providing advices on my research. I would like to especially thank Professor John Howell and Li Shi for their help in getting my financial aids. Also, I am very thankful to Professor Li Shi for helpful discussion in some of my projects.

It has been a great pleasure to work with other graduate students in Dr. Chen’s group. My appreciation goes to former lab member Shifeng Li, Senthil Theppakuttai, Mat Hense as well as current member Yi Lu, David Fozard, Leo Han, Arvind Battula and Carlos Aguilar. In particular, I would like to thank Shifeng, Yi and Senthil for their helpful discussion of my projects and David for his help for reading my papers.

I would not have been able to finish my PhD without the love, encouragement, and support from my family. I would like to thank my wife Xueqing for her love, endurance and support. My daughter, Carolyn, has been a source of happiness since her birth. At last, I’m deeply in debt to my parents, sister and brother in China for their support and encouragement to me during every step of my life, especially in the last several years even tracing back to my decision to study abroad.

Sub-wavelength Optical Phenomena and Their Applications in Nano-fabrication

Publication No._____________

Dongbing Shao, Ph.D.
The University of Texas at Austin, 2006

Supervisor: Shaochen Chen

This dissertation presents the numerical study of sub-wavelength optical phenomena and experimental demonstration of their applications in nanoscale patterning.

The optical near-field enhancement associated with sub-wavelength scale nanostructures, such as nano-ridges and nano-tips, were utilized to produce nanoscale patterns. Numerical simulation using finite difference time domain (FDTD) method were employed as a modeling tool to predict and optimize a scheme to achieve parallel patterning by near-field enhanced direct nano-molding. In order to pattern the whole area of the substrate, the laser light was chosen to be transparent to the substrate and was shine from the back with an incident angle. The near-field enhancement facilitates the local ablation to form line or dot patterns on the thin film coated on the substrate. Fabrication process to manufacture the nanostructure used as the mold was also developed.

Further investigation into the near-field enhancement phenomena leads to the study of underlying physics: surface plasmons (SPs) and SP-light coupling. Previous research efforts have shown that transmission through sub-wavelength apertures can be orders of magnitude higher than predicted by aperture theory due to SP-light coupling. In this dissertation study, the SPs excited on the nano apertures were combined with the SPs on the substrate to overcome the two fundamental restraints of light at sub-wavelength scale, transmission and diffraction. The discovery was exploited for nanolithography, coined Surface Plasmon Assisted Nanolithography (SPAN), and one-to-one nanoscale pattern transfer has been achieved using both laser light and UV lamp without losing convenience and simplicity of traditional photolithography technique.

High contrast optical near-field interference generated by SP-light coupling was also studied and combined with the photolithography technique to produce three-dimensional (3D) nanostructures. Different multi-layer 2D/3D periodic polymeric nanostructures have been directly fabricated using such a mechanism in a typical photolithography setup. The nanostructures fabricated can be easily controlled in terms of size, layout, and defects by designing the mask. This so-called Surface Plasmon Assisted 3D Nanolithography (3D-SPAN) was demonstrated in experiments to offer flexible and convenient 3D nanofabrication capabilities.

Table of Contents

List of Tables

List of Figures

Chapter 1: Introduction to Optical Phenomena at Sub-wavelength Scale

The term 'sub-wavelength scale optical phenomena' used in this study is not a very well-defined terminology, but rather referring to a collection of optical/electromagnetic (EM) phenomena that are either having a characteristic dimension smaller than the wavelength of the radiation or are associated with a sub-wavelength scale structure. These two situations, in many cases, are often inter-related and hard to separate. Because the sub-wavelength dimension at visible wavelengths, which range approximately from 400 nm to 700 nm, covers a range from tens of nanometers to several hundred nanometers, these optical phenomena are also often referred as *nano optics*.

The trend of research into nano optics is coincident with the overall trend toward nanoscience and nanotechnology in the current scientific community. This trend is motivated by the fact that as we move to smaller and smaller scales the underlying physical laws start to change from macroscopic to microscopic and many novel phenomena can be observed. The recent advances in this trend are also partly accelerated by our newly acquired ability to measure, fabricate and manipulate structures having nanometer scale dimensions. Taking the example of this study, different nano characterization tools such as Atomic Force Microscopy (AFM), Scanning Electron Microscopy (SEM) and nano fabrication tools such as Electron Beam Lithography (EBL), Focused Ion Beam (FIB) have been thoroughly used throughout the study.

In the meantime, the advance of nanoscale science and technology also raises the need to extend our optics-based tools and sensing capabilities into the nanometer regime.

Optical microscopy and optical lithography are just two simple examples. Although controlling and manipulating light fields on the nanometer scale have far-reaching impact in many fields such as optical microscopy, optical data storage and optical communication, there are fundamental constraints of light at such scale, namely diffraction and transmission. The study of optical near-field, which is the interaction of optical fields and nanostructures, has shown the possibilities to achieve well-defined nanoscale optical field distributions with many promising applications. Optical near-field has been extensively studied in the last decade mainly due to the development of near-field scanning optical microscopy (NSOM) and related techniques, such as Near-field Raman Spectroscopy. The underlying physics and potential applications are, however, spreading into many areas dealing with the interaction of electromagnetic fields with matter.

The interaction of light and macroscopic material has been a classical field of study in the last several decades [1-2] and many mechanisms have been well understood. For metallic materials, the absorption of optical energy is dominantly by free electrons in the metal, in which electrons are free to move within the metal but are confined to the metal by potential barriers. This theory, despite ignoring the effect of the periodic potential due to the atoms in the crystal, has been quite successful in explaining the optical properties of metals. In dielectric materials and semiconductors, however, the analysis of periodic potential is required, which results in energy band, a continuous range of energy values that an electron may have. The highest filled energy band is called valence band, while the lowest unfilled energy band is called conduction band. The energy difference between the maximum of valence band and the minimum of conduction band is the band gap, which is the minimum energy needed to excite an electron in dielectric or semiconductor material that have direct band gap. The absorption of a photon by an electron is only possible if the electron, after taking up the photon energy and perhaps additional momentum, falls in an allowable energy band.

When a small structure is involved in such light-material interaction, however, new physics come to play. As the structure become smaller and smaller, surface-volume ratio upsurges and surface effects tend to prevail. Such surface optical phenomena, which are usually ignored for macroscopic materials, have their maximum intensity at the interface and decays dramatically as it leaves the surface, which is the reason for the name near-field.

The concepts of near-field and far-field were originated previously in microwave technology. The near-field concept can be understood from solving Maxwell's equations. The electric and magnetic fields around a small element can be described by equations with three components proportional to different powers of r, the distance from the element [3-4]. The component of the field strength proportional to $1/r$ is called the radiation term and represents the energy flowing away from the element. The component proportional to $1/r^2$ is called the induction term. The final component, proportional to $1/r^3$, is called the electrostatic field term and represents the electrical charges in the element. Clearly, the $1/r^2$ and $1/r^3$ terms are more dominant at the near field, or the Fresnel zone, while the $1/r$ term dominates in the far field, or the Fraunhofer zone. There is no exact boundary between the two field regions, and sometimes a transition region between them is used.

Present research in optical near-field is strongly influenced by the development of near-field scanning optical microscopy (NSOM) [5]. Imaging by traditional optical microscopy is based on the principle of the interference of light waves [6]. However any types of interference of waves are imposed a limit coined diffraction limit [6]. One way of delaying such limit is by using waves that have smaller wavelength, such as electron waves. In 1981, a breakthrough was made at IBM's Zurich Laboratory in which imaging of a surface was achieved by detecting a weak electric current flowing between a tip and the surface [7-9]. This so-called Scanning Tunneling Microscopy (STM) technology has since inspired many follow-up studies using different interaction mechanisms, which are termed in general Scanning Probe Microscopy (SPM). In NSOM, which is the combination of SPM and optical field, the strength of local electromagnetic interaction between a specimen and a scanned optical probe tip is mapped to produce a nanometer scale image.

In NSOM, the tip and specimen are at a distance shorter than the optical wavelength, but still far from intrinsic contact. They are also well separated with their electronic state at this distance. However the scattered field reflected from one of them will significantly affect the field of the other. The super-resolution optical microscopy is achieved based on the fact that in the vicinity of matter the near-field of light is composed of both propagating and evanescent fields. Having larger wavevector number, the latter is believed to carry high spatial frequencies information and is the key to overcome the diffraction limit. However the evanescent field remained practically untouched by demonstration or applications until recently.

The performance of NSOM is highly dependent on the optical near-field enhancement factor, which is defined as the maximum local field intensity over incident plane wave intensity. Researches have shown that at certain condition such optical near-field can be orders of magnitude higher than the incident field, depending on many factors. However the dependence of the field enhancement on the parameters is highly nonlinear and hard to predict theoretically. From a modeling point of view, when a light field interacts with structures that have complex geometric features comparable in size to the wavelength of the light, it is not permissible to invoke the assumptions of the classical diffraction theory, which simplify the problem and allow for approximate solutions. In such cases, direct numerical solutions of the governing Maxwell's equations are sought instead. Researchers have been using numerical modeling methods by directly solving Maxwell's equations to qualitatively calculate the enhancement. Among those numerical methods, Finite Difference Time Domain (FDTD) is perhaps the most popular one.

More recently, the discovery of extraordinary transmission through metal films that have sub-wavelength scale holes/apertures has triggered tremendous research interest in the community of optics [10]. The discovered transmission at certain wavelength is orders of magnitude higher than predicted by traditional theory. The concept of Surface Plasmon (SP), which is defined as electromagnetic excitations coupled to the free charges at the surface of a conductive medium, was able to explain such unusual behavior. In fact, SPs can act to significantly strengthen the fields associated with the evanescent waves, and dramatically enhance the transmission. With the help from surface modulation by the sub-wavelength structure, SPs can also interfere with each other or couple to the light, producing interesting and unprecedented optical phenomena.

Sub-wavelength structures are of particular interest to optical scientists. They have characteristic length scales much larger than atomic sizes but smaller compared to the optical wavelength. In a sense, nanostructured materials can be thought of as an intermediate phase between bulk material and individual atoms or molecules. Most optical phenomena involving macroscopic samples can be understood from the classical description based on Maxwell's equations, whilst the light interaction with atoms is generally described by quantum mechanics. In the case of nanostructures, both approaches are used. For the dimension size involved in this dissertation study, quantum effect can often be ignored. In other words, this dissertation is more focused on the study of optical near-field, which is light interaction with sub-wavelength structures, using classical Maxwell's equations. In this dissertation, both numerical simulation and experimental demonstration work were carried out to study the optical near-field associated with metallic nanostructures, aiming at developing convenient novel nanofabrication techniques by use of optical near-field.

In Chapter 2, the details of the FDTD modeling techniques are elaborated. The model developed in Chapter 2 provides a powerful modeling tool to study optical near-field for almost arbitrary complex geometries and is utilized throughout this dissertation study. In the following chapters, optical near-field is exploited for different configurations to achieve nanoscale patterning employing sub-wavelength optical effects. The experimental work is also conducted to demonstrate the findings from the numerical modeling. In Chapter 3, the optical near-field enhancement is applied for direct molding of nanostructures. In Chapter 4, SP-light coupling is studied and a planar nanolithography scheme, coined Surface Plasmon Assisted Nanolithography (SPAN) is developed. In Chapter 5, the SPAN process is extended to achieve 3D nano-fabrication of periodic multilayer nanostructures.

Reference

1. M. Bass, *Laser materials processing,* North-Holland. (New York, N.Y., 1983).
2. I. W. Boyd, *Laser processing of thin films and microstructures: oxidation, deposition, and etching of insulators*, Springer-Verlag. (Berlin; New York, 1987).
3. J. D. Kraus, *Antennas*, McGraw-Hill. (New York,, ed. 1st, 1950).
4. B. Berkowitz, *Basic microwaves,* Hayden Book Co. (New York, 1966).

5. E. Betzig, J. K. Trautman, "Near-Field Optics - Microscopy, Spectroscopy, and Surface Modification Beyond the Diffraction Limit," *Science*, **257**, pp.189-195 (1992).
6. M. Born, E. Wolf, *Principles of optics; electromagnetic theory of propagation, interference and diffraction of light*, Macmillan. (New York,1964).
7. G. Binnig, H. Rohrer, C. Gerber, E. Weibel, "Tunneling through a Controllable Vacuum Gap," *Applied Physics Letters*, **40**, pp.178-180 (1982).
8. G. Binnig, H. Rohrer, C. Gerber, E. Weibel, "7x7 Reconstruction on Si(111) Resolved in Real Space," *Physical Review Letters*, **50**, pp.120-123 (1983).
9. G. Binnig et al., "Tunneling Spectroscopy and Inverse Photoemission - Image and Field States," *Physical Review Letters*, **55**, pp.991-994 (1985).
10. T. W. Ebbesen, H. J. Lezec, H. F. Ghaemi, T. Thio, P. A. Wolff, "Extraordinary optical transmission through sub-wavelength hole arrays," *Nature*, **391**, pp.667-669 (1998).

Chapter 2: FDTD Simulation for Nano Optics Study

2.1 MAXWELL'S EQUATIONS

Light is an electromagnetic (EM) wave whose behavior is governed by the famous Maxwell's equations. Although the equations were published by James Clark Maxwell as early as 1873, the powerful equations represent one of the most elegant and concise ways to state the fundamentals of electricity and magnetism. In another word, any EM phenomena could be derived from the fundamental governing equations. Although these equations may have assumptions and limitations, the interesting optical phenomena that fall in the scope of this dissertation study can be predicted by the Maxwell's equations.

The generalized 3D Maxwell's Equations state as following:

$$\nabla \cdot \overline{D} = \rho \qquad (2.1.1)$$

$$\nabla \cdot \overline{B} = 0 \qquad (2.1.2)$$

$$\nabla \times \overline{E} + \frac{\partial \overline{B}}{\partial t} = 0 \qquad (2.1.3)$$

$$\nabla \times \overline{H} - \frac{\partial \overline{D}}{\partial t} = \overline{J} \qquad (2.1.4)$$

where $\overline{E}$ is the electric field vector and $\overline{H}$ is the magnetic field vector. Electric displacement field $\overline{D}$ is defined as $\overline{D} = \varepsilon_0 \overline{E} + \overline{P}$, where ε_0 is the permittivity of free space and $\overline{P}$ the polarization, while the magnetic induction $\overline{B}$ is related to $\overline{H}$ by $\overline{H}$ = $\overline{B} / \mu_0 - \overline{M}$, where μ_0 is the permeability of free space and $\overline{M}$ the magnetization. Also in equation (2.1), ρ is the free electric charge density and $\overline{J}$ the current density.

For the ordinary media, which are linear and isotropic, one can assume $\overline{D} = \varepsilon \overline{E}$, $\overline{B} = \mu \overline{H}$ and $\overline{J} = \sigma \overline{E}$, where the constants ε, μ and σ are permittivity, permeability and conductivity of the material respectively. Due to the fact that equation (2.1.2) is automatically satisfied considering the mathematical transformation of equation (2.1.3) and equation (2.1.1) is only useful to obtain ρ after $\overline{E}$ is solved, we are usually only interested in the simplified Maxwell's equations in the following form, which involves 6 unknowns and 6 equations in 3D.

$$\nabla \times \overline{E} + \mu \frac{\partial \overline{H}}{\partial t} = 0 \tag{2.2.1}$$

$$\nabla \times \overline{H} - \varepsilon \frac{\partial \overline{E}}{\partial t} = \sigma \overline{E} \tag{2.2.2}$$

Now the problem seems simple as long as we can solve the governing equations. However, the Maxwell's equations are complex differential equations, where electric and magnetic fields are coupled. To find an analytical solution is impossible for many cases. Alternatively, numerical results are often sought. In this chapter, I will first review the computational techniques used in electromagnetism. Then, details of modeling approach will be given to the method that I used for my PhD study, which is called the Finite Difference Time Domain (FDTD) method.

2.2 OVERVIEW OF NUMERICAL METHODS FOR NANO-OPTICS STUDY

Because of the needs and difficulties of solving Maxwell's equations numerically, a division of research, called computational electromagnetism, has boomed since 1960s. There have been perhaps more than tens of methods being developed and widely used, each with pros and cons. In this section, a few examples of them are briefly reviewed here.

2.2.1 Multiple multipole method

The multiple multipole method (MMM) [1-2] was developed based on the generalization of Mie theory. The Mie theory provides rigorous solutions for light scattering by an isotropic sphere embedded in a homogeneous medium. In the MMM method, EM fields are represented by a series expansion of the analytical solutions of Maxwell's equations. The fields are forced to fulfill the boundary conditions by choosing appropriate coefficients in the series expansion at discrete points at the interface between adjacent homogeneous domains. The final solution is represented by a self-consistent analytical expression. Although the Mie theory is restricted to spherical, homogeneous, isotropic and non-magnetic particles in a non-absorbing medium, there have been many research efforts to enhance MMM for other types of geometry and materials. On the other hand, MMM algorithm trades complexity for exactness and specified accuracy can be achieved in the algorithm.

2.2.2 Method of moments

The method of moments (or moment method) [3] solves complex integral equations by reducing them to a system of linear equations. It employs a technique known as the method of weighted residuals, which is the origin of the name of this method.

The key step in weighted residual techniques is the calculation of residuals, which is the difference between the true solution and a set of trial solution functions with variable parameters. By minimizing the residuals, the variable parameters are determined to ensure a best fit of the trial functions. The equation solved by moment method techniques is generally of integral forms, which can be derived from Maxwell's equations by considering the scattering by a perfect conductor (or a lossless dielectric).

2.2.3 Rigorous coupled wave analysis (RCWA)

The RCWA, also known as the Fourier modal method, is an efficient tool for the numerical analysis of optical diffraction from 2D binary grating structures [4]. The RCWA method starts with Fourier transformation of both the dielectric functions of the material and the EM fields. It then calculates the grating modes as eigenvectors and matches the fields at the interface of the gratings to fulfill the boundary conditions.

2.2.4 Finite element method (FEM)

FEM method is a widely used computation method in many areas of engineering fields for complex nonlinear problems. FEM analysis first divides the computational domain into many pieces of small homogeneous pieces, called elements. In each element, a simple linear or higher order variation of the field quantity is assigned, and the goal of the FEM analysis is to determine the field quantities at the corners of each element by minimizing an energy function. The energy function describes all the energy associated with the specific configuration. For example, for EM problems, the energy function consists of the energy stored in the electric and magnetic fields, as well as the energy in conduction current. The recent advances in FEM algorithm have made it practical for solving 3D EM problems [5-6].

2.2.5 FDTD method overview

FDTD method is perhaps the most straightforward numerical method to solve the Maxwell’s equations. It uses a time stepping procedure and simple central-difference approximations to evaluate the time and spatial derivatives. Originally, the FDTD method was not favored by the scientists and researchers because the method requires a very large amount of storage space for the unknowns at all the grid points in the computational domain. In 1966, Yee [7] proposed an elegant discretizing algorithm, in which the electric field grids are offset from magnetic field grids in both time and space. With such configuration, the present EM fields are updated in a leap-frog scheme from their past values and the storage needs for the variables are significantly reduced. Later on, the advances in both computer technology as well as the FDTD algorithms have made FDTD perhaps the most popular numerical method in solving EM problems.

Compared to other numerical techniques, FDTD method has the following merits. First, unlike most other techniques, FDTD techniques work in the time domain. This makes them well-suited to transient analysis problems. Secondly, the FDTD method is very good at modeling complex inhomogeneous configurations, similar to finite element method. The ability to easily deal with complex geometrical features and different material properties is of crucial importance to our study. Thirdly, the advances in FDTD algorithm have made it convenient and efficient to model open-space problems, which is also very important for our studies. Last, but not least, the FDTD method directly solves the Maxwell's equations without any assumptions. Those optical phenomena associated with the sub-wavelength structure will be directly reflected in the FDTD simulation results.

2.3 FINITE DIFFERENCE TIME DOMAIN (FDTD) METHOD

In this section, the details of our FDTD algorithm will be discussed.

As implied by the name, the FDTD method is a mesh grid based finite difference method and it became practical only after Yee's elegant discretizing algorithm, which is illustrated in figure 2-1. The electric (magnetic) fields are updated from their previous values with the neighboring magnetic (electric) fields. The offset of the electric field node to the magnetic field node eliminates redundant variables and the memory storage requirement is reduced.

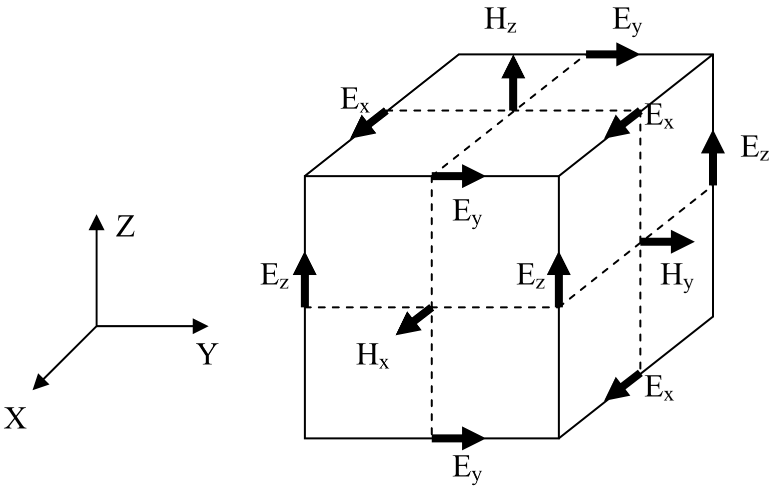

Figure 2-1: Illustration of discretization in Yee's algorithm

The grid size is usually uniform across the computational domain. In order to stabilize the iteration, the grid size Δ is has to be 1/20 of the wavelength λ and the time step τ on the order of Δ/c, where c is the speed of light in free space. From this, one can be clear that the wavelength and the size of the object to be simulated have to be comparable so that both the memory requirement and the number of iteration steps are reasonable. Originally, the FDTD method was used in microwave engineering and had very successful applications. The wavelengths of microwaves are on the order of centimeters and are smaller but comparable to the size of the objects such as, for example, an antenna. In the past, however, the FDTD method was seldom used in solving optical problems due to the simple fact that the optical wavelength is orders of magnitude smaller than the size of macro or even millimeter objects. In my study, fortunately, we are interested in sub-wavelength scale structures and thus the whole computational domain can be just a few microns. It turns out that the FDTD method is a useful and powerful tool for my study of sub-wavelength optical phenomena.

2.3.1 Two dimensional TM mode FDTD discretizing scheme

Although the FDTD method is the right tool for my research, the coding of FDTD method at 3D would be troublesome. Fortunately, many sub-wavelength optical phenomena that I studied can be simplified to 2D. In 2D, there are basically two polarization modes. The first one is transverse electric (TE) mode, where the electric field is perpendicular to the plane of propagation, while in transverse magnetic (TM) mode the electric field is always in the plane of propagation. Figure 2-2 illustrates the two modes. Interestingly, the phenomena of interest, such as near-field enhancement and surface plasmon coupling with light, are only present in the TM mode configuration. The reason for that will be explained in later chapters.

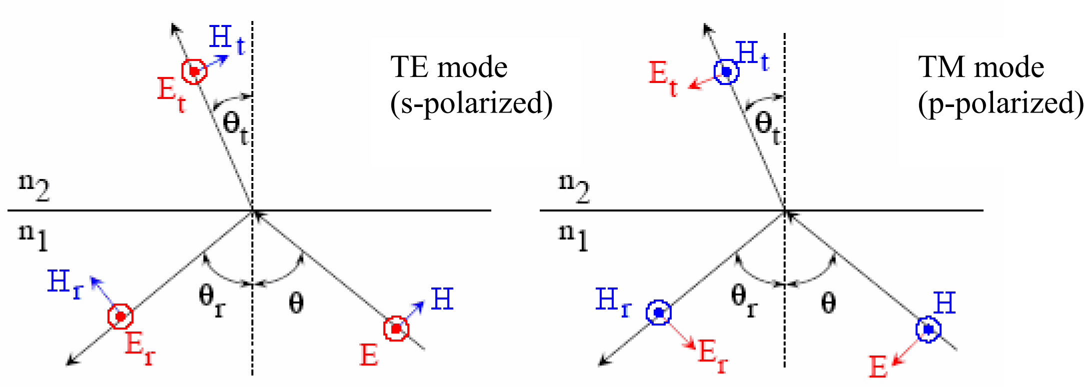

Figure 2-2: Illustration of TE and TM polarizations.

Based on above discussion, a 2D TM mode FDTD code is developed for the study. For 2D TM mode, the Maxwell's equations reduce to:

$$\mu\frac{\partial H_z}{\partial t} = -(\frac{\partial E_y}{\partial x} - \frac{\partial E_x}{\partial y}) \tag{2.3.1}$$

$$\varepsilon\frac{\partial E_x}{\partial t} = \frac{\partial H_z}{\partial y} - \sigma E_x \tag{2.3.2}$$

$$\varepsilon\frac{\partial E_y}{\partial t} = -\frac{\partial H_z}{\partial x} - \sigma E_y \tag{2.3.3}$$

The first order discretization of equations (2.3) gives:

$$H_z^{n+1}(i,j) = H_z^n(i,j) - \frac{\tau}{\mu}\left[\frac{E_y^n(i+1,j) - E_y^n(i,j)}{\Delta} - \frac{E_x^n(i,j+1) - E_x^n(i,j)}{\Delta}\right] \tag{2.4.1}$$

$$E_x^{n+1}(i,j) = \frac{\varepsilon/\tau - \sigma/2}{\varepsilon/\tau + \sigma/2}E_x^n(i,j) + \left[\frac{H_z^n(i,j) - H_z^n(i,j-1)}{\Delta(\varepsilon/\tau + \sigma/2)}\right] \tag{2.4.2}$$

$$E_y^{n+1}(i,j) = \frac{\varepsilon/\tau - \sigma/2}{\varepsilon/\tau + \sigma/2}E_y^n(i,j) - \left[\frac{H_z^n(i,j) - H_z^n(i-1,j)}{\Delta(\varepsilon/\tau + \sigma/2)}\right] \tag{2.4.3}$$

2.3.2 Boundary conditions

The ability to simulate open boundary problems, such as scattering of light by a particle, was one of the challenges that FDTD method had to face. Because Maxwell's equations are wave equations in nature, a propagating 'digital' wave will eventually come to the edge of the computational domain, which is dictated by the matrices dimensions in the program. Normally, in calculating the E field, we need to know the surrounding H values. However at the edge of the computational domain we will not have the value on one side. Without proper boundary treatment, unpredictable reflections would be generated and the numerical wave would be bounced back into the computational domain due to the iteration algorithm. There would be no way to differentiate the real EM wave that we are interested to study and the artificially reflected one. This is the reason that boundary treatments have been an issue ever since FDTD has been used and many numerical approaches have been proposed for a flexible and efficient Absorbing Boundary Conditions (ABCs) [8-10].

The basic idea of ABC is that, when a plane wave is propagating in medium A and impinges upon medium B, the amount of reflection is dictated by the intrinsic impedances of the two media:

$$\Gamma = (\eta_A - \eta_B)/(\eta_A + \eta_B) \tag{2.5}$$

where the impedance is determined by: $\eta = \sqrt{\mu / \varepsilon}$. For most non magnetic natural materials, μ is a constant. However if we assign an artificial number of μ_{B} according to ε_{B} so that η_{B} is unchanged compared to η_{A}, then Γ would be zero meaning no reflection occurs. This still doesn't solve our problem since the wave will keep propagating in the new medium. However if we make the artificial medium lossy (complex ε with non-zero imaginary part) at the same time, the wave will be absorbed numerically in the medium.

However equation 2.5 is only valid for a plane wave and does not consider the factors such as the angle of incidence and mode of polarization. As a result, the direct implementation of such ABC, although effective, cannot eliminate all the numerical errors. In 1994, Berenger extended further in this approach and proposed the Perfectly Matched Layer (PML) method [11]. In the PML method, the governing Maxwell's equations inside the PML are split into two sets of equations. Such treatment as illustrated in Fig. 2-3, although has no physical meaning, can theoretically absorb EM waves at any frequencies and angles of incidence without reflection when combined with utilizing lossy material properties and matched impedance. The finite-difference implementation of PML requires the conductivities to be turned on gradually over a distance of a few grid points to avoid numerical reflections from the discontinuity.

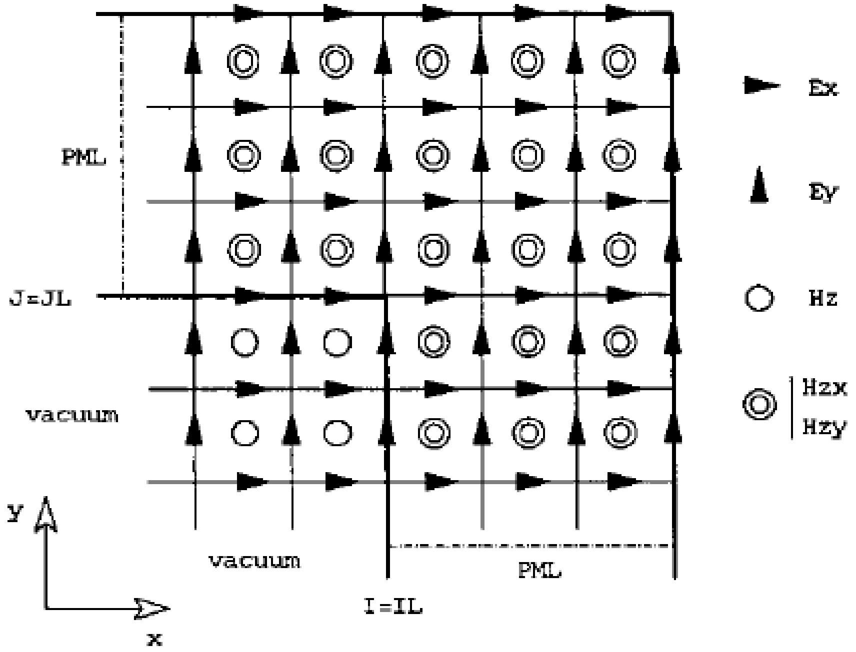

Figure 2-3: Illustration of PML grids at the corner of the computation domain.

As an illustration of the effects, Fig. 2-4 shows the electric field inside the computational domain with different boundary treatments. Figure 2-4(c) shows that the numerical errors inside the computation domain due to the boundary effect are about two orders of magnitude smaller as compared to the case without a boundary treatment (Figure 2-4b). Figure 2-4(d) clearly showed the effect of PML, for if the outgoing wave were partially reflected, the contours would not be concentric.

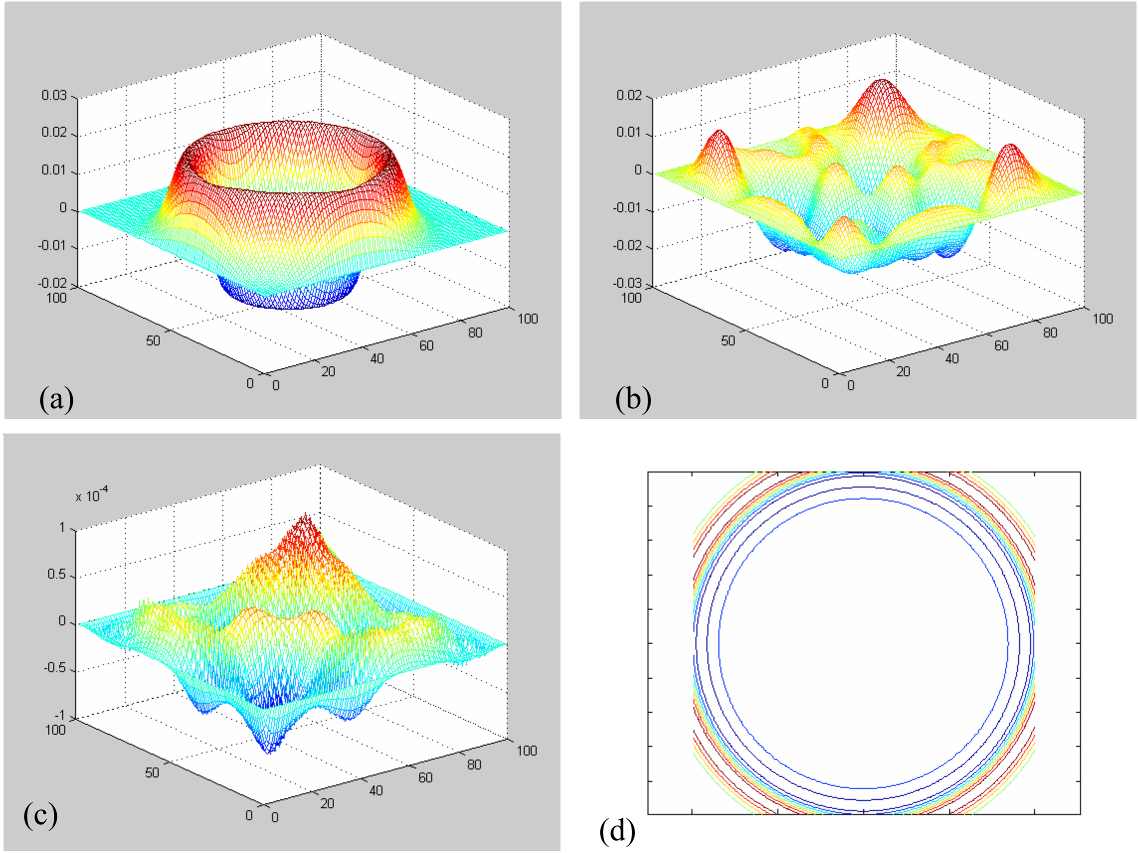

Figure 2-4: (a) Wave from a point source propagating outward; (b) field distribution without boundary treatment; (c) field distribution with ABC; (d) field distribution with PML.

2.3.3 Light source in FDTD

There are basically two types of light sources often used in a FDTD method for the studying of light-material interaction. The first type is just a point source, where a point disturbance, sinusoidal or exponentially decaying as a function of time, is added to the electric field at a certain node. Then this disturbance will propagate outward by the FDTD iteration. The other type is a plane wave light source, which is more useful and of interest in computational electromagnetism. For many instances, especially after a distance on the order of tens of wavelengths from the source, the field can be approximated as a plane wave.

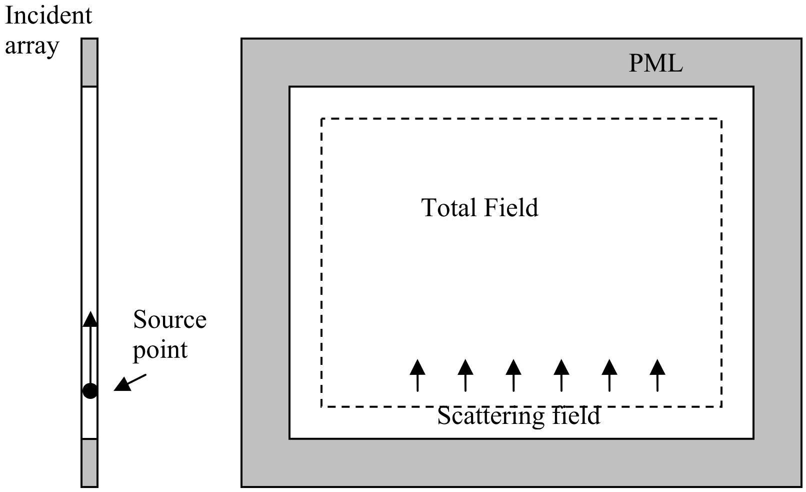

Figure 2-5: Total field and scattered field of the 2D computation domain.

In order to simulate a plane wave, for example in a 2D case, the computational space has to be divided into two regions, the total field and the scattered field, as illustrated in Figure 2-5. The plane wave is only propagating in the total field. The plane wave information is calculated and stored in a one-dimensional buffer called the incident array. The idea is that if a point is in the total field but uses values of points in a scattered field when updating its own value, it must be modified according to the data stored in the incident array and vice versa. The details of the algorithm can be found in literature [8-10]. Figure 2-6 illustrates the propagation of a plane wave of Gaussian pulse through the domain.

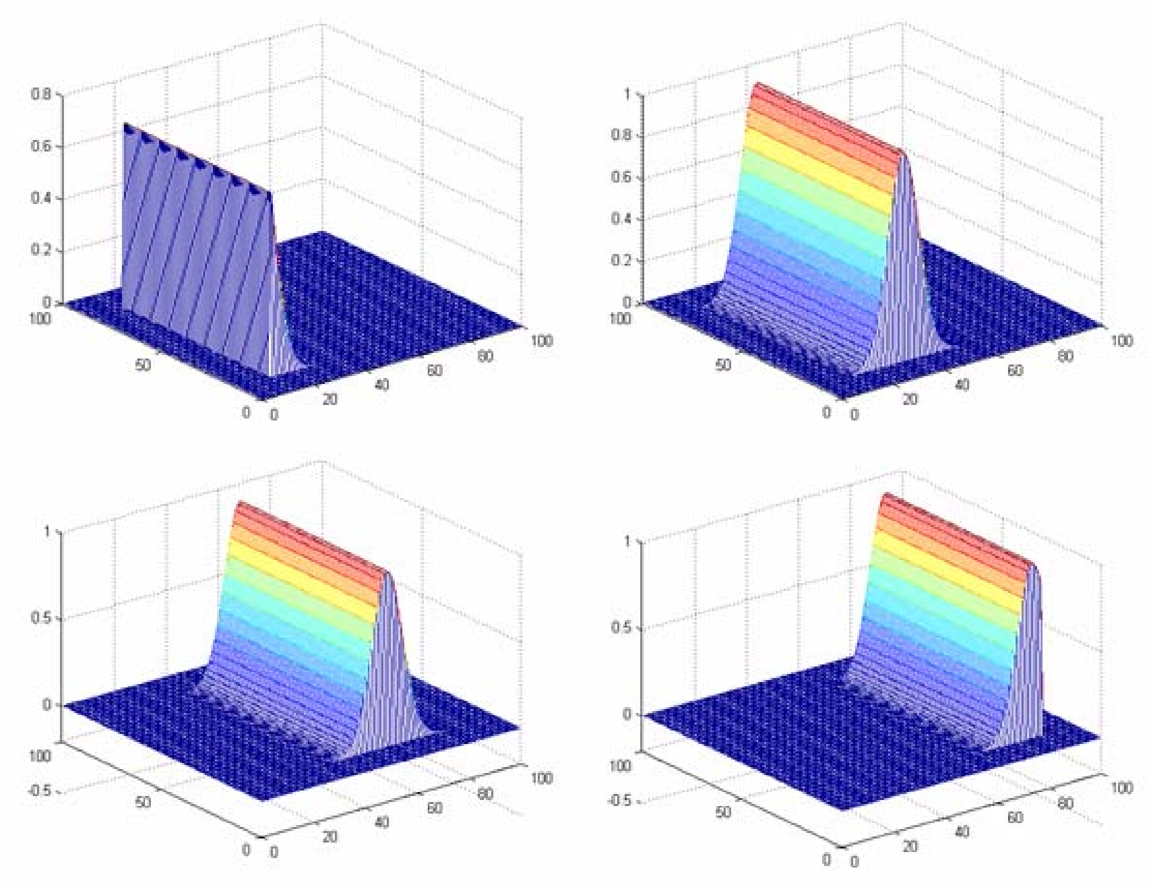

Figure 2-6: Plane wave pulse propagation. The incident pulse is generated at one end and subtracted on the other end.

2.3.4 Drude model

Metals at optical frequencies are characterized with complex dielectric constants. The non-zero imaginary part is associated with absorption and the real part, which is often negative, is associated with high reflectivity. In Chapter 4, these attributes will be explained to stem from the free electrons in metals. A pragmatic problem due to the negative dielectric constant, however, is that it makes the standard time iteration scheme, as shown in equation (2.4), have stability problem during the iterations. An alternative is to introduce current density terms into Maxwell's equation that are formally equivalent upon Fourier transformation to the frequency domain to the use of a complex-valued dielectric constant.

On the other hand, the material properties of most media are frequency dependent. In some cases, people are interested in an EM source of a range of frequencies. For example, a single pulse can contain a spectrum of frequencies. In order to simulate frequency-dependent material, an additional model is needed to account for the effect. In fact, this has been a major field of development in the FDTD method.

People have been introducing different physical models to simulate light interaction with frequency-dependent materials. For example the Derby model [8]:

$$\varepsilon(\omega) = \varepsilon(\infty) + \frac{\sigma}{j\omega\varepsilon_0} + \frac{\chi_1}{1 + j\omega t_0} \tag{2.6}$$

describes a single-pole frequency dependence. The Lorenz model [8], which is a two-pole frequency dependence, expresses as:

$$\varepsilon(\omega) = \varepsilon(\infty) + \frac{\varepsilon_1}{1 + j2\delta_0(\frac{\omega}{\omega_0}) - (\frac{\omega}{\omega_0})^2} \tag{2.7}$$

In 1900, Drude used a spring-mass system considering the resisting force from collision between the positive ions and electrons to describe the dynamics between metal atoms and electrons. Even though simplifications and estimations are present in the model, the formulation model has been proved quite successful at explaining a number of observed phenomena of metals. The Drude model is described as [12]:

$$\varepsilon_D(\omega) = \varepsilon_D(\infty) - \frac{\omega_D^2}{\omega^2 + i\Gamma_D\omega} \tag{2.8}$$

where $\varepsilon_D(\infty)$, ω_D and Γ_D are constants with physical meanings. For example, $\varepsilon_D(\infty)$ is the dielectric constant limit at infinite frequency value and ω_D represents the bulk plasmon frequency. However these parameters do not necessarily have to reflect the true physical values, especially when we simply fit the three parameters to empirical data over a small range of frequencies. In this way, a much more flexible and realistic approximation is obtained. In fact, I used this numerical approach to model optical phenomena involving materials including metal as well as dielectric and low lossy materials. In my study, since we are interested in optical phenomena only at a specific wavelength, the programming for fitting is much simplified. The three parameters are determined by fitting with optical properties of the metals (namely refractive index and extinction coefficient) that are available in literature [13]. An infinite sets of parameters can be obtained that can serve the purpose.

After incorporating the Drude model, the 2D TM mode Maxwell's equations transform to [12]:

$$\mu_0 \frac{\partial H_z}{\partial t} = -(\frac{\partial E_y}{\partial x} - \frac{\partial E_x}{\partial y}) \tag{2.9.1}$$

$$\varepsilon_{eff} \frac{\partial E_x}{\partial t} = \frac{\partial H_z}{\partial y} - J_x \tag{2.9.2}$$

$$\varepsilon_{eff} \frac{\partial E_y}{\partial t} = -\frac{\partial H_z}{\partial x} - J_y \tag{2.9.3}$$

$$\frac{\partial J_x}{\partial t} = \alpha J_x + \beta E_x \tag{2.9.4}$$

$$\frac{\partial J_y}{\partial t} = \alpha J_y + \beta E_y \tag{2.9.5}$$

where $\varepsilon_{\mathrm{eff}}$, α and β are related to Drude model parameters $\varepsilon_D(\infty)$, ω_D and Γ_D given by:

$$\varepsilon_{eff} = \varepsilon_0 \varepsilon_\infty \tag{2.10.1}$$

$$\alpha = -\Gamma_D \tag{2.10.2}$$

$$\beta = \varepsilon_0 \omega_D^2 \tag{2.10.3}$$

2.3.5 Benchmark

Benchmark of the numerical simulation is always needed to make sure the results are reflecting the true physics to avoid numerical errors or even small bugs in the code. In fact, mistakes can be easily made in programming without notice due to many reasons. In this study, I used the theoretical solution of light scattering by a cylinder to benchmark my FDTD modeling. The theoretical solution of internal electric fields (within the cylinder) can be expressed in cylindrical coordinates and it takes the form as below [14]:

$$E_r^{\text{int}}(nkr) = -\frac{E_0}{n^2 kr} \sum_{m=-\infty}^{\infty} i^m c_m m J_m(nkr) e^{im\phi} \tag{2.11.1}$$

$$E_\phi^{\text{int}}(nkr) = -\frac{iE_0}{n} \sum_{m=-\infty}^{\infty} i^m c_m J_m^{'}(nkr) e^{im\phi} \tag{2.11.2}$$

$$c_m = \frac{1}{J_m(nx)}[J_m(x) - a_m H_m^{(1)}(x)] \tag{2.11.3}$$

$$a_m = \frac{J_m^{'}(nx) J_m(x) - n J_m(nx) J_m^{'}(x)}{J_m^{'}(nx) H_m^{(1)}(x) - n J_m(nx) H_m^{'(1)}(x)} \tag{2.11.4}$$

The comparison of results from my FDTD simulation and theoretical solution were made for different materials and size. Even though we have to use a zigzagged geometry in the grids to approximate a circular shape, the comparison showed a satisfactory match between the two, as illustrated by an example in Figure 2-7. After benchmarking, the code can be used with confidence to model optical field distribution involving different complex geometries and structures.

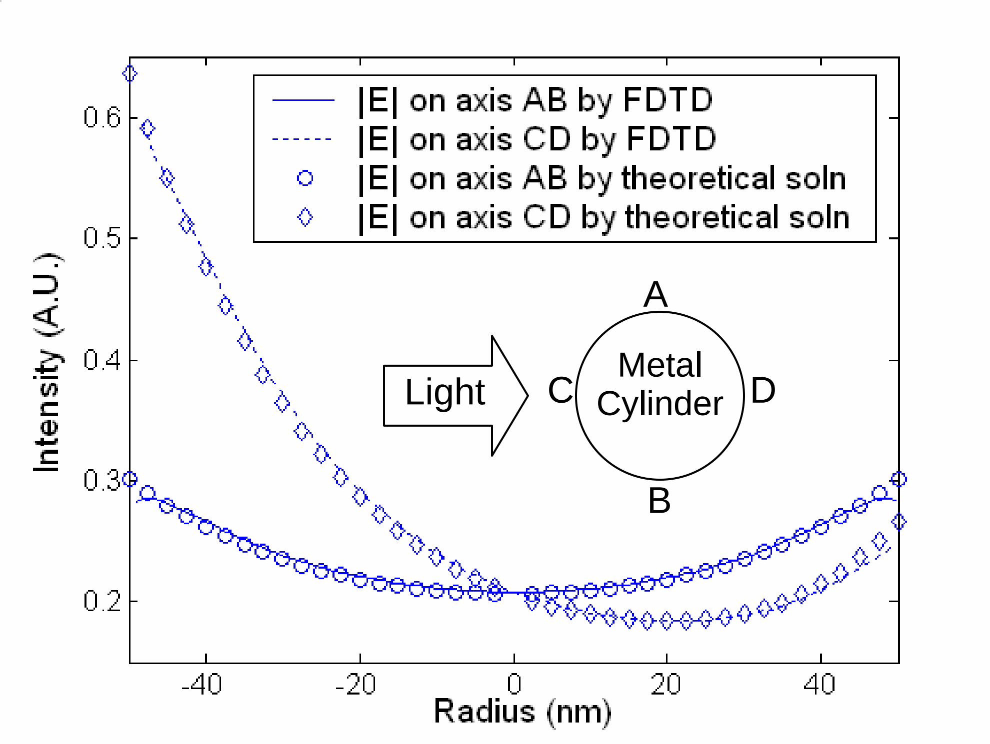

Figure 2-7: Comparison of FDTD modeling results and theoretical solution.

2.3.6 Discussion

There are some limiting situations where we should be cautious about using FDTD modeling.

Since the FDTD method is a time domain method, the transient response is calculated rather than directly calculating the harmonic field as in a FEM method. In my FDTD simulation, the iteration is repeated until harmonic fields are established and then the fields are obtained by calculating the amplitude of the oscillation. An appropriate grid size has to be selected otherwise not only enormous storage space is required for the variables but also the time steps are too small and the iterations become too long to bear.

The material properties we use in my FDTD modeling are obtained from experimental data of bulk materials. As we know, the electrical properties of a material do not necessarily come from a single atom or molecules but rather a collection of them. Special care has to be taken when the minimum dimension of the structures is close to the scale of the atoms or molecules, at which level the EM response will be significantly different from that of a bulk material. Generally speaking, it should be safe to have a minimum dimension on the order of ten nanometers. Below that, the FDTD modeling might be physically no meaning.

2.4 SUMMARY

In this chapter, the numerical techniques for computational electromagnetism were first briefly reviewed. The Finite Difference Time Domain method was chosen as the primary method for this dissertation study and details of this technique were reviewed. A 2D TM mode numerical code based on FDTD method was built to study light interaction with sub-wavelength scale structures. The basic issues associated with FDTD method, such as the PML boundary treatment technique to simulate open-space problem, plane wave excitation, and handling of metallic materials having negative dielectric constant, were addressed and enabled in this code. The model was benchmarked with the theoretical solution and can be used as a modeling tool for this dissertation study.

REFERENCE

1. C. Hafner, *The generalized multipole technique for computational electromagnetics* Artech House, Boston, (1990).

2. L. Novotny, D. W. Pohl, B. Hecht, "Scanning near-Field Optical Probe with Ultrasmall Spot Size," *Optics Letters*, **20**, pp.970-972 (1995).
3. R. F. Harrington, *Field Computation by Moment Methods*, the Macmillan Co., New York (1968).
4. M. G. Moharam, T. K. Gaylord, "Diffraction Analysis of Dielectric Surface-Relief Gratings," *Journal of the Optical Society of America*, **72**, pp.1385-1392 (1982).
5. K. D. Paulsen, D. R. Lynch, "Elimination of Vector Parasites in Finite-Element Maxwell Solutions," *Ieee Transactions on Microwave Theory and Techniques*, **39**, pp.395-404 (1991).
6. D. R. Lynch, K. D. Paulsen, "Origin of Vector Parasites in Numerical Maxwell Solutions," *Ieee Transactions on Microwave Theory and Techniques*, **39**, pp.383-394 (1991).
7. K. S. Yee, “Numerical Solution of Initial Boundary Value Problems Involving Maxwell's Equations in Isotropic Media,” *IEEE Transactions on Antennas and Propagation*, **14**, 302- 307 (1966).
8. A. Taflove, *Computational electrodynamics: the finite-difference time-domain method,* Artech House, Boston, (1995).
9. K. S. Kunz, R. J. Luebbers, *The finite difference time domain method for electromagnetics,* CRC Press, Boca Raton, (1993).
10. D. M. Sullivan, IEEE Microwave Theory and Techniques Society., *Electromagnetic simulation using the FDTD method*, IEEE Press series on RF and microwave technology. IEEE Press, New York, (2000).

11. J. P. Berenger, "A Perfectly Matched Layer for the Absorption of Electromagnetic-Waves," Journal of Computational Physics, 114, pp.185-200 (1994).
12. S. K. Gray, T. Kupka, "Propagation of light in metallic nanowire arrays: Finite-difference time-domain studies of silver cylinders," *Physical Review B*, **68**, pp.- (2003).
13. E. D. Palik, *Handbook of optical constants of solids*, Academic Press, Orlando, (1985).
14. P. W. Barber, S. C. Hill, *Light scattering by particles: computational methods* World Scientific, Singapore; Teaneck, N.J., (1990).

Chapter 3: Near-field Enhanced Mold-Assisted Direct Nanopatterning

The aggressive pursuit of ever decreasing feature size in modern integrated circuit fabrication has been a hallmark of the microelectronics industry. Finer feature size is not only desirable in microelectronics for higher performance, but also in nanofabrication for applications in many aspects in nanotechnology including biomedical engineering and the life sciences. However, it is difficult to conveniently and cheaply achieve critical dimensions at sub-wavelength scale due to the optical diffraction limit using traditional photolithography techniques.

Recently, there has been extensive research interest in optical near-field, which has an intrinsic scale smaller than the wavelength of the EM radiation. The blooming research in the optical near-field is following the invention of Scanning Near-field Optical Microscopy (SNOM). As the understanding in this area progresses, such optical near-field has been studied as an alternative route to improve photolithography resolution and achieve large area parallel nanofabrication.

3.1 INTRODUCTION TO OPTICAL NEAR-FIELD AND NSOM

3.1.1 Aperture Based NSOM

Since the invention of scanning tunneling microscope (STM), various schemes of scanning probe microscopes have been realized. Among them, the best known representative is perhaps the Scanning Force Microscope (SFM) or Atomic Force Microscope (AFM). In 1984, Pohl et al. demonstrated the possibility to circumvent the diffraction limit in the optical regime by scanning an illuminated sub-wavelength aperture as a quasi-point light source in close proximity to the sample surface [l]. This new technique is called Scanning Near-field Optical Microscopy (SNOM or NSOM) and has triggered tremendous research interest in NSOM and underlying optical near-field phenomena since then. The basic idea behind NSOM is that immediately behind the aperture, the light field is spatially confined to a scale comparable to the size of aperture, the optical near-field. Only if a scatterer is within such local light from the aperture will it interact with the radiation field, as shown in Fig. 3-1. The smaller the aperture, the higher resolution theoretically NSOM can achieve.

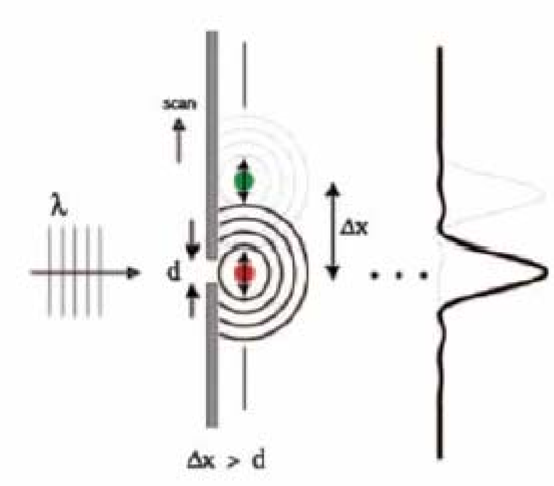

Figure 3-1: Schematic of aperture based scanning near-field microscopy.

The above approach is generally termed as aperture-based NSOM and different versions of this approach have been developed. In one of the later versions, a tapered glass fiber tip was coated with aluminum to prevent light leakage except at the very end of the tip, leaving an aperture of a few tens of nanometer [2]. Laser light is coupled into the fiber and guided towards the tip by total internal reflection. Light emerged from the tiny aperture is transmitted through the sample and detected with conventional diffraction-limited optics using known contrast enhance mechanism. Outstanding features of this technique are the non-destructiveness, ambient working condition, the wavelength and polarization sensitivity, and the penetration of the optical near field into the transparent sample. This permits surface sensitive spectroscopic imaging with nanometer spatial resolution. NSOM has already been used for imaging biological samples [3], improving data storage [4-5], and investigating the fluorescence from single dye molecules [6].

Unfortunately, only a tiny fraction of the light coupled into the fiber is emitted through the aperture because of the propagation cutoff of the waveguide modes. The low-light throughput and the finite skin depth of the metal are the limiting factors for resolution of aperture based NSOM. Also there are many practical issues in aperture probe fabrication. First it is difficulty to obtain a smooth metal coating and reproducible probe fabrication. Second, the flat end of the aperture probes is not suitable for simultaneous topographic imaging with high resolution. Third, the absorption of light in the metal coating causes significant heating that poses a problem for temperature-sensitive applications.

3.1.2 Aperutreless NSOM

People later found that the above mentioned limitation of aperture probes can be overcame by using a nano tip irradiated by a laser light. By this approach, the resolution of NSOM can also be improved.

As we know, the field near any light illuminated surface is constituted of two kinds of waves: propagating waves and evanescent waves. The former can propagate to the far-field while the latter has the maximum amplitude at the surface and dies away exponentially as it leaves the surface. According to Fourier Optics, the higher resolution information, which has higher wave vector number, is carried only by the evanescent wave and is lost in the far-field. In another word, the diffraction limit of classical microscopy stems from the inability of evanescent waves to propagate. However the evanescent wave can be partially converted to propagating radiation by using a nano probe. The probe can either be used as a local scattering source or a local excitation source. In the first one, a pointed probe, a tip or even a particle is used to locally perturb the fields at a sample surface. The response to this perturbation can be detected in the far field with a high signal-to-noise ratio. However if the surface is very rough, the method is hard to differentiate the true optical contrast resulted from material property or from topographic contrast due to the fact that the scattering efficiency depends strongly on separation distance between the probe and the sample.

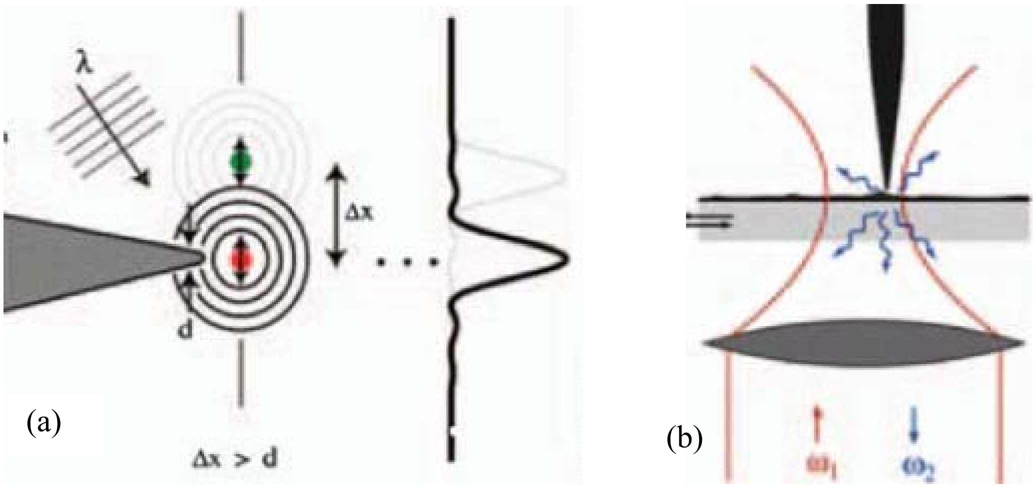

(a)

(b)

Figure 3-2: Principle of tip-enhanced near-field optical microscopy. (a) Schematic of the method. (b) Practical implementation.

On the other hand, the probe tip can also be used as a local light source. Under certain conditions, such as proper polarization, suitable probe materials and probe geometries, the field near the end of the probe tip can become strongly enhanced over the field of the illuminating laser light [7-8]. The enhancement can be of several orders bigger than the incident light according to some literature [7] and thus many practical applications can be achieved. This local-excitation scheme is commonly referred to as tip-enhanced scanning near-field optical microscopy as illustrated in Fig 3-2. This approach enables simultaneous spectral and sub-diffraction spatial measurements, but it depends sensitively on the magnitude of the field-enhancement factor, which is only achieved under certain conditions. In the next session, the factors that affect optical near-field enhancement are discussed.

3.1.3 Optical Near-field Enhancement

Following above introduction it is clear that a higher optical near-field enhancement is preferable in tip-enhanced NSOM. In fact higher field enhancement has many applications such as optical tweezers, near-field Raman microscopy, and photolithography. In this section we review literatures investigating on how to increase the field enhancement around a NSOM tip.

Although it has been demonstrated experimentally in various studies that nanoscale NSOM imaging can be performed by using tips made of dielectric or semiconductor materials [9–10], it is generally accepted that the field enhancement and the scattering efficiency are stronger for metallic tips [11-13]. Novotny et al. [7] studied the optical near-field of a gold tip in water for the purpose of trapping and alignment of dielectric particles by optical forces, which they called ‘optical tweezers’. The Multiple Multipole method (MMP) was employed in their study, in which electromagnetic fields are represented by a series expansion of known analytical solutions of Maxwell’s equations. As shown in Fig. 3-3, if the polarized light is illuminated from the bottom of the tip, no matter how the light is polarized, there is barely any enhancement. However if the light is shine from side with the polarization parallel to the axis of the tip, which is TM polarization, the field enhancement can reach almost 3000. Interestingly, if the light polarization is perpendicular to the axis of the tip (TE mode), the field enhancement is diminished again.

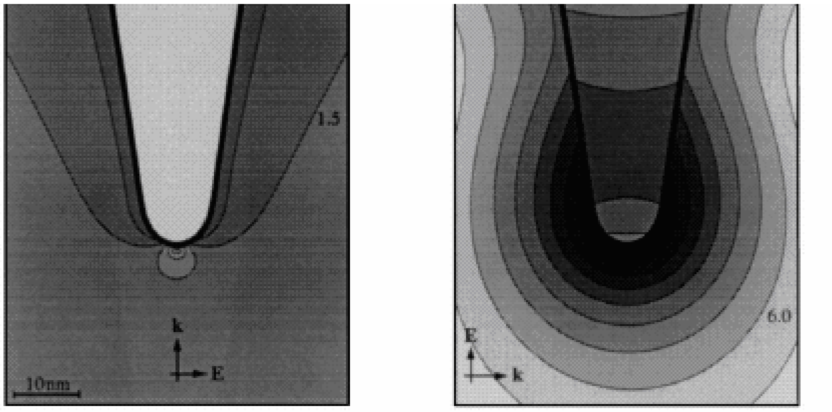

Figure 3-3: Near field of a gold tip in water illuminated by monochromatic waves of λ = 810 nm with two different polarizations [7].

Krug et al. [14] carried out three-dimensional electromagnetic simulation of gold nanoparticles with specific geometries for rational design of apertureless NSOM probes. Analytical solutions for field enhancement by spheroidal particles were first used to provide physical insight for probe design, which indicated that probes need to be not only sharp, but also finite in length to generate the higher field enhancement. Pyramid structures were also studied by using a three dimensional FDTD simulations. Field enhancements for right trigonal pyramids are found to be size and wavelength dependent. The authors believe these structures can be fabricated using current nanofabrication techniques, and therefore hold great promise as apertureless NSOM probes.

A proper understanding of the near field around the tip end and the ability to tune this near-field are critically important to NSOM instrumentation and NSOM image interpretation. Sun et al. [15] systematically studied the effects of a number of parameters related to the application of apertureless NSOM, e.g., polarization, incident angle, wavelength of the incident laser, tip material, and tip length. Their results show that all the above parameters have a significant influence on near-field enhancement. The dependence on angle of incidence is of particular interest. Although the electric field component along the tip axis plays an important role, maximum enhancement does not occur at an incident angle of 90°, where the electric field of the laser is along the tip axis. When light is illuminated with an angle, the multipoles caused by electric field components along and perpendicular to the tip axis are strongly coupled and both electric field components can contribute to the field enhancement. Depending on the tip geometry, there should be a certain angle at which the field enhancement reaches the maximum.

3.1.4 Direct Surface Patterning by Optical Near-field Enhancement

One of the practical applications of optical near-field enhancement phenomena could be direct surface patterning for data storage or lithography. The advantage of this approach over traditional methods for data storage and lithography is the easy setup and intrinsic nanoscale dimension. This approach, though still at its infancy, promises technology advances.

After the invention of STM, manipulation and modification of surfaces have been accomplished by using various STM interactions such as contact forces, electrical fields etc. What interested us is a method externally injecting energy into the tip–substrate gap by laser radiation. This technique is so called focusing of laser radiation in the near field of a tip (FOLANT) and is illustrated in Fig 3-4. The FOLANT technique, which has several advantages compared to other methods mentioned above, was first suggested by

Wessel [16]. Gorbunov et al. [17] created small hillocks with silver tips on the surface of gold films in vacuum. Jersch et al. [18] used this technique and demonstrated surface patterning of features such as craters, ditches and hillocks with a lateral resolution of approximately 10 nm. The process has been demonstrated on gold and gold/palladium substrates by utilization of tungsten, silver, and platin/iridium tips. Substrate evaporation and surface grain reorganization were observed at low laser intensities using tungsten tip. No distortion of the employed tips during the structuring process was observed.

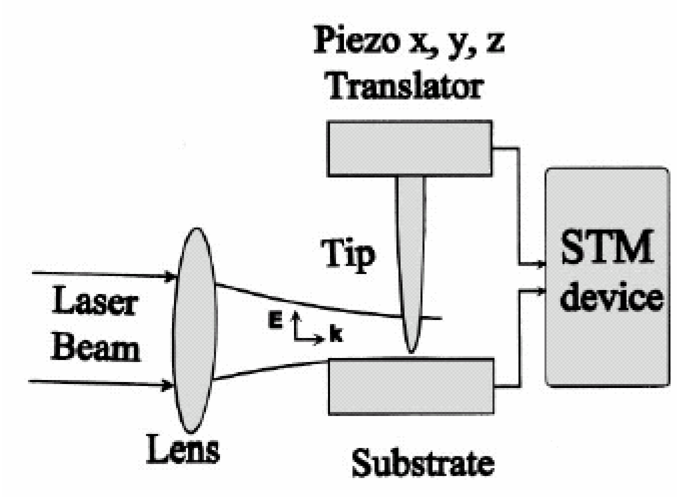

Figure 3-4: Schematic diagram of FOLANT.

Cooper et al. [19] selectively grew a single wall carbon nanotube on an AFM cantilever and demonstrated a pattern density of 1.6 Tbits/in2 on an atomically flat titanium surfaces on alumina substrate by anodically oxidizing titanium locally. As claimed by the authors, the threshold of a terabit per square inch was first exceeded at room temperature and ambient environment.

Chimmalgi et al. [20] combined femto-second pulsed laser radiation with local field enhancement in the near-field of a sharp tip and demonstrated that controllable surface nano-machining can be achieved in this manner. Ultra-short laser pulse is believed to be an effective method for precision materials processing and surface nano-modification because of minimal thermal and mechanical damage. By coupling 800-nm femtosecond laser radiation with a silicon tip in ambient air, line structures, complex grid patterns and curved contours of uniform width and depth can be nano-patterned in thin gold films with great accuracy and precision. The authors also conducted FDTD simulation of the spatial distribution of the laser field intensity beneath the tip, which confirmed that the observed high spatial resolution is due to the enhancement of the local field. Possible structuring mechanisms and factors affecting this process, such as laser pulse energy and tip-sample separation distance, were discussed. The authors believed this process is a very intriguing means for massive nanolithography due to the flexibility in the substrate material selection, high spatial resolution of ~10 nm. They also suggested that fast processing rates are achievable through simultaneous irradiation of multi-array tips.

On the other hand, people have also been studying the optical near-field around nano spheres for a more fundamental understanding of the phenomena. Munzer et al. [21] reported a method that allows the nanostructuring of surfaces with intense laser pulses. Isolated polystyrene spheres with diameters 320 nm, 800 nm and 1.7 μm, respectively, were deposited on a silicon or glass surface and illuminated with short (355 nm, 8ns) and ultrashort (800 nm, 100fs) laser pulses. Holes right underneath these particles were produced. According to their calculations of the field near the particles based on Mie theory [22], they came to the conclusion that geometrical optics (focusing by the spherical shape of the sphere), as well as near-field effects, contribute to the size and shape of these holes.

Lu et al. [23] studied the Marangoni effect (material redistribution due to surface tension difference in a liquid layer) in nanosphere-enhanced laser direct nanopatterning of silicon surface. A monolayer of nanosphere array was formed on the silicon substrate by self-assembly and irradiated by 248-nm excimer laser. The silicon surface was locally melted during the irradiation due to optical field enhancement between the nanosphere and the substrate. The molten material was redistributed due to Marangoni effect that arises due to the competition between a thermocapillary force and a chemicapillary force acting on the molten material, resulting in the formation of a nanodent array. The morphology of the nanodents changed from bowl-type to ‘‘Sombrero’’ with increase of laser intensity.

As the diameter of the sphere becomes smaller than the laser wavelength, near-field enhancement plays a more dominant role in nanostructuring the substrate surface. Theppakuttai et al. [24] produced nanopatterns on borosilicate glass by a 1064 nm Nd:YAG laser using silica nanospheres of 640 nm in diameter. The laser beam was shined from the bottom of the glass sample, in which the geometrical optics effect was minimized. Nanofeatures on the glass substrate were still created, which could only be explained by the direct near-field enhancement due to the spheres.

3.1.5 Near-field Nano Photolithography

The above review has shown that near-field enhancement associated with nanostructures (tip or sphere) can be utilized for direct nanoscale surface patterning. Compared to traditional lithography techniques, this nanolithography approach has the following merits. First, like the focused ion beam (FIB) technique, this approach can directly pattern various thin films, thus it is a single step process without the need of processing the masking layer. Secondly, unlike FIB or EBL which require vacuum working condition, it is a relatively simple and cheap process to achieve nanoscale dimension in ambient environment.

Meanwhile there are also tremendous research efforts to improving the resolution of contact or proximity mode traditional photolithography. The resolution of tradition photolithography can be easily decreased by using a shorter wavelength light source, such as Deep Ultra Violet (DUV) or even Extreme Ultra Violet (EUV) light. However the making of such light source is not easy at all and the optics to handle such UV light is complicated and making the system complex and expensive. Moreover, this approach is not in line with the interest of this study. In this section, I will focus on innovative photolithography schemes that utilize the optical near-field to achieve nano scale resolution.

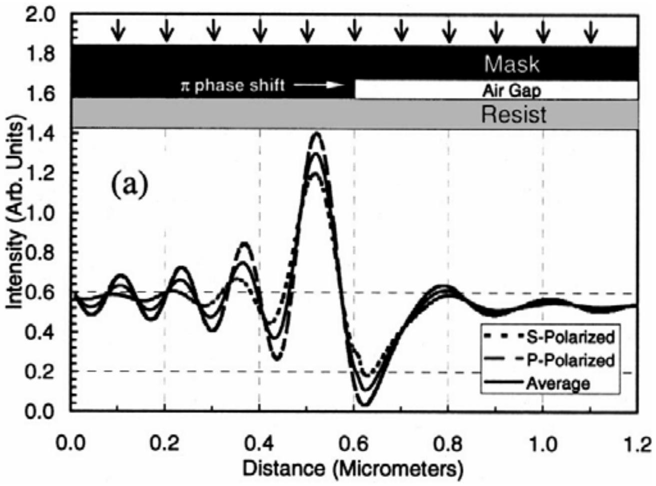

Figure 3-5: Configuration of the phase-shifting mask and associated intensity distribution.

Phase shift technology utilizes the near-field generated by phase differences introduced by optical path difference in the phase shift mask (PSM) and is considered as a resolution enhancement technique. Kunz et al. [25] combined PSM and DUV (193 nm) technologies and created arbitrarily shaped structures as small as 45 nm. The configuration of the mask is shown in Fig. 3-5, and the near-field intensity distribution below the mask was calculated using FDTD method. Conformal and flexible polyimide substrates were used to ensure good contact between the mask and substrate

Alkaisi et al. [26] demonstrated sub-diffraction limit photolithography using evanescent near-field optical lithography (ENFOL) with broadband illumination. Line width of 50 nm and gratings with 140 nm period were achieved and the pattern was transferred to a depth of more than 100 nm into silicon by RIE. The mask pattern used in ENFOL was in a 25-nm-thick NiCr (80:20) absorber layer fabricated on 2-μm-thick silicon nitride membranes, which was deposited on Silicon Substrate. Although the light source has a spectrum between 313 and 600 nm, the resist they used was insensitive for wavelengths greater than 450 nm. And UV light below 340 nm was absorbed in silicon nitride membranes. Full electromagnetic field simulations validated their experimental findings and revealed that the exposure is dominated by one polarization (TM mode) for the grating structures used in their study.

Goodberlet et al. [27] used near-field mask named embedded-amplitude mask (EAM), which has “embedded attenuator” made of chromium to enhance the near-field effect. The FDTD method was used to support the design of mask and guide the experiments. Sub-50nm lines, holes and posts have been patterned at exposing wavelength of 220nm generated by an arc lamp. The EAM mask is made of three layers of different materials and anti-reflective coating is also used in the resist stack.

Light coupling mask (LCM) is based on the idea that light can across interface of two structures having matched impedance and being in conformal contact without dispersal. A potential limitation of such light coupling masks is the difficulty of achieving uniform coupling between the light-guiding structures and the photoresist. Schmid et al. [28] made LCMs from high modulus siloxane polymers with sufficient strength so that intimate contact between LCM and the substrate was ensured. Images of arbitrarily shaped features with sub-100 nm dimensions much smaller than that of the wavelength of the exposing light were formed in the resist in a 1:1 correspondence. A master was made by E-beam lithography and siloxane polymer LCMs were replicated by direct molding from the master.

3.2 NEAR-FIELD ENHANCED PARALLEL NANO-MOLDING

We have shown that near-field enhanced direct patterning technique can be an intriguing alternative nanopatterning technique because of its several advantages over existing nanolithography tools and nanoscale photolithography methods. However the direct patterning based on near-field enhancement was never demonstrated in a parallel fashion, which we believe, if demonstrated possible, will make this technique more attractive. It is our goal to achieve large area parallel patterning utilizing the near-field enhancement effect.

However the idea of simply having more than one nano tip and shining laser light from side will have many practical issues, for example the accessibility of light to every gap between tip and substrate. Instead, we investigated the possibilities to shine the laser from the back of the substrate so the whole area to be patterned can be under illumination. The scheme is illustrated in Fig 3-6. A transparent substrate, Pyrex glass wafer, was used. Laser irradiation (full width half maximum=10 ns, λ = 532 nm) was from the back of the substrate at an angle. However we need to investigate if field enhancement could be enough in such scheme as the light will be illuminated at a large angle. Also, it is interesting to see the possibility of patterning a line pattern using a nano ridge instead of scanning a nano tip along the surface. Again it is important to study the optical enhancement since the field enhancement around a nano ridge structure has never been studied before.

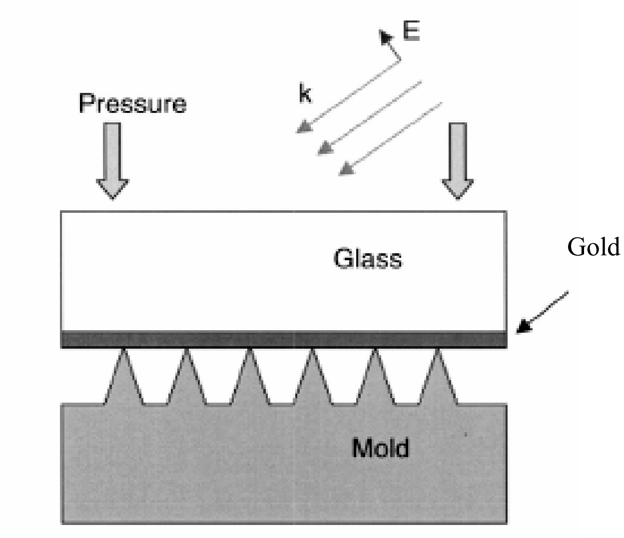

Figure 3-6: Schematic view of near-field enhanced direct patterning.

3.2.1 FDTD Simulation

In this section, I present my FDTD simulation results to investigate the feasibility of the scheme proposed in Fig 3-6. In order to have large field enhancement, a thin Au film was deposited on the substrate by electron beam evaporation and a thin Cr film was deposited on the ridge/tip mold made by silicon dioxide. The reason we chose different metal on tip/ridge and substrate is explained in later section. The choice of metal film thicknesses was not straightforward. The metal films are needed to enhance the local field, however metals are also good light absorber at the same time and light intensity can be easily attenuated with a thick metal film. We optimized the film thickness by FDTD modeling.

The optical properties of the materials at 532 nm wavelength were first determined from literature [29] and fitted to the Drude model. Geometries of the mold and the substrate were built in FDTD with appropriate material properties. The incident angle of laser was set at 50 degree. Figure 3-7(a) shows the contour of the electric field around the contacting area between the nano ridge and the substrate. The numerical value along the line A–A as indicated in Fig. 3-7(a) was extracted and plotted in Fig. 3-7(b). The results show maximum energy enhancement of ~11 is achievable with this configuration.

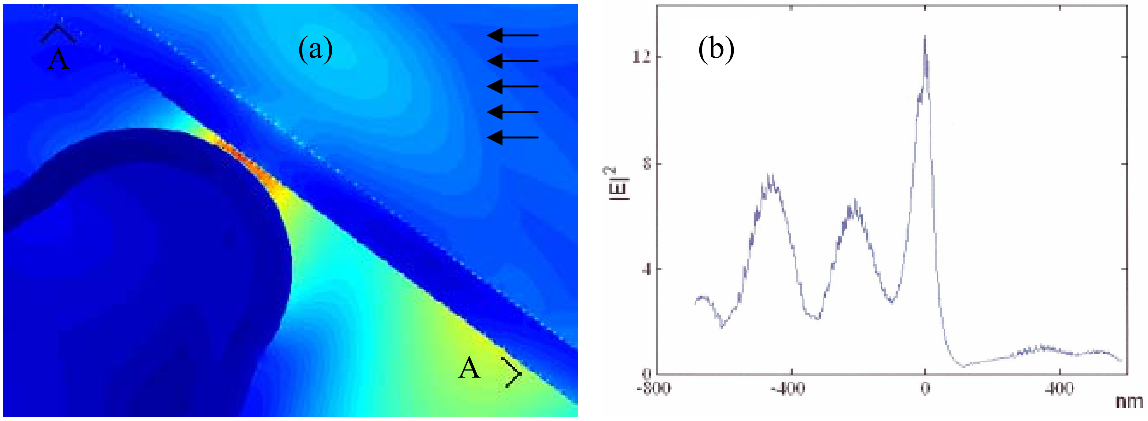

Figure 3-7: FDTD simulation results: (a) contour plot of electric field amplitude in the vicinity of the ridge end and the substrate, (b) the electric field amplitude on the surface of the glass substrate along A–A. The near-field enhanced peak has a width of about 100 nm at the half peak value.

If we zoom in the tiny gap between the ridge and substrate, the FDTD results show that a gradient of field amplitude exists from the ridge to the substrate and the stronger field is always closer to the ridge. Since the mechanism of the proposed direct patterning is based on near-field enhanced local material removal, according to the simulation the metal on the mold would be evaporated first if the same metal material is used on the ridge and the substrate. In fact we did preliminary experiments using gold film on the ridge and the results we got indicated material was deposited on the substrate rather than material removal that we were expecting. Chromium, which has a much higher melting temperature and better durability, was then used on the mold for the near-field enhanced direct patterning.

3.2.2 Fabrication of Nano-tips and Nano-ridges

A fabrication process with good controllability of tip/ridge geometry is desirable for the near-field enhanced direct patterning technique. Following the microfabrication techniques used to make a tip array [30], long rectangular masks were used to fabricate ridge array by taking the advantage of isotropic wet etching. We first deposited a 4-μm-thick low temperature oxide (LTO) layer on a silicon wafer using low pressure chemical vapor deposition (LPCVD). LTO was used as it can reach such thickness in a reasonable amount of time; however, the film quality is usually not good compared to other silicon dioxide thin film deposition methods. The wafer was then annealed at 1000°C for about an hour to enhance film density and etching durability. A layer of 200 nm polysilicon, which would be used as the third masking layer for buffered oxide etching (BOE) to form the desired tip/ridge structure, was deposited by LPCVD. The second masking layer, a 100-nm-thick aluminum layer for reactive ion etching (RIE) was then deposited by E-beam evaporation. Photolithography was used to pattern rectangles in photoresist and the resist was used as the first masking layer to transfer the pattern to aluminum by wet etching. The photolithography mask was made with critical dimension (CD) smaller than 50 nm to minimize the roughness of line pattern transferred in each lithography step. With the Al mask, RIE was carried out to transfer the pattern into LTO with an etching depth of more than one micron. Then, a highly diluted (20:1) BOE was used to slow down the etching process for easy control of the etching process. The tips or ridges formed right after the masks were etched free. Finally, the ridges and the tips were coated with a 30 nm layer of chromium by e-beam evaporation.

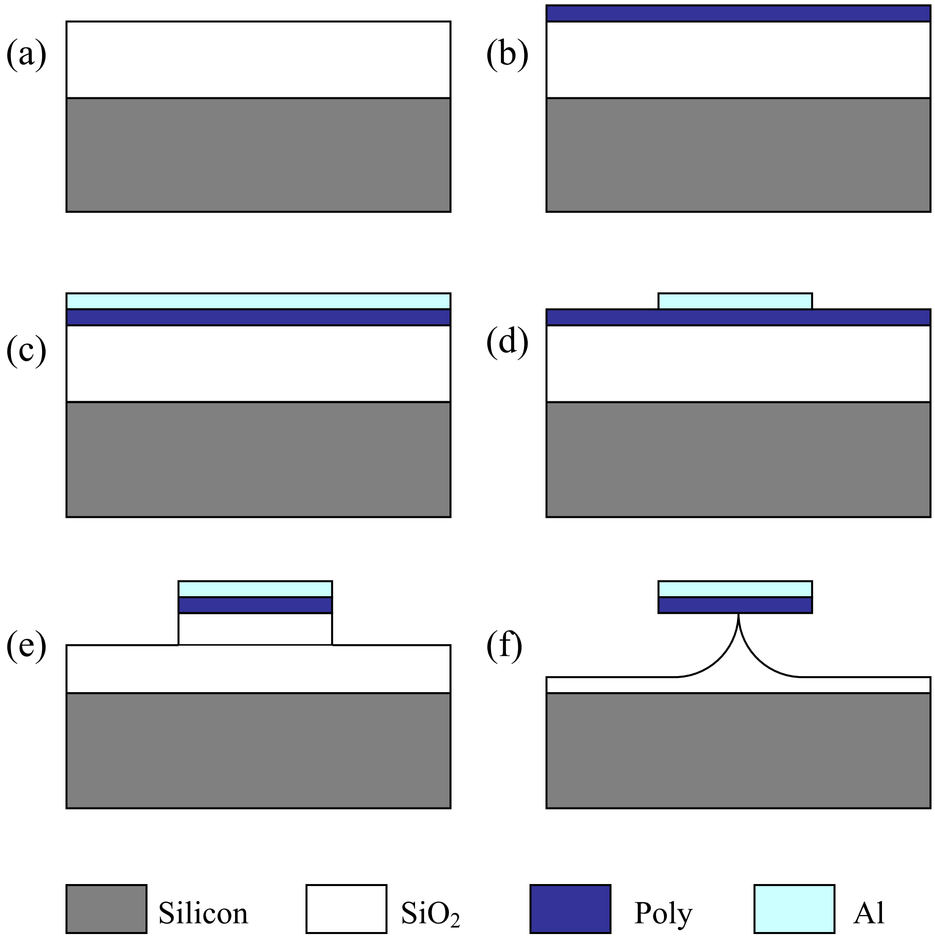

Figure 3-8: Schematic view of tip/ridge fabrication. (a) Deposit 4μm LTO by LPCVD; (b) Deposit 200 nm polysilicon by LPCVD; (c) Deposit 100 nm Aluminum by E-beam evaporation; (d) Pattern a photoresist layer using photolithography and then transfer the pattern to Al by wet etching using Al etchant; (e) Dry etch into polysilicon and LTO by

RIE; (f) Form the tip/ridge structure in wet etch using BOE by precise control of the etching time.

Fig. 3-8 illustrates the process flow and Fig. 3-9 shows the scanning electron microscopy (SEM) image of the ridges, which has end radii less than 50 nm.

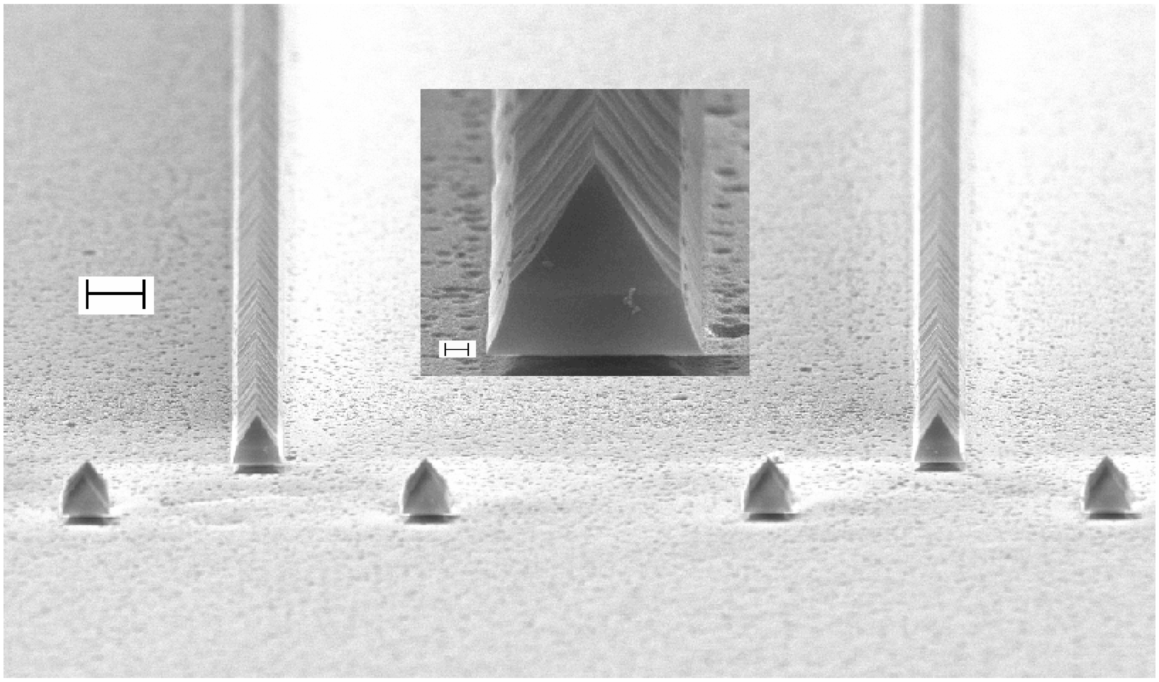

Figure 3-9: SEM pictures of the nano ridge and nano tip array, scale bar = 2 μm. Inset: close view at the end of the nano ridge, scale bar = 200 nm.

3.2.3 Experimental Demonstration

During the experiment, the threshold laser intensity for direct ablation of the gold film on glass substrate without the near-field mold was first measured as 0.53 J /cm^2 at the incident angle of 50° of laser irradiation. The laser energy was then reduced by a factor of 2–3 for direct patterning using the near-field mold. At this energy level, no visible damage can be seen by directly shining the beam onto the sample at that angle. To ensure contact between the ridges and the glass substrate, a small force was applied during the experiment to engage the mold and the substrate. Care was taken to ensure that the laser light shined on the ridge structure with a TM mode polarization, i.e. the polarization of laser is not parallel to the ridges. Only after a few laser shots the patterns formed on the substrate and the SEM images in Fig. 3-10 show that lines were successfully transferred from the ridges of the near-field mold to the gold film on glass. We have found the pattern size and quality were affected by the laser energy used. At half the threshold energy (0.26 J /cm^2), the width of the lines were measured to be about 200 nm, as shown in Fig. 3-10(a). In this case, the features are clearly defined and smooth at the boundary. When the laser energy were lowered to about 0.20 J /cm^2, the feature size decreased to about 100 nm; however the defects of the ridges, result from the defects of the etching mask made by E-beam lithography, became noticeable on the patterns (Fig 3-10b). AFM results revealed pattern depth of about 20 nm for the high energy case, as seen in Fig. 3-11, and about 15 nm for the low intensity case.

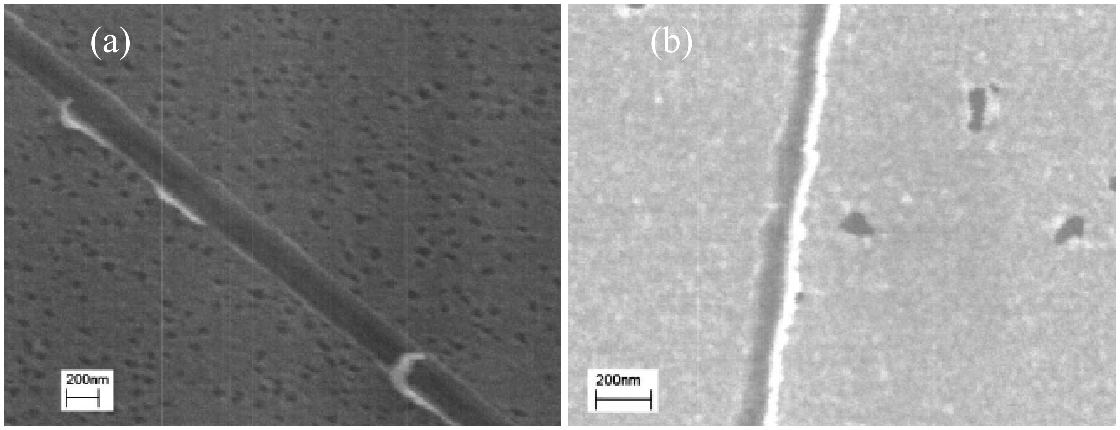

Figure 3-10: SEM close view of the line pattern at laser energy of: (a) 0.26 J /cm^2 (b) 0.20 J /cm^2.

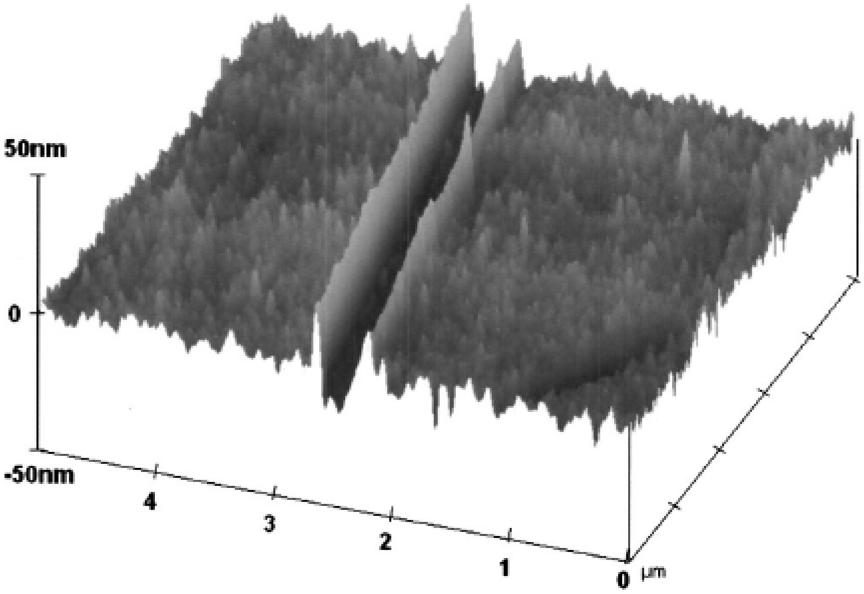

Figure 3-11: AFM results of the line pattern at laser energy of 0.26 J /cm^2.

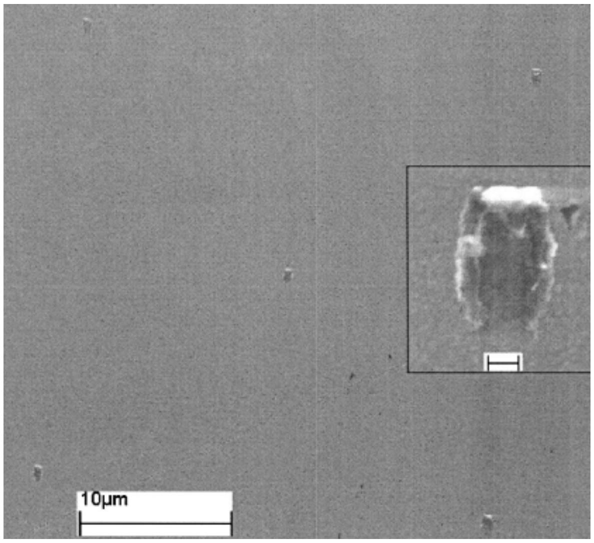

Figure 3-12: SEM images dot array on a gold film. The scale bar in the inset indicates 200 nm.

By using a tip array instead of ridge array, an array of pits was produced on the gold thin film, as shown in Fig. 3-12, at about 1/4 of the threshold energy. The energy needed to produce dot pattern is further reduced since the tip structure has a relatively stronger optical field enhancement compared to that of a ridge. In fact, this energy is still too strong as perceivably more residue can be seen around the pit.

From Fig. 3-10 and 3-12 the residue of the gold film can be observed at the edges of the channels or pits. AFM results shown in Fig. 3-11 also verified the protrusion at the edge of the patterns. This could be either the result of the pressing mold to force the material relocation or due to naturally the surface tension force at the liquid/solid interface, as discussed previously [23].

Even if the pressing force between the mold and the sample might have played a role in the patterning process, we have found that direct molding without laser incidence did not create any pattern on the gold film. Furthermore, for the same laser energy and pressing force, we also tried to simply rotate the ridge array horizontally by 90 degree with respect to the incidence of laser beam. In this case, for the ridge mold, TM polarization no longer exists and we found no patterns on the gold film, which indicates the polarization dependence of the field enhancement effect.

3.2.4 Discussion

The laser intensity enhancement factor (~3) by the ridge structure from the experiment was much smaller than the predicted value (~11) from FDTD simulation. The discrepancies can be understood by considering the pinholes in the evaporated gold film and defects at the interface, which will scatter incident laser radiation and reduce laser intensity coming to the contacting area. By improving the quality of the metallic film, higher enhancement could be achieved in experiment and as a result, the width and the quality of the patterns can be controlled better by adjusting the laser energy.

We believe the scheme we proposed here for near-field enhanced direct surface patterning can be extended to other materials/substrate. For example, silicon substrate can be patterned in the same setup by using an infrared laser beam (for example, 1064 nm Nd:YAG laser), which is transparent to silicon. Gold and Chromium can still be used to enhance optical near-field as their optical properties at 1064 nm do not vary significantly compared to those at 532 nm, indicating similar near-field enhancement behavior. Other metals, such as silver and aluminum, which also produce near-field enhancement and have a relatively low melting point at the same time, can be served as the metal film on the substrate as well.

Scanning probe lithography [31-33] has attracted intensive research interest as a new form of lithography technique. It has the potential to be an alternative to E-beam lithography with nanoscale resolution but simplified and cheaper setup and reduced proximity effect. However one of the major drawbacks it has is low throughput associated with the serial writing process. We believe our scheme can also combine with photolithography technique or even two-photon lithography [34] technique to overcome this disadvantage. In this case, a thin photoresist layer will be used instead of the metallic mask layer in the case of current study.

In another possible scheme, the incident beam could also be shone from the backside of a transparent mold. For example, the mold can be made of quartz wafer and coated with a thin layer of Chromium to enhance the near-field. In this case the transparency requirement on substrate is removed. However the scattering of light by the rough surface resulted from etching might be a concern.

3.3 SUMMARY

In this chapter, I investigated a direct surface nano patterning technique called ‘near-field-enhanced mold-assisted direct patterning’. Optical near-field enhancement around nanostructures, for example nano tips, was utilized to locally ablate the masking layer. In this study, we proposed a scheme in which we shined laser beam (wavelength 532 nm) from the backside of the substrate so that the whole patterning area was under illumination and parallel patterning can be achieved utilizing such phenomena. Nano ridge structure was fabricated and the near-field around such nano ridge was utilized to directly pattern lines in a single laser shot without the need to scan a nano tip. The resulted lines and dots pattern have a width or size ranging from 200 nm to 100 nm with depth on the order of 20 nm. Both experimental tests and numerical modeling results demonstrated the effect of near-field enhancement. We believe features with smaller size and better quality can be achieved using such method with better tip/ridge geometry and film quality.

Reference

1. D. W. Pohl, W. Denk, M. Lanz, "Optical Stethoscopy - Image Recording with Resolution Lambda/20," *Applied Physics Letters*, **44**, pp.651-653 (1984).
2. E. Betzig, J. K. Trautman, "Near-Field Optics - Microscopy, Spectroscopy, and Surface Modification Beyond the Diffraction Limit," *Science*, **257**, pp.189-195 (1992).
3. E. Betzig, R. J. Chichester, "Single Molecules Observed by near-Field Scanning Optical Microscopy," *Science*, **262**, pp.1422-1425 (1993).
4. E. Betzig *et al.*, "Near-Field Magnetooptics and High-Density Data-Storage," *Applied Physics Letters*, **61**, pp.142-144 (1992).

5. T. J. Silva, S. Schultz, D. Weller, "Scanning near-Field Optical Microscope for the Imaging of Magnetic Domains in Optically Opaque Materials," *Applied Physics Letters*, **65**, pp.658-660 (1994).
6. W. P. Ambrose, P. M. Goodwin, J. C. Martin, R. A. Keller, "Single-Molecule Detection and Photochemistry on a Surface Using near-Field Optical-Excitation," *Physical Review Letters*, **72**, pp.160-163 (1994).
7. L. Novotny, R. X. Bian, X. S. Xie, "Theory of nanometric optical tweezers," *Physical Review Letters*, **79**, pp.645-648 (1997).
8. O. J. F. Martin, C. Girard, "Controlling and tuning strong optical field gradients at a local probe microscope tip apex," *Applied Physics Letters*, **70**, pp.705-707 (1997).
9. J. M. Gerton, L. A. Wade, G. A. Lessard, Z. Ma, S. R. Quake, "Tip-enhanced fluorescence microscopy at 10 nanometer resolution," *Physical Review Letters*, **93**, pp.- (2004).
10. F. Zenhausern, Y. Martin, H. K. Wickramasinghe, "Scanning Interferometric Apertureless Microscopy - Optical Imaging at 10 Angstrom Resolution," *Science*, **269**, pp.1083-1085 (1995).
11. E. J. Sanchez, L. Novotny, X. S. Xie, "Near-field fluorescence microscopy based on two-photon excitation with metal tips," *Physical Review Letters*, **82**, pp.4014-4017 (1999).
12. D. Haefliger, J. M. Plitzko, R. Hillenbrand, "Contrast and scattering efficiency of scattering-type near-field optical probes," *Applied Physics Letters*, **85**, pp.4466-4468 (2004).

13. H. G. Frey, S. Witt, K. Felderer, R. Guckenberger, "High-resolution imaging of single fluorescent molecules with the optical near-field of a metal tip," *Physical Review Letters*, **93**, pp.- (2004).
14. J. T. Krug, E. J. Sanchez, X. S. Xie, "Design of near-field optical probes with optimal field enhancement by finite difference time domain electromagnetic simulation," *Journal of Chemical Physics*, **116**, pp.10895-10901 (2002).
15. W. X. Sun, Z. X. Shen, "Optimizing the near field around silver tips," *Journal of the Optical Society of America a-Optics Image Science and Vision*, **20**, pp.2254-2259 (2003).
16. J. Wessel, "Surface-Enhanced Optical Microscopy," *Journal of the Optical Society of America B-Optical Physics*, **2**, pp.1538-1541 (1985).
17. A. A. Gorbunov, W. Pompe, "Thin-Film Nanoprocessing by Laser Stm Combination," *Physica Status Solidi a-Applied Research*, **145**, pp.333-338 (1994).
18. J. Jersch, K. Dickmann, "Nanostructure fabrication using laser field enhancement in the near field of a scanning tunneling microscope tip," *Applied Physics Letters*, **68**, pp.868-870 (1996).
19. E. B. Cooper *et al.*, "Terabit-per-square-inch data storage with the atomic force microscope," *Applied Physics Letters*, **75**, pp.3566-3568 (1999).
20. A. Chimmalgi, T. Y. Choi, C. P. Grigoropoulos, K. Komvopoulos, "Femtosecond laser aperturless near-field nanomachining of metals assisted by scanning probe microscopy," *Applied Physics Letters*, **82**, pp.1146-1148 (2003).
21. H. J. Munzer *et al.*, "Local held enhancement effects for nanostructuring of surfaces," *Journal of Microscopy-Oxford*, **202**, pp.129-135 (2001).
22. M. Kerker, *The scattering of light, and other electromagnetic radiation* (Academic Press, New York,, 1969).

23. Y. Lu, S. Theppakuttai, S. C. Chen, "Marangoni effect in nanosphere-enhanced laser nanopatterning of silicon," *Applied Physics Letters*, **82**, pp.4143-4145 (2003).
24. S. Theppakuttai, S. Chen, "Nanoscale surface modification of glass using a 1064 nm pulsed laser," *Applied Physics Letters*, **83**, pp.758-760 (2003).
25. R. R. Kunz, M. Rothschild, M. S. Yeung, "Large-area patterning of similar to 50 nm structures on flexible substrates using near-field 193 nm radiation," *Journal of Vacuum Science & Technology B*, **21**, pp.78-81 (2003).
26. M. M. Alkaisi, R. J. Blaikie, S. J. McNab, R. Cheung, D. R. S. Cumming, "Sub-diffraction-limited patterning using evanescent near-field optical lithography," *Applied Physics Letters*, **75**, pp.3560-3562 (1999).
27. J. G. Goodberlet, H. Kavak, "Patterning Sub-50 nm features with near-field embedded-amplitude masks," *Applied Physics Letters*, **81**, pp.1315-1317 (2002).
28. H. Schmid, H. Biebuyck, B. Michel, O. J. F. Martin, "Light-coupling masks for lensless, sub-wavelength optical lithography," *Applied Physics Letters*, **72**, pp.2379-2381 (1998).
29. E. D. Palik, *Handbook of optical constants of solids*, Academic Press handbook series. (Academic Press, Orlando, 1985).
30. L. Shi, S. Plyasunov, A. Bachtold, P. L. McEuen, A. Majumdar, "Scanning thermal microscopy of carbon nanotubes using batch-fabricated probes," *Applied Physics Letters*, **77**, pp.4295-4297 (2000).
31. F. H'dhili, R. Bachelot, G. Lerondel, D. Barchiesi, P. Royer, "Near-field optics: Direct observation of the field enhancement below an apertureless probe using a photosensitive polymer," *Applied Physics Letters*, **79**, pp.4019-4021 (2001).

32. A. Tarun, M. R. H. Daza, N. Hayazawa, Y. Inouye, S. Kawata, "Apertureless optical near-field fabrication using an atomic force microscope on photoresists," *Applied Physics Letters*, **80**, pp.3400-3402 (2002).
33. X. B. Yin, N. Fang, X. Zhang, I. B. Martini, B. J. Schwartz, "Near-field two-photon nanolithography using an apertureless optical probe," *Applied Physics Letters*, **81**, pp.3663-3665 (2002).
34. S. Kawata, H. B. Sun, T. Tanaka, K. Takada, "Finer features for functional microdevices - Micromachines can be created with higher resolution using two-photon absorption.," *Nature*, **412**, pp.697-698 (2001).

Chapter 4: Surface Plasmon and Two-dimensional Surface Plasmon Assisted Nanolithography (2D-SPAN)

Although our model based on the FDTD method has been proved to be a useful tool for the study of sub-wavelength scale optical phenomena, i.e. the near-field optical enhancement, much has not been understood about the physics behind the enhancement, and its mysterious dependence on factors such as material, polarization, wavelength etc. On the other hand, there has been a renewed research interests in Surface Plasmons (SPs) due to recent advances in patterning and characterization of metal structures at the nanometer scale. It turned out that the mechanism of SPs can be introduced into near-field phenomena and explains very well the enhancement effects.

4.1 SURFACE PLASMON

4.1.1 Introduction

Many of the fundamental electronic properties of the solid state, such as energy band gap, can be successfully described by the analogy of electrons interacting with periodic array of atoms. Alternatively, the free electrons of a metal can be treated as an electron liquid (plasma) of high density (about 10^{23} cm^{-3}) and ignore the atom lattice in a first approximation. Such plasma supports propagation of density fluctuation through the volume of the metal, and the minimum propagating frequency is defined as the plasma frequency:

$$\omega_P = \sqrt{ne^2 / m\varepsilon_0} \tag{4.1}$$

where n is the electron density and m the mass of electron. Below the plasma frequency, no propagating waves can exist, which results in the typical properties of a metal, such as being highly reflective and non-transparent. Based on such assumptions, different model have been proposed and more details will be discussed in later sections in this chapter.

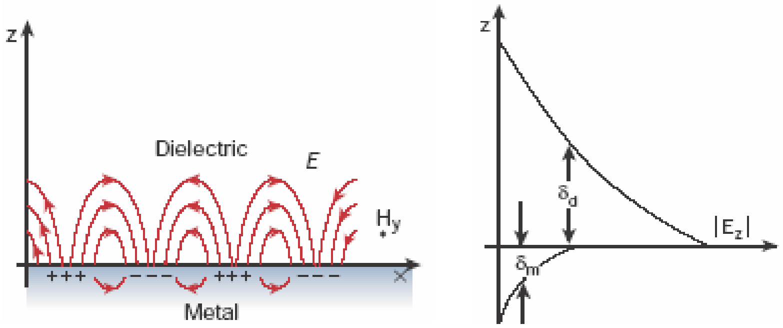

(a) (b)

Figure 4-1: Illustration of surface plasmon.

While the electron density fluctuation may propagate through the bulk of a metal, another interesting wave phenomenon, which can be predicted by the Maxwell's equations, happens at the interface of a metal and a dielectric material. The electrons on a metal surface can exhibit coherent fluctuations caused by, for example, an incident EM wave. Because of the existence of the boundary, net charges are accumulated at the surface, which produces another local EM field in the dielectric side of the interface. Such interaction between the surface charges and the EM field constitutes the SP, which can propagate along the interface, as is illustrated in figure 4-1(a). In contract to the propagating nature of SPs along the surface, the field perpendicular to the surface decays exponentially as it leaves away from the surface, as illustrated in figure 4-1(b). The field in this direction is known as evanescent or near-field in nature. In another word, the EM energy of SPs is trapped at the surface and not radiating. Because of the fact that SPs always involve interaction of trapped light waves with the free electrons of the conductor, they are also often called Surface Plasmon Polaritons (SPPs).

Such wave phenomenon can also be analytically unraveled by solving the Maxwell's equations under the appropriate boundary conditions. Here we briefly go through the derivation to give a more theoretical understanding. From above analysis, we have been aware that such phenomena have to have the requirement of E field normal to the surface to create surface charges. Thus only TM mode is needed in the consideration of two-dimensional scenario. We assume the x-y plane to be the interface plane and the positive z half space as the medium of metal, as shown in figure 4-2.

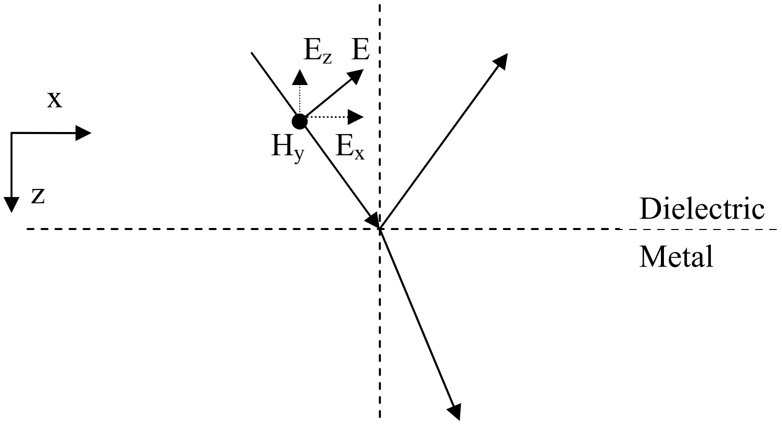

Figure 4-2: Illustration of incidence of light at dielectric and metal material interface.

The TM mode EM fields at the interface are:

$$E_d = (E_{x,d}, 0, E_{z,d}) \exp[i(k_x x + k_{z,d} z - \omega t)] \tag{4.2a}$$

$$H_d = (0, H_{y,d}, 0) \exp[i(k_x x + k_{z,d} z - \omega t)] \tag{4.2b}$$

$$E_m = (E_{x,m}, 0, E_{z,m}) \exp[i(k_x x + k_{z,m} z - \omega t)] \tag{4.2c}$$

$$H_m = (0, H_{y,m}, 0)\exp[i(k_x x + k_{z,m} z - \omega t)] \tag{4.2d}$$

By applying $\nabla \cdot E = 0$ we find

$$E_{z,d} = -E_{x,d}\frac{k_x}{k_{z,d}} \tag{4.3a}$$

$$E_{z,m} = -E_{x,m}\frac{k_x}{k_{z,m}} \tag{4.3b}$$

Now if we use Faraday's law to find the relationship between H_y and E_x we get:

$$H_{y,d} = \omega E_{x,d}\varepsilon_0\varepsilon_d / k_{z,d} \tag{4.4a}$$

$$H_{y,m} = \omega E_{x,m}\varepsilon_0\varepsilon_m / k_{z,m} \tag{4.4b}$$

Finally we know the tangential components of EM fields have to be continuous at the interface. Thus $H_{y,d} = H_{y,m}$ and $E_{x,d} = E_{x,m}$, which leads to the following relationship between the relative permittivities and the normal components of the wavevectors in both media:

$$\frac{\varepsilon_d}{k_{z,d}} = \frac{\varepsilon_m}{k_{z,m}} \tag{4.5}$$

Also we have:

$$k_{z,d}^2 + k_x^2 = \varepsilon_d k_0^2 \tag{4.6a}$$

$$k_{z,m}^2 + k_x^2 = \varepsilon_m k_0^2 \tag{4.6b}$$

where $k_0 = 2\pi / \lambda$. In order to have truly an evanescent wave with exponential decays into both media, both $\exp(ik_{z,d}z)$ and $\exp(ik_{z,m}z)$ terms have to be exponentially decaying term, requiring $ik_{z,d} > 0$ and $ik_{z,m} < 0$. Obviously both $k_{z,d}$ and $k_{z,m}$ have to be imaginary with opposite signs.

Now from our above derivation we can have two important conclusions. First, from equation (4.5), we can see the dielectric functions of the two media have to be of opposite signs. This in fact explains why such phenomena have a dependence on choice of materials. Only metals that have negative dielectric constants can support propagating SPs on their surfaces. More general speaking, materials having no band gap, like metal, or only partial band gap, like semiconductor, can support such surface mode, which may be a propagating one or just a localized surface resonance mode, the collective oscillation of the conduction electrons.

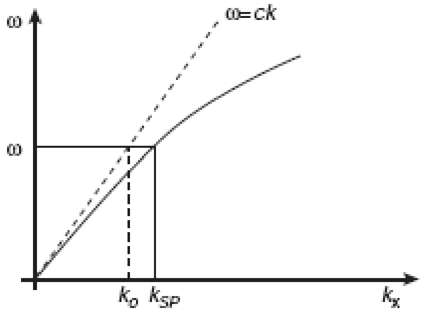

Figure 4-3: Dispersion relation of light (dashed curve) and surface plasmon (solid curve)

Secondly, as $k_{z,d}$ being imaginary, we can conclude from (4.6a) that the surface mode wavevector k_x has to be greater than $\sqrt{\varepsilon_d}\,k_0$, the wavevector of the photon in the dielectric medium. This momentum mismatch is illustrated in figure 4-3 and will have far-reaching effect as we will discuss in the later session of this chapter. By substituting equations (4.6) into (4.5), the surface mode wavevector can be obtained as:

$$k_x = k_0 \sqrt{\frac{\varepsilon_d \varepsilon_m}{\varepsilon_d + \varepsilon_m}} \tag{4.7}$$

Due to scattering by phonons in real metals, the dielectric constants of metals are always having an imaginary component, which results in a complex wavevector predicted by equation (4.7). Assuming $k_x = k_x^{'} + ik_x^{''}$, the propagation length can be found as:

$$\delta_{SP} = \frac{1}{2k_x^{''}} \tag{4.8}$$

Noble metals, such as Au, Ag, are believed to strongly support SPs compared to other metals at visible range. Copper and Aluminum are also good choices at those frequencies. When moving to the infrared region, other metals like Nickel and Platinum are good candidates to support SPs too.

After above introduction of the physics of SPs, the near-field optical enhancement can now be understood. SP modes can also exist on curved surfaces, for example, a sub-micron tip structure. These modes are, contrary to what we discussed above for planar surface, radiative, i.e., the curved surface couples the modes with photons. Thus the dependence of near-field enhancement on factors such as polarization, material and wavelength becomes naturally explainable.

4.1.2 Excitation of Surface Plasmon by Light

Surface plasmons can be excited by either fast electrons or light. For the scope of this dissertation, I only focus on the later. As we mentioned before, the SPs cannot be directly excited by light due to their momentum mismatch. Additional momentum has to be provided to bridge the gap. There are usually two methods for this purpose.

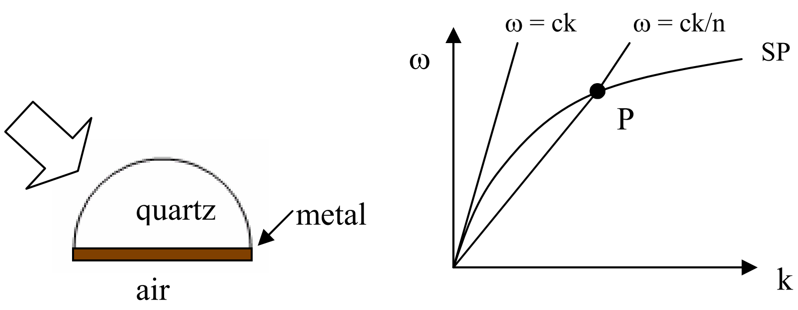

Figure 4-4: Excitation of surface plasmon via ATR.

First is via Attenuated Total Reflection (ATR) coupler, as illustrated in figure 4-4. In such quartz/metal/air structure, the horizontal momentum of light at quartz/metal interface is:

$$k_x = \frac{\omega}{c} n_{quartz} \sin\theta \tag{4.9}$$

Since the light line now lies to the right of SP up to point P, light can now excite SPs with the same frequency at the right angle of incidence on the metal/air interface. SPs at quartz/metal side still cannot be excited directly by light.

The second method is via gratings. Grating structures can provide stationary momentum of $m\frac{2\pi}{a}$, where m is an integer and a the grating constant. The dispersion relation now becomes:

$$k_x = \frac{\omega}{c}\sin\theta \pm m\frac{2\pi}{a} = k_{SP} \tag{4.10}$$

More generally, any perturbation in the smooth surface, such as a tip structure, can provide additional momentum to bridge the momentum gap so that the SP can transform into light, or vice versa. Such photon-SP coupling via nanostructures is the fundamental mechanism of my study.

4.1.3 Extraordinary Transmission through Perforated Metal Films

Recent research has shown that photon-SP coupling has the potential to overcome the two fundamental constraints in manipulating light at sub-wavelength scale: transmission and diffraction. According to traditional diffraction theory, the transmission efficiency of a single sub-wavelength aperture is predicted to scale as $(r/\lambda)^4$ [1], where r is the hole radius. Accordingly, for a hole of 150 nm diameter, one would expect transmission efficiency on the order of 10^{-3} to10^{-4} at visible range. In addition, the intensity (I) of the transmission from a grating is proportional to the inverse of wavelength [2].

In 1998, a paper published in Nature regarding transmission through perforated metal film surprised the community of optics. In that study [3], a silver film of about 200 nm thickness was deposited by evaporation onto a quartz substrate. A variety of two-dimensional arrays of cylindrical holes having different hole diameters and spacing periods were prepared in the films by Focused Ion Beam (FIB) and transmission spectrum of such perforated metal films was analyzed. The zero-order transmission spectra, where the incident and detected light are collinear, were recorded with spectrophotometer with both coherent and incoherent light sources.

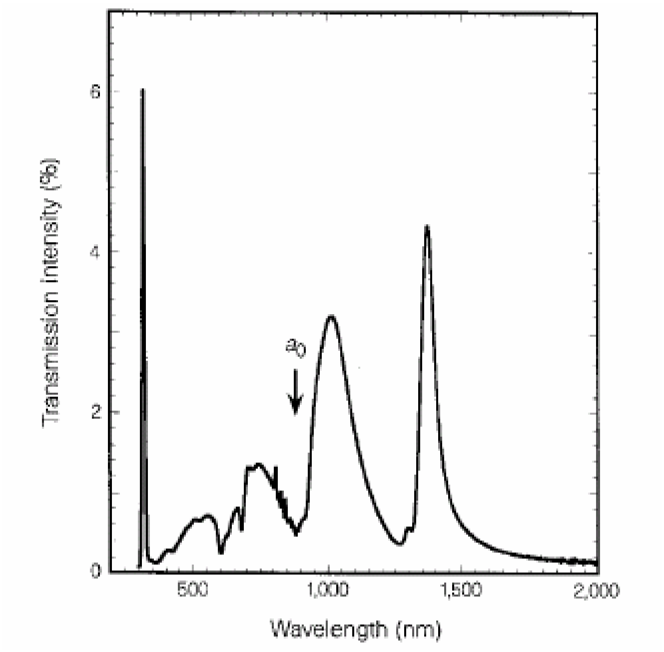

Figure 4-5: Zero-order transmission spectrum of an Ag array (period a_0: 0.9 μm, diameter: 150 nm, thickness: 200 nm) [3].

Figure 4-5 shows a typical zero-order transmission spectrum for a square array of 150nm holes with a period of 0.9mm. The spectrum shows a distinct peak at $\lambda = 326$ nm, which disappear as film thickness increases. Interestingly, the peaks of the spectrum become gradually stronger at longer wavelengths. Two noticeable minima happen at wavelength of a_0, and $a_0\sqrt{\varepsilon}$ respectively, where a_0 is the periodicity of holes array and ε is the dielectric constant of the quartz substrate. The maximum transmission intensity occurs at 1370 nm, which is nearly ten times the diameter of an individual hole in the array. Remarkably, if the light transmission is normalized by the surface area of the holes, the transmission can reach more than one. This indicates that even the light impinging on the metal surface between the holes is also transmitted. Furthermore, the transmission of the hole array scales linearly with the surface area of the holes. All these features are surprisingly remarkable considering the theory we have known from traditional diffraction for centuries. The results indicate that there is additional active element besides the simple passive geometries.

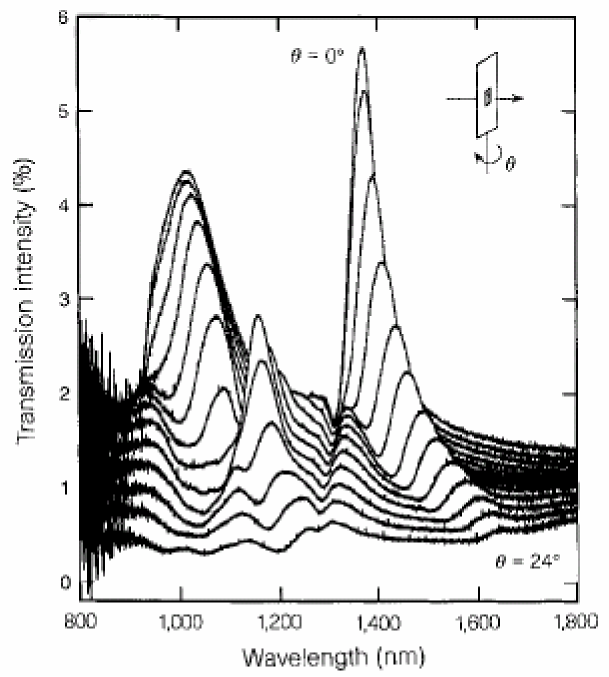

Figure 4-6: Zero-order transmission spectra as a function of incident angle of the light. Data were taken every 2 degree for a square Ag array (period a0: 0.9 μm, diameter: 150 nm, thickness: 200 nm) [3].

In order to understand the origin of this phenomenon, authors of the paper tested the dependence on all the possible variables such as holes diameter, periodicity, thickness and type of metal. They discovered that the periodicity of the array determines the position of the peaks, while the width of the peaks appears to be strongly dependent on the aspect ratio (depth divided by diameter) of the cylindrical holes. The authors related the phenomenon to surface plasmons after two important clues observed from their experiments. First is the absence of enhanced transmission in holes arrays fabricated in Germanium films, which points out the importance of metallic film. The other is the angular dependence of the spectra in metallic ones. Figure 4-6 illustrates the zero-order transmission as a function of incident angle, where data were recorded every 2 degree up to 24 degree. It clearly indicates that the spectra change in a marked way even for very small angles. The peaks in spectra change in intensity and split into new peaks moving in opposite directions, which is exactly the behavior observed when light couples with SPs in reflection gratings [4].

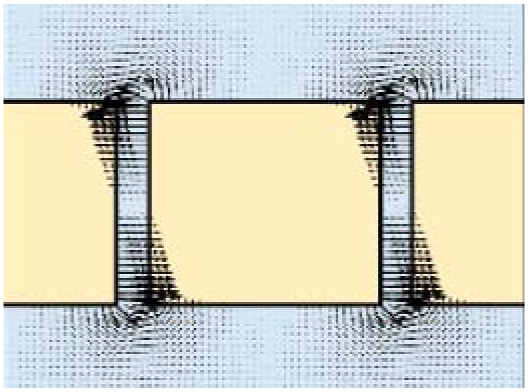

Figure 4-7: Calculation of light through a slit. Arrows represent the direction and strength of electric fields [5].

This paper triggered tremendous research interest in understanding the mechanism underneath the enhanced transmission and SP-light coupling. As explained earlier in the chapter, the surfaces of materials having negative ε are characterized with EM modes different from those in the bulk. Unlike bulk modes, the surface modes can couple to external transverse radiation and have extremely high density in the immediate vicinity of the surface. Pendry [5] realized that light can couple to the surface modes of the metal that are very closely confined to the surface. Therefore light find it much easier to filter through the tiny holes like it is sucked through the film, as seen in their calculation. Inside the slit, huge enhancement of fields is observed, which is typical of highly curved surface that can trap surface mode as local resonance.

The zero-order transmission spectra exhibit well-defined maxima and minima, the position of which is dependent on the periodicity and aspect ratio of the holes array. Ghaemi et al. [6] show that the minima are the collection of loci for Wood's anomaly, which occurs when a diffracted beam becomes tangent to the film, and that the maxima are the result of a resonant excitation of surface plasmons.

Popov et al. [7] took into account the existence of the two-dimensional holes array in their modeling and develop a two-dimensional analysis of the experimental results without simplification. Their work has demonstrated the existence of a channel for the transmission of light that cannot be predicted by one-dimensional models.

Martín-Moreno et al. [8] present a fully three-dimensional theoretical study of the extraordinary transmission of light through sub-wavelength holes array in optically thick metal films and results matched very well with experimental data. An analytical minimal model was also developed, which conclusively shows that the enhancement of transmission is due to surface plasmons formed on each metal-dielectric interface. Different regimes of tunneling were found depending on the geometrical parameters defining the system. For thin films the tunneling is resonant through closely coupled SPs, while for large thicknesses, the photon hops from SP to SP, with the tunneling being sequential. The ability of SPs to transmit and focus light efficiently is not restricted to this particular geometry.

Collin et al. [9] calculated the complex photonic band gap of transmission metallic gratings with rectangular slits. The results show pronounced discontinuities located on Wood's anomalies and reveal unambiguously two different types of resonances, which are identified as horizontal and vertical surface-plasmon resonances, illustrated in Fig 4-8. While the vertical SP mode can be guided through the slits, the horizontal SP mode can directly couple to SP on the other side of the film. Once the SPs reach the other side of the metallic film, it re-emits light.

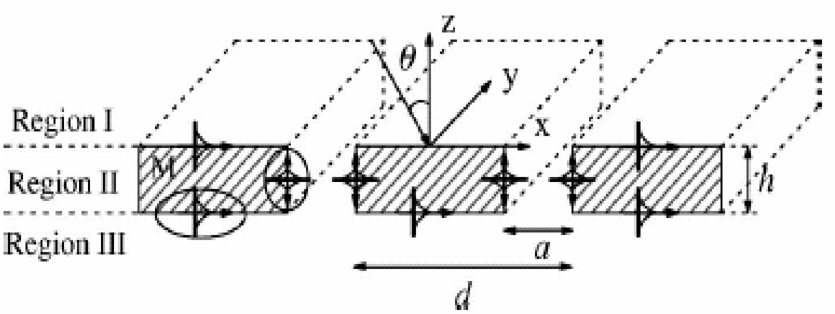

Figure 4-8: Horizontal and vertical surface plasmons on metallic grating.

Barns et al. [10] present results of the transmitted, reflected, and absorbed power associated with the enhanced transmittance of light through a sample under different polarization conditions. The transmission features are consistent with the TM mode resonant from experimentally acquired dispersion curves. In the zero-order regime transmission maxima are associated with reflectivity minima and with absorbance maxima. All observations are consistent with the view that SPP modes act to enhance the fields associated with the evanescent waves, thus providing a way to increase the transmittance. In addition, the authors note that enhanced transmittance might also occur through the involvement of other surface waves such as surface phonon polaritons.

4.1.4 Surface Plasmon Lithography

The remarkable transmission of the SP waves through pierced metallic films has a potential to pattern nanoscale features using conventional photolithography technique to overcome the diffraction limit. There have been some research efforts in these areas. Here I review two representative approaches that have been experimentally demonstrated.

Srituravanich et al. [11] demonstrated plasmonic nanolithography by utilizing SPs transmitted through sub-wavelength 2D holes array masks. Their plasmonic mask designed for lithography in the UV range is composed of a perforated aluminum film, which is believed to most strongly support SPs at UV wavelength. Quartz is employed as the mask support substrate, and a very thin spacer layer of polymethyl methacrylate (PMMA) is used as the matching dielectric material. As a proof of the concept, a negative near-UV photoresist (SU-8) is directly spun on the plasmonic mask. A sub-100 nm dot array pattern on a 170 nm period has been successfully obtained using an exposure radiation of 365 nm wavelength. The authors also investigated the effect of the holes array period and the spacer thickness. Although the authors claim that the concept of plasmonic lithography applies not only to periodic structures but also to arbitrary shapes, the experimental demonstration is still under investigation.

Luo et al. [12] proposed and experimentally demonstrated a sub-100 nm line width photolithography by utilizing surface plasmon polaritonic interference in the optical near field excited by a wavelength of 436 nm. The basic principle of the method is based on the idea that with the aid of a periodic corrugation, illumination light can couple with surface plasmon to obtain a new state named SPP. The interference of SPP can result in a strongly enhanced nanoscale spatial distribution and expose the thin layer of photoresist directly below the mask. The features on the mask have a periodicity of 300 nm, and the opening is 1/5 of the periodicity. Both their simulation and experiment results show that the near-field emission pattern with the wavelength around the SPP resonance has a different periodicity from that of the opening features on the mask. The features on the photoresist have a periodicity of 100 nm and the line width is about 50 nm. Most of the light transmitted is not only found at the locations below the aperture but also below the metal surfaces. Since the illuminating source is not only the light directly emitted from the aperture but the optical near-field produced by SP interference, the pattern produced in this approach is not one-to-one matched with mask pattern. And again, arbitrary patterning is still not demonstrated.

4.2 SURFACE PLASMON ASSISTED NANOLITHOGRAPHY (SPAN)

It is desirable to have a photolithography scheme that can have arbitrary nano-scale patterning capability while the system setup remains as simple as possible. In order to reach that purpose, the two fundamental issues of light at sub-wavelength scale, transmission and diffraction, have to be resolved to certain extent. The discovery of enhanced transmission through perforated metal film and the understanding of the mechanism behind this phenomenon have paved a way to overcome the transmission issue by utilizing SP-light coupling. So now the question is: can SP-light coupling be utilized to resolve the diffraction issue?

In this chapter, I present a nanolithography scheme utilizing SP-light coupling to overcome the two fundamental issues. The scheme is discovered first by FDTD modeling and then demonstrated in experiments. Later the mechanism behind is made clear by numerical investigation. The surface plasmons excited on the mask enhance the light through the sub-wavelength aperture, while the surface plasmons excited on the substrate help to confine the light intensity to the space behind the mask aperture by coupling to the light. Improvements are achieved in more experimental results.

4.2.1 FDTD Modeling for SPAN

Photoresist behaves somewhat like a thresholder, for which only if incident optical radiation is above a critical intensity that the photochemical reactions are activated. Below the threshold, the resist can be exposed for a relatively long time without any changes. In fact, some simple models for resist simply use a threshold level, for example 0.5. The 0.5 contour of the optical intensity can roughly gives us the idea of the photolithography results.

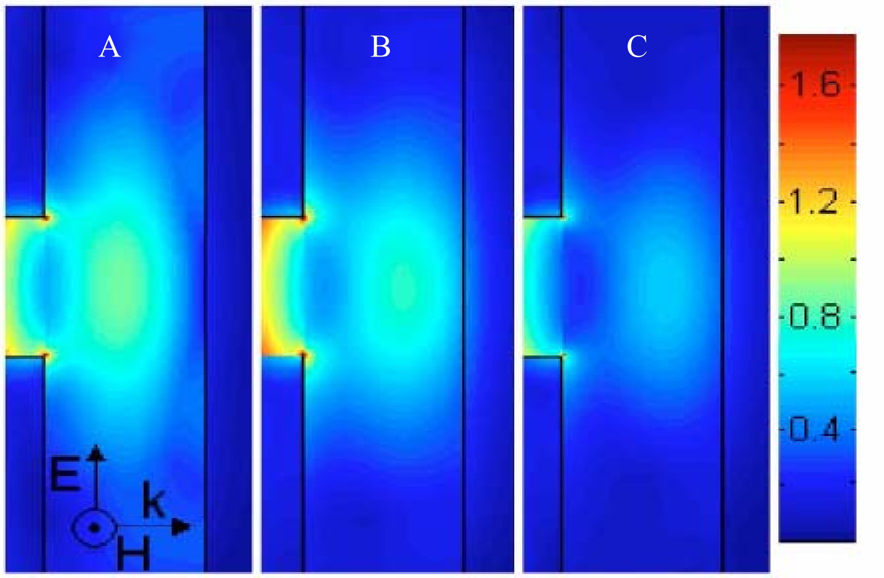

Figure 4-9: FDTD simulation results of electric-field distribution in the photoresist with: A) a gold mask and bare silicon substrate, B) a gold mask and Ti shield on a Si substrate, C) a Ti mask and Ti shield on a Si substrate.

By FDTD modeling I studied and compared three cases, as shown in Fig 4-9. In case A, a gold mask is used for a photoresist thin film on a Si substrate. In case B, a thin Ti layer of about 80 nm is used in between the photoresist and the Si substrate. In case C, both the metal mask and the thin film on the substrate are made of Ti. The reason we introduced such Ti layer, which we call shield layer as explained later, is following the idea that people found that SPs excited on a thin noble metal layer, for example silver, can have focusing effect. The EM waves, both propagating waves and evanescent waves, from a near-field object can be collected by the film with proper amplification to the opposite side to form an image with a resolution far beyond diffraction limit.

As shown in the simulation results, for a bare silicon substrate, not only does the light spread in the lateral direction, but its intensity at the interface between the photoresist and substrate is significantly weakened. This explains why photolithography does not work well with a bare silicon substrate. There is no pattern transfer when the light is weak (the photoresist at the interface is not photoinitiated and washes away during development). On the other hand, when the light intensity is high, the pattern will be significantly oversized. By using the Ti shield layer, the light intensity is well confined behind the aperture. Since the penetration depth of titanium at 355 nm wavelength is about 30 nm, the 80 nm thick titanium layer is thick enough to absorb the light as it reaches the silicon substrate. Thus, the Ti layer acts like a shield and the optical properties of the substrate are not important to the lithography results. We believe this lithography scheme can work for any substrates.

The combination of Ti mask and Ti shield seems to have the best effect for the application of photolithography as shown in fig 4-9C.

4.2.2 Experimental Setup

The schematic representation of the setup is shown in Fig 4-10. A polarized laser beam of 355 nm wavelength was used as the light source to expose an 80 nm thick photoresist on an 80 nm Ti film deposited by E-beam evaporation on a silicon substrate. For demonstration of the concept at that stage, we used a grating mask that has a 100 nm aperture width with periodicity of 1 μm or 500 nm, which was almost the nominal resolution of the EBL machine we used. The nanolithography mask was fabricated by first patterning lines of 950 K po1ymethylmethacrylated (PMMA) on a quartz substrate using EBL. The quartz mask we used has a layer of Indium Tin Oxide (ITO) of about 100 nm thickness to facilitate the E-beam writing of PMMA on the quartz substrate. The ITO layer accounts for the roughness of the mask pattern shown in Fig 4-10.

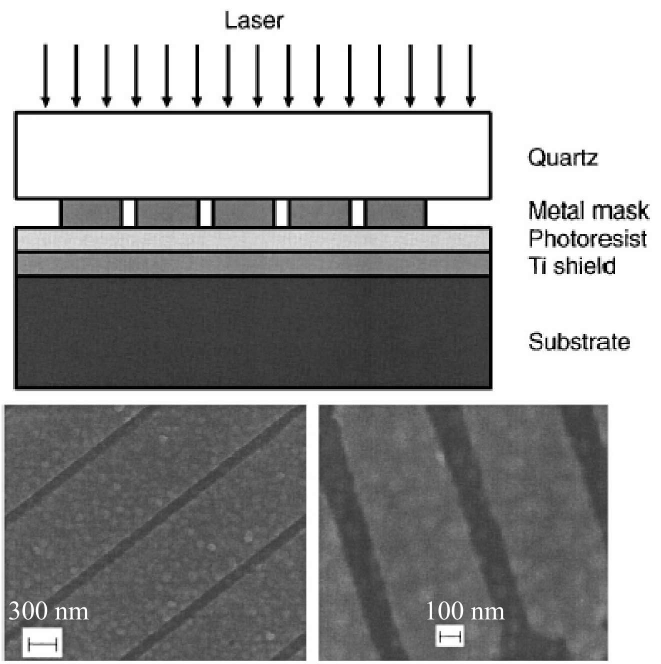

Figure 4-10: Schematic view of SPAN scheme and SPAN masks fabricated using EBL.

Because of the small line-width as well as the high density of the pattern, the EBL patterns were greatly affected by two issues. First, the PMMA lines tended to expand due to absorption of chemicals during development, which was more severe because of the high surface-volume ratio in our case. Secondly, the E-beam proximity effect was very obvious due to the high density patterns. By adoption of E-beam dosage modulation and weaker developer, isopropyl alcohol (IPA) instead of methyl isobutyl ketone (MIBK), the above two issues were significantly alleviated. The mask was then obtained by depositing 70 nm gold or titanium using electron-beam evaporation and lift off. Each mask pattern consists of two sets of line apertures perpendicular to one another.

SU-8 (Microchem®), a negative near-UV photoresist (refractive index 1.67) was spun on the Ti-coated silicon substrate to a thickness of 80 nm. During our photolithography experiments, the polarization of the laser light was always kept in such a direction that one set of lines was parallel to the light polarization, while the other perpendicular. The laser light source is first adjusted to desirable intensity and wait for some time for stabilization. After exposure, the sample is developed in SU-8 developer for 40 seconds and gently dried by air.

4.2.3 SPAN Results with Coherent Light Source

Figure 4-11 shows Atomic Force Microscopy images of the photoresist line pattern after exposure at an energy density of approximately 90 W/m^2 for about 50 seconds. For the gold mask, the line pattern was transferred only with the TM mode to a linewidth of 200–300 nm. For the titanium mask with 1 μm periodicity, both the parallel and perpendicular line patterns, with respect to the laser polarization, were formed with a width of approximately 200 nm. The TM mode has a linewidth slightly larger than the TE mode. The 500 nm periodicity pattern is also well defined in the photoresist and the TE mode has a linewidth of about 130 nm. Since the intensity of the pulse laser we were using is fluctuating strongly, it’s hard to monitor the accurate dosage for the above two cases. We believe if we can better control the light energy, the linewidth can be further decreased.

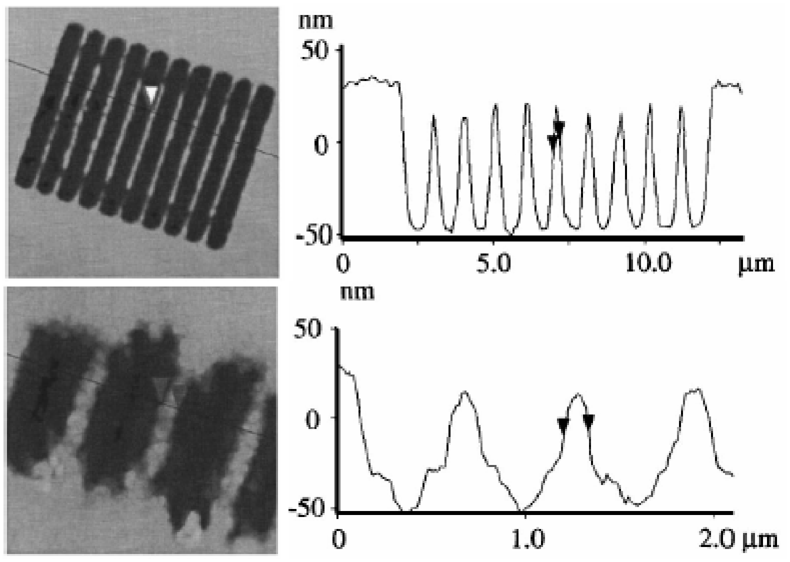

Figure 4-11: AFM results of close view and cross section view of the photoresist patterns with a) 1 µm periodicity and b) 500 nm periodicity using Ti mask and Ti shield.

We also varied the lithographic process by changing laser intensity and dosages for the TM mode gold mask, as seen in Figure 4-12. As the intensity and dosage increase, the cross section of the lines perpendicular to the laser polarization significantly changed. At laser intensity of about 120 W/m^2 of 1min, the photoresist lines became 300–400 nm in width and two peaks formed across the section Fig 4-12(b). The distance between the two peaks is about 200 nm. At this intensity level, there was still no pattern transfer parallel to the laser polarization (TE mode). When the energy density was further increased to about 200 W/m^2 and exposure time of 3 minutes, the surface plasmon interference effect became significant (Fig 4-12C). Additional lines formed between lines of larger height and width. At this intensity level, the lines started to form for TE mode but were poorly defined having a noticeable interference effect.

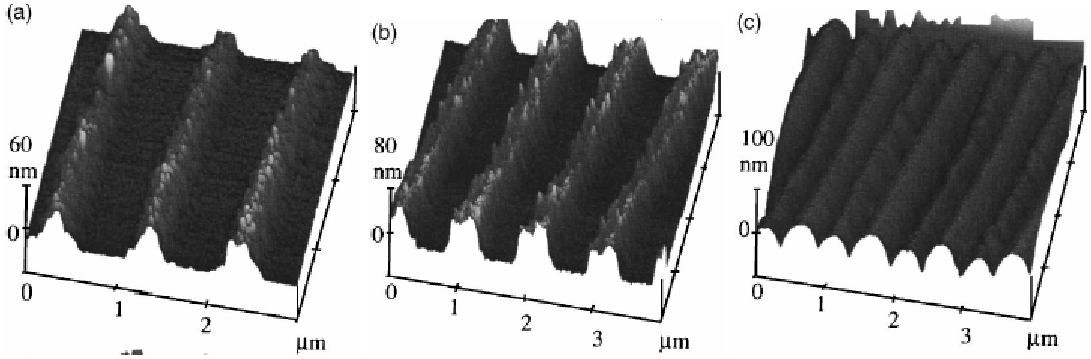

Figure 4-12: AFM results of photoresist patterns at different energy density and dosage with gold mask and Ti shield. Photoresist lines perpendicular to polarization with a) 50 s at 90W/m^2, b) 1 min at 120 W/m^2, and c) 3min at 200W/m^2.

4.2.4 FDTD Modeling of Surface Charge Oscillation

In order to better understand the mechanism that lies behind, more FDTD modeling were conducted. Other mask/shield material combinations were also tested numerically. It has been shown from the FDTD results that the shield material is more crucial than the mask material in terms of line-width control in this application. Perhaps due to their relatively low refractive index (1.30 for Ti and 1.33 for Cr at 355 nm), titanium and chromium are the best, in terms of confining light intensity, among the many metals commonly used. However, no sufficient light confinement was achieved when we changed the shield material to an artificial dielectric material (e.g., refractive index 1.3) in the model, indicating the important contribution from free electron plasma.

When the plane wave incident light encounters the metal mask or shield, the electric fields, Ex and Ey, drive the free electrons in the metal and produce a harmonically oscillating surface charge at the surface. By integrating the current flowing in and out of each cell in FDTD computational domain, we can calculate the charge density distribution. As shown in Fig 4-13, the charges are having symmetric amplitude across the centerline of the aperture, but they always have π phase difference, meaning the charges on each side always have opposite signs. The charge oscillation on the mask metal facilitates light transmission through the aperture. Meanwhile, the opposite charges on the shield surface produce an electric field that counter-acts on the incoming electric field emitted from the aperture. This strongly helps in preventing light intensity spreading in lateral directions and interacting with adjacent electric fields exited from neighboring apertures. In this manner high density patterning becomes feasible. In fact simulations show that the periodicity of the aperture can be further decreased until the surface plasmons excited on the shield layer start to interfere with each other, as shown in Fig. 4-13, which has a periodicity of 150 nm. Below that, FDTD simulations show that the light intensity inside the resist starts to lose contrast.

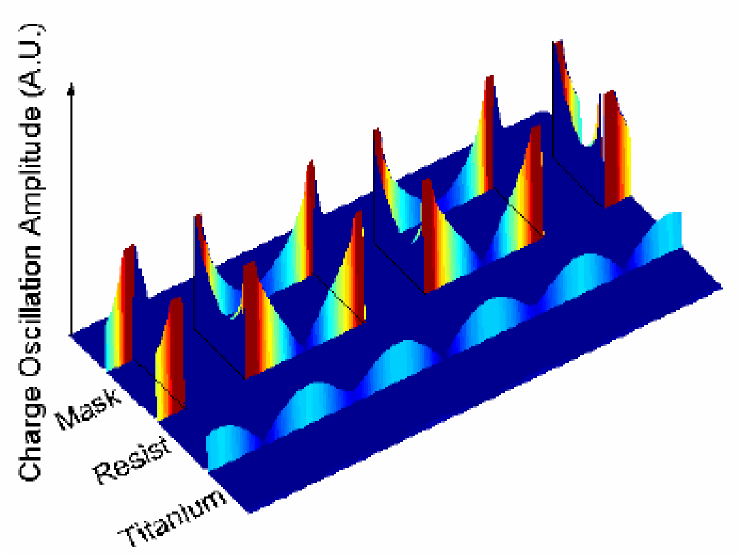

Figure 4-13: Charge oscillation amplitude distribution with metal mask and Ti shield.

4.2.5 High Density SPAN Using UV Light

We also investigated the possibilities to conduct SPAN using light from mercury lamp, which is the light source used in traditional photolithography. The ultraviolet light from the mercury lamp has a spectrum with several peaks and the maximum peak is centered at 365 nm with a full width at half maximum (FWHM) of about 20 nm. The wide emission spectrum made the photolithography using mercury lamp quite complex, especially for a silicon substrate. Although the optical properties of metals, for example titanium, do not vary significantly across the UV range, the optical properties of silicon change dramatically (Shown in table 4.1 below) [13]. Since the optical penetration depth of UV light in titanium is only about 30 nm, we believe that by using a titanium shield layer of approximately 60 nm the variation of optical properties of silicon across the UV emission spectrum should not be an issue any more.

	Refractive index (n)	Extinction Coefficient (k)
Ti @ 354 nm	1.3	2.01
Ti @ 376 nm	1.44	2.09
Si @ 354 nm	5.61	3.01
Si @ 376 nm	6.71	1.32
Al @ 354 nm	0.385	4.30
Al @ 376 nm	0.432	4.56
Ag @ 354 nm	0.209	1.44
Cr @ 354 nm	1.33	3.18

Table 4-1: Optical properties of some materials used in the study.

For the demonstration of SPAN using UV lamp, we fabricated new mask using an advanced EBL machine. The mask pattern is consisted of both grating structures and an arbitrary shape, a ring aperture as shown in Fig 4-14. The gratings have aperture width of 80 nm with different periodicity (200 nm or 400 nm) and number of apertures. Again because of the ITO layer, the mask patterns display noticeable roughness compared to the size of the aperture.

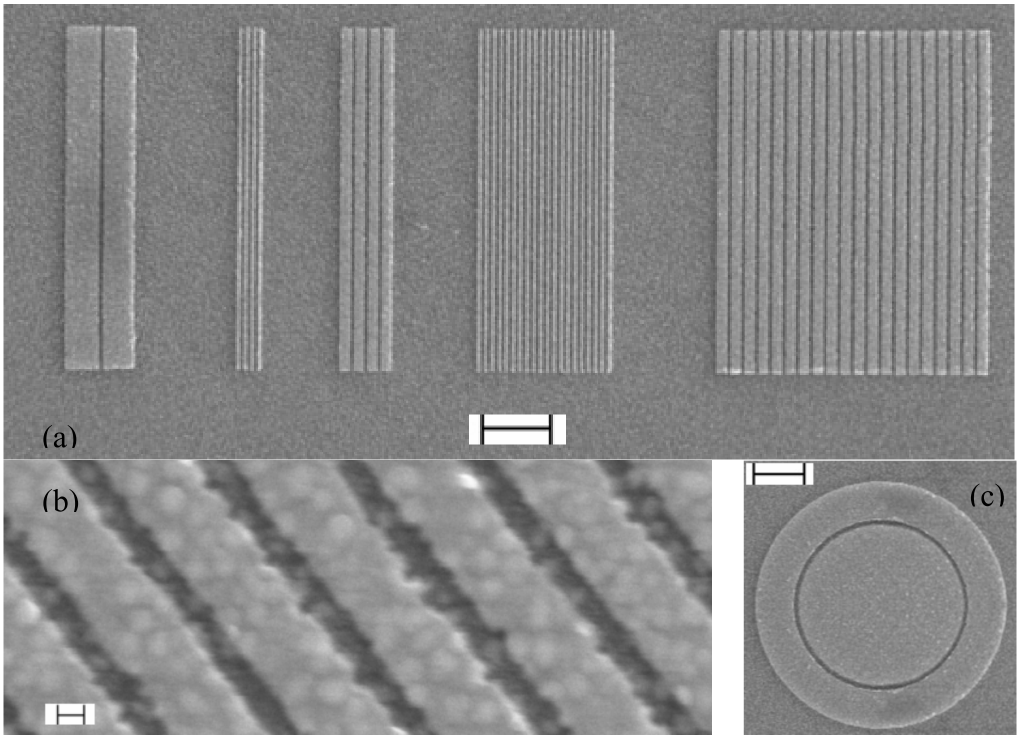

Figure 4-14: Ti mask pattern used for SPAN with UV light. (a) Overview of grating structures used for SPAN, scale bar = 2μm. (b) Close view of a grating structure with 80 nm aperture and 400 nm period, scale bar = 100 nm. (c) Close view of a ring aperture, scale bar = 2μm.

Also, by using an un-polarized light source, the polarization dependence of SPAN is minimized. No matter how the mask pattern is aligned, it can always receive the TM mode component from the un-polarized light source. Further detailed discussions about comparison between laser light and UV light (coherency, polarization and wavelength spectrum) can be seen in the next chapter.

During lithography, the mask and sample, which is silicon substrate deposited with an 80 nm Ti shield layer and an 80 nm photoresist layer sequentially, were hold in close contact by applying some pressure using home made gadget. The exposure was done in a UV aligner (Karl Suss, 1000) for 2 minutes. The sample was then directly developed in SU-8 developer for 40 seconds and gently dried by air gun.

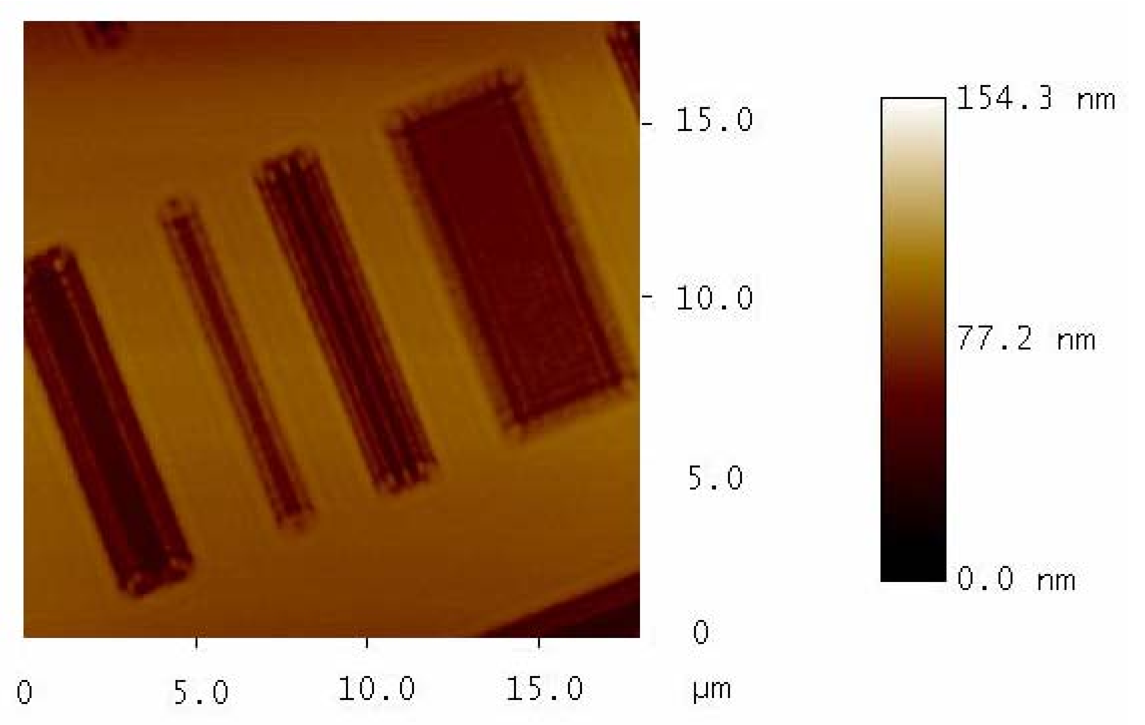

Figure 4-15: AFM characterization of lithography results with grating mask.

The lithography results for grating mask vary depending on both number of apertures and periodicity. For grating mask patterns that have a period of 200 nm, the lithography resulted in almost no contrast (pattern 2 and 4 from left in Fig 4-15). In this case, the FDTD modeling has predicted satisfying contrast, although the periodicity is at the minimum limit. Considering the severe defects we have in the mask, this result is not very surprising. The pattern of gratings that have a period of 400 nm were transferred fairly well for different number of apertures, as seen in both Fig 4-15 (pattern 3 from left) and Fig 4-16. From Fig 4-16, the AFM results show that the pattern in the resist has a height of about 35 nm, which I believe is partly due to the shrinkage of SU-8 during development.

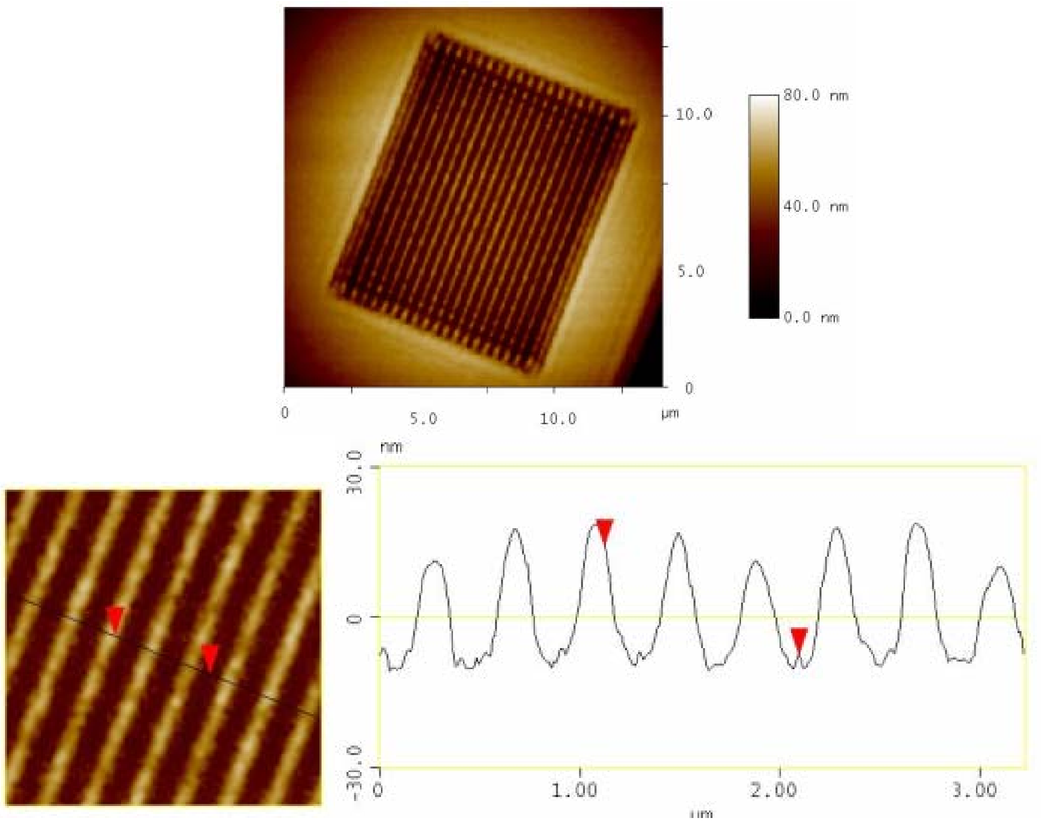

Figure 4-16: Lithography results with grating mask (period 400 nm).

The pattern of single aperture was not transferred to the resist, as seen in Fig 4-15 (pattern 1 from left). This is somewhat surprisingly interesting. According to my FDTD modeling, both single aperture and aperture array can have good light confinement, with slightly difference in contrast. There might be two reasons to explain this unexpected result. First, in both modeling and experiment, the termination of mask pattern at the ends on each side of the single aperture may physically place an actual period for the pattern in both modeling and experiment. These two periods could easily be different without notice, which results in the discrepancy. Second, although the single aperture may be able to confine the light similarly compared to an aperture array, it may not be efficient in collecting the light impinging on it, thus requiring more time of exposure. Last but not the least, the imperfectness of mask apertures (e.g. the roughness) was not accounted in simulation.

Noticeable boundary effect can be seen for all the grating patterns mentioned. This effect seems similar to the proximity effect in E-beam lithography and photolithography, which is already understood and can be corrected by certain design correction rules. However, interestingly, in our case the lithography results at the boundary are enhanced rather than weakened as most commonly seen in optical/E-beam proximity effect. Also, an additional line is observed on each side of the polymer grating pattern. The additional features can also be seen in the SPAN result for a ring aperture mask, as is shown in Fig 4-17. The mask ring pattern has an outer diameter of 10 μm and the ring aperture of 6.5 μm in diameter. The pattern in the resist has an outer diameter of 10 μm too, however not only there are several ring structures produced in the photoresist, the primary ring in the resist has a diameter slightly different from that of the ring aperture in the mask.

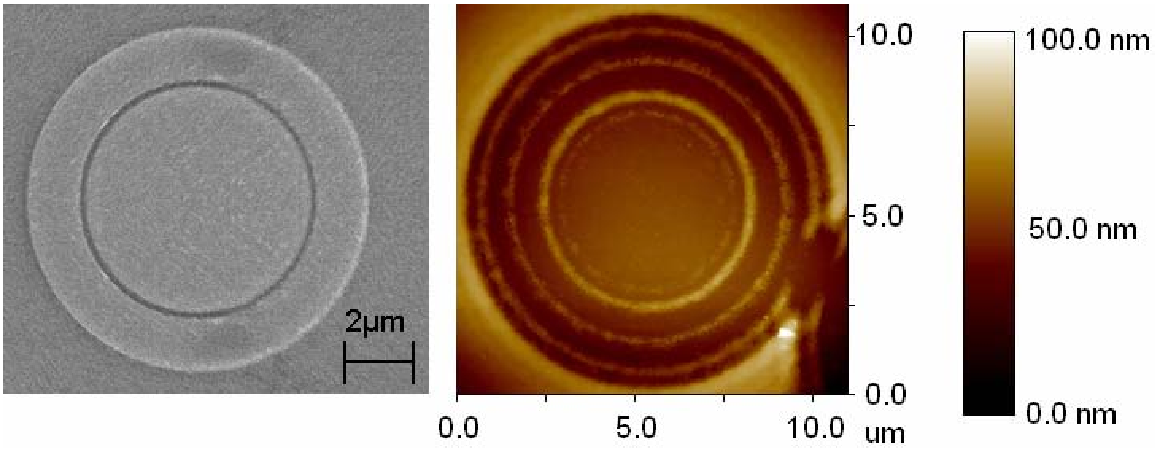

Figure 4-17: a) SEM image of ring aperture, scale bar 2 μm. b) AFM characterization of lithography results with ring aperture.

We believe these interesting phenomena can be explained by the propagating and interference of SPs on the metal film surface. Further investigation in this can help better understand the mechanism of surface plasmon in SPAN and to create design rules to minimize the boundary effect.

4.2.6 Discussion

As discussed previously, the Ti shield layer is crucial in SPAN. It helps to focus the light intensity in the photoresist to achieve high density nano scale patterning. Also, the 80 nm thick titanium shield is thick enough to absorb the light as it reaches the substrate since the penetration depth of titanium at 355 nm wavelength is about 30 nm. Thus, the optical properties of the substrate are not important to the lithography results and virtually any substrates can be used. Once the patterns form in the photoresist, the titanium shield layer can be patterned and used as a metal mask to pattern the underneath substrate.

Right now the minimum line width demonstrated in our experiments is still only about 100 nm. Even if the lines can be smaller, say 80 nm, the roughness of the line, which is the result from the roughness of mask pattern, made it hard to characterize the difference. Although it is already a fairly good achievement considering the light source we were using and the defects in our SPAN mask, there are still room to improve for SPAN in terms of minimum line width. The feature size using such method could be further scaled down, limited theoretically by the validity of the dielectric function of the material, and practically by the fabrication of the mask. The former limit indicates that it can reach a dimension on the order of 20 nm, however, that would place a very critical requirement on the mask fabrication. By improving the SPAN mask quality, for example polarization of the mask substrate, we believe the lithography results can be significantly improved.

4.3 SUMMARY

In this chapter, I investigated sub-wavelength scale light confinement by utilizing SP-light coupling and demonstrated that photolithography resolution can be extended to a sub-wavelength scale by exciting surface plasmons simultaneously on both a metallic mask and a substrate. Without any additional equipment or added complexity to mask design, one-to-one pattern transfer has been achieved. Both polarized laser beam of 355 nm wavelength and UV light source were used as light source to photoinitiate an 80 nm thick photoresist on a silicon substrate coated with titanium of 80 nm thickness. Simulation results by the finite difference time domain method have predicted the results and also revealed the contribution of surface plasmons excited on both the metallic mask and the Ti shield in helping to spatially confine the light. The lithography scheme discussed in this chapter offers a convenient, low cost, and massive pattern transfer method for nanofabrication need. The feature size using such method could be further scaled down, limited theoretically by the validity of the dielectric function of the material, and practically by the fabrication of the mask.

Reference

1. H. A. Bethe, “Theory of Diffraction by Small Holes,” *Physical Review.* **66,** 163–182 (1944).
2. M. Born, E. Wolf, *Principles of optics : electromagnetic theory of propagation, interference and diffraction of light* (Cambridge University Press, New York, ed. 7th expanded, 1999).
3. T. W. Ebbesen, H. J. Lezec, H. F. Ghaemi, T. Thio, P. A. Wolff, "Extraordinary optical transmission through sub-wavelength hole arrays," *Nature*, **391**, pp.667-669 (1998).
4. H. Raether, *Surface plasmons on smooth and rough surfaces and on gratings*, Springer tracts in modern physics; 111. (Springer-Verlag, Berlin; New York, 1988).
5. J. Pendry, "Applied physics - Playing tricks with light," *Science*, **285**, pp.1687-1688 (1999).
6. H. F. Ghaemi, T. Thio, D. E. Grupp, T. W. Ebbesen, H. J. Lezec, "Surface plasmons enhance optical transmission through subwavelength holes," *Physical Review B*, **58**, pp.6779-6782 (1998).
7. E. Popov, M. Neviere, S. Enoch, R. Reinisch, "Theory of light transmission through subwavelength periodic hole arrays," *Physical Review B*, **62**, pp.16100-16108 (2000).

8. L. Martin-Moreno *et al.*, "Theory of extraordinary optical transmission through subwavelength hole arrays," *Physical Review Letters*, **86**, pp.1114-1117 (2001).
9. S. Collin, F. Pardo, R. Teissier, J. L. Pelouard, "Strong discontinuities in the complex photonic band structure of transmission metallic gratings," *Physical Review B*, **63**, pp. 033107 (2001).
10. W. L. Barnes, W. A. Murray, J. Dintinger, E. Devaux, T. W. Ebbesen, "Surface plasmon polaritons and their role in the enhanced transmission of light through periodic arrays of subwavelength holes in a metal film," *Physical Review Letters*, **92**, pp.- (2004).
11. W. Srituravanich, N. Fang, C. Sun, Q. Luo, X. Zhang, "Plasmonic nanolithography," *Nano Letters*, **4**, pp.1085-1088 (2004).
12. X. G. Luo, T. Ishihara, "Surface plasmon resonant interference nanolithography technique," *Applied Physics Letters*, **84**, pp.4780-4782 (2004).
13. E. D. Palik, *Handbook of optical constants of solids*, Academic Press handbook series. (Academic Press, Orlando, 1985).

Chapter 5: Surface Plasmon Assisted Three-dimensional Nanolithography (3D-SPAN) for Periodical Multilayer Nanostructures

5.1 THREE DIMENSIONAL PERIODICAL NANOSTRUCTURES

The past decade has witnessed intensive research efforts related to photonics. The term ‘photonics’ describes a technology whereby the transmission, control, manipulation and storage of data using photons, the basic building blocks of light. A photonic device may be superior to an electronic one based on the following two simple facts. First, an electric current flows much slower than light. This limits the rate at which data can be exchanged over long distances, and is one of the factors that led to the evolution of optical fiber. By applying some of the advantages of visible and/or IR networks at the device and component scale, a photonic device might operate faster than a conventional electronic one. Secondly, light beams, unlike electric currents, can pass through each other without interacting. On the other hand, electric currents have to be guided around each other, and this makes three-dimensional wiring necessary. Thus an optical device, besides being possible to run much faster than an electronic one, might be smaller at the same time.

However, to achieve functional photonics device, novel photonic materials are needed just like dielectric materials, semiconductor and metals for electronics. Also, novel photonics integration techniques are critical for this goal. The interaction of light with a material can be described by the material's refractive index or dielectric constant. Yablonovitch [1] and John [2] were the first to realize that setting up a periodic refractive index can result in a similar 'band theory' for photons where certain frequencies cannot propagate. Such a material would be the photonic equivalent of an insulator. However, visible light has a much longer wavelength than electrons, several hundred nanometers as opposed to around 0.1 nanometers. In order to see diffractive effects of light the artificial "atoms" must have a much larger scale. Photonic band gap (PBG) materials, also known as photonic crystals (PhCs), are micro/nano-structured materials in which the dielectric constant is periodically modulated on a length scale comparable to the working wavelength. Since the introduction of the concept in 1987, a lot of efforts, both theoretical and experimental, have been performed [3-6]. Photonic insulators and materials with a photonic band gap may be the key to controlling and exploiting light. At a time when the electronics industry turns increasingly to optical devices for extra speed and capacity, this may turn out to be extremely important. Meanwhile, they are also interesting to many other fields of study, such as quantum physics, chemistry, etc.

In addition to this pure structural route to photonic materials, the concept of “negative epsilon” (or to say SP) can also be combined and exploited to make materials that have novel electromagnetic (EM) properties. Most recently, a Split Ring Resonator (SRR) composite designed to exhibit a magnetic resonance at THz frequencies was fabricated [7]. In this SRR device, the split ring structures have a self capacitance and self-inductance that create a resonance. The currents that flow when this resonance is activated couple strongly to an applied magnetic field, yielding an effective permeability that can reach quite high values. The size of the SRRs was on the order of 30 μm, 10 times smaller than the 300 μm wavelength at 1 THz. Scattering experiments confirmed that the SRR medium have a magnetic resonance that could be tuned throughout the THz band by slight changes to the geometrical SRR parameters. The THz SRR metamaterial illustrates the advantage of developing artificial magnetic response that is not available in naturally occurring materials.

Micro/nano structured materials may also have other interesting novel EM properties. In 1967, Soviet physicist V. G. Veselago proposed an innovative artificial medium for which both permittivity ε and permeability μ are negative [8], which he believed would result in negative refractive index and many other novel optical phenomena without violating any physical laws. It turned out by some of the recent researches that negative index of refraction could be achieved by either photonic crystal or metamaterials.

Cubukcu et al. [9] demonstrated negative refraction of electromagnetic waves in a two-dimensional dielectric photonic crystal that has a periodically modulated positive permittivity and a permeability of unity. Their structure consisted of a square array of alumina rods in air and exhibits the maximum angular range of negative refraction at an operating frequency of 13.7 GHz. Band diagram was calculated and they pointed out that equal frequency surfaces that are both convex and larger than those for air are needed to obtain negative refraction. They believe the negative-refraction effect depends only on the refractive index of the dielectric material and the geometric factors used in two-dimensional photonic crystals.

Parimi et al. [10] further demonstrated that negative index of refraction allows a flat slab of a material to behave as a lens, using the phenomenon of negative refraction in a photonic crystalline material. The key advance that enabled this observation lies in the design of a photonic crystal with suitable dispersion characteristics to achieve negative refraction over a wide range of angles. The focusing was observed only in a narrow frequency range, between 9.0 and 9.4 GHz, with the best focus at 9.3 GHz. Outside this narrow band, at all other frequencies between 2 and 12 GHz, a single focus point was not seen.

Shalaev et al. [11] reported negative refractive index in the optical range from a metamaterial consisted of double-periodic array of parallel gold nanorods pairs. Such behavior results from the plasmon resonance in the pairs of nanorods for both the electric and the magnetic components of light. The refractive index is retrieved from direct phase and amplitude measurements for transmission and reflection, which are all in excellent agreement with simulations. Both experiments and simulations demonstrate that a negative refractive index $n = -0.3$ was achievable at an optical communication wavelength of 1.5 μm using an array of nanorods.

5.2 Fabrication Techniques for Periodical Nanostructures

All the above mentioned theory and research at visible wavelengths place critical requirements on nanofabrication, as fabricating periodic nanostructures with such dimension scale and complexity with a high degree of control is very challenging. Traditional nanofabrication methods, such as Focus Ion Beam (FIB) and Electron Beam Lithography (EBL), are only capable of 2D patterning in a thin film. Although devices based on two dimensional nanostructures have demonstrated the theory, the practical applications of such 2D structures are limited by the finite thickness of the film, although demonstrated to some extent.

A direct solution to achieve 3D structure using existing technology is via a layer-by-layer approach [12]. Lin et al. [13] reported the construction of a three-dimensional infrared photonic crystal on a silicon wafer using relatively standard microelectronics fabrication technology. The 3D lattice structure was built by repetitive deposition and etching of multiple dielectric films. To accomplish this goal, a comprehensive five-level stacking process was developed. Within each layer, SiO_2 was first deposited, patterned, and etched to the desired depth. The resulting trenches were then filled with polycrystalline silicon and then flattened using chemical mechanical polishing (CMP). Such process was then repeated until five-level was completed. The wafer was immersed in a HF/water solution for the final removal of SiO_2. The pitch between adjacent rods is

4.2 μm, the rod width is 1.2 μm and the layer thickness is 1.6 μm. The crystal shows a large stop band (10–14.5μm), strong attenuation of light within this band (12 dB per unit cell) and a spectral response uniformity to be better than 1 percent over the area of a 6-inch wafer.

Qi et al. [14] presented the fabrication process of 3D photonic crystals using a layer-by-layer approach employing E-beam lithography to align and define each layer. Spin-on-dielectric (SOD) was used to fill and planarize the etched cylinders. Point-defect micro-cavities were introduced during the fabrication process and optical measurements show they have resonant signatures around telecommunications wavelengths (1.3–1.5 μm). Measurements of reflectance and transmittance at near-infrared were in good agreement with numerical simulations.

The general drawbacks for the layer-by-layer approach are the extremely complex alignment and planarization processes between layers. Other novel 3D nanofabrication techniques based on new concepts and physics have been proposed.

Blanco et al. [15] fabricated single crystals of silicon inverse opal with a complete three-dimensional photonic bandgap centered at 1.46μm. The material synthesis process was performed in a suspension of mono-dispersed silica particles (500 nm diameter) that act as seeds for further growth. Once the large spheres (600-1000 nm) are made, they are settled in an aqueous solution of ethylene glycol (typically 50% concentration). The resulting opal is a close-packed f.c.c. lattice of silica spheres with a typical single domain size of 100 μm. A further sintering process leads to the formation of small necks between the silica spheres and provides the template with mechanical stability. Silicon is then grown inside the voids of the opal template by means of chemical vapor deposition (CVD) using disilane (Si_2H_6) gas. After silicon growth, the samples are heated to 600 Celsius to improve the semiconductor crystallization and to allow diffusion of silicon inside the void structure. The silica template is subsequently removed using a Fluoride-based etching procedure. The synthesis method is simple and inexpensive, yielding photonic crystals of pure silicon that are easily integrated with existing silicon-based microelectronics.

Campbell et al. [16] generated periodic microstructure by interference of four non-coplanar laser beams in a film of photoresist typically 30 μm thick. The four laser beams are generated by splitting the ultraviolet laser output twice with dielectric beam splitters. The three outer beams are symmetrically placed around the central beam with an angle of 39 degree. The intensity distribution in the interference pattern has three dimensional translational symmetry; its primitive reciprocal lattice vectors are equal to the differences between the wave vectors of the beams. Films of photoresist are spun onto fused silica disks, and the fused silica substrate is index-matched to a thick glass block with hydrocarbon oil to reduce the effects of back-reflected laser light. Highly exposed photoresist is rendered insoluble; unexposed areas are dissolved away to reveal a three dimensionally periodic structure formed of cross-linked polymer with air-filled voids. To demonstrate that the microstructure has adequate connectivity to act as a template for a crystal with higher refractive-index contrast, an inverse replica in titania was produced by filling the pores with titanium (IV) ethoxide, and then heating to 575 degree Celsius in moist air to burn off the template and sinter the ceramic.

Direct laser writing (DLW) by multi-photon polymerization [17] of a photoresist has emerged as a technique for the rapid, cheap and flexible fabrication of nanostructures for photonics. Deubel et al. [18] fabricated high quality large-scale Face-Center-Cubic (FCC) layer-by-layer structures by DLW. Optical characterization of the structures revealed fundamental stop bands ranging from 1.3 to 1.7 μm. In DLW by multi-photon polymerization, a photoresist is illuminated by laser light at a frequency below the single-photon polymerization threshold of the resist. When this laser light is tightly focused inside the photoresist, the light intensity inside a small volume (the focus) may exceed the threshold for initiating multi-photon polymerization. The size and shape of these so-called ‘voxels’ depend on the iso-intensity surfaces of the microscope objective, and the exposure threshold for multi-photon processes of the photosensitive medium.

Most recently, a novel 3D nano-fabrication method was developed by J. Rogers’ group [19]. In their approach, high-resolution, conformable phase masks were used to fabricate 3D nanostructures by photolithography. Light passing through a phase mask that has features of relief comparable in dimension to the wavelength generated a 3D distribution of intensity that exposes a photopolymer film throughout its thickness. Rigorous coupled wave analysis was utilized to reveal the fundamental aspects of the optics associated with this method.

We believe that it will be vital to have a 3D nanofabrication method that possesses the following capabilities: 1) to fabricate 3D structures in a parallel fashion to avoid complex processes, 2) to introduce local defects for desired functionalities, 3) to selectively layout the nanostructures with a microscale outer dimension for device development.

5.3 SURFACE PLASMON ASSISTED THREE-DIMENSIONAL NANOLITHOGRAPHY

5.3.1 FDTD Modeling Results

Surface Plasmons (SPs) are collections of electrons that oscillate at an interface between a metal and a dielectric material [20-21]. In 1998, Ebbesen et al. [22] discovered extraordinary optical transmission of light through perforated metal film and concluded that such phenomena were due to SPs generated on the metal film and coupled with light. Since then, SPs have invoked immense research interest. SPs cannot be directly generated by light on smooth metal surfaces because of momentum mismatch [20]; however, it has been shown that periodic nanostructures, like hole or aperture arrays, on metal films provide momentum compensation, which allows light-SP conversion and manipulation of light at sub-wavelength scales [20]. In fact, this phenomenon has been used to overcome the diffraction limit of traditional photolithography [23-25].

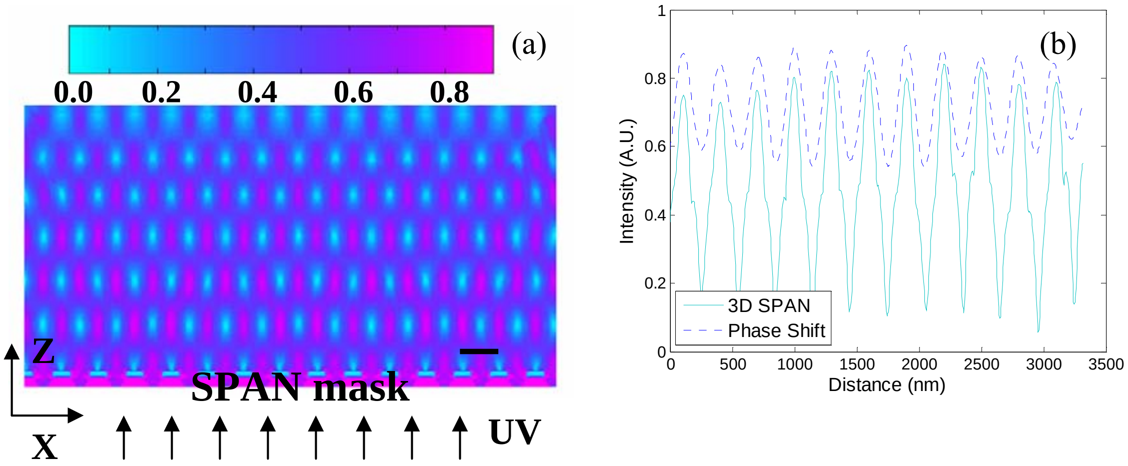

Figure 5-1: (a) Optical field intensity distribution in the photoresist after a 3D-SPAN mask with 1D grating. The wavelength of light is 365 nm. Scale bar = 300nm. (b) Comparison of contrast achieved using aluminum mask and optimized phase shift mask.

We have found that when apertures are positioned at resonant periodicities, incident light generates a strong near-field interference pattern on the opposite side of the apertures. Figure 5-1 shows a TM mode (with magnetic field H perpendicular to the simulation domain) distribution of optical intensity calculated by the Finite Difference Time Domain (FDTD) method. It is very interesting to see that the interference pattern in the medium (refractive index n = 1.67) forms a very regular virtual lattice structure with very strong intensity contrast at a very fine scale. The contrast of such interference is very large with minimum at almost zero while maximum at about 0.9, with 1 being the incident light amplitude. Such interference phenomenon may be related to the Wood-Rayleigh anomaly associated with the horizontal mode of SPs [26], which is highly dependent on the grating period and the angle of incidence. In our study, we chose aluminum as the mask material because it most strongly supports SPs at ultraviolet (UV) frequencies [21]. The aperture width and periodicity in Fig. 5-1 is 150 nm and 300 nm, respectively.

Although such optical near-field interference looks similar to the ordinary diffraction grating near-field due to optical path difference, we believe the SPs have played an important role in our 3D-SPAN. To illustrate this point, we did simulation of the optical near-field using phase shift mask [19] with same periodicity but varied thickness. Although the optical field patterns in the two cases are alike, the contrast is different. In Fig 5-1(b), we compare the contrast of the optical field by Aluminum mask and optimized phase shift mask. It is clear from the plot that 3D-SPAN can achieve a much larger contrast, which can significantly facilitate the photolithography process. It is understandable that phase shift mask produces a relatively small contrast, as the materials used in the mask are all transparent; while in our case the metallic material can effectively block the undesired background light. Nevertheless, we feel the detail mechanism of SPs in achieving such high contrast interference is worth further investigation.

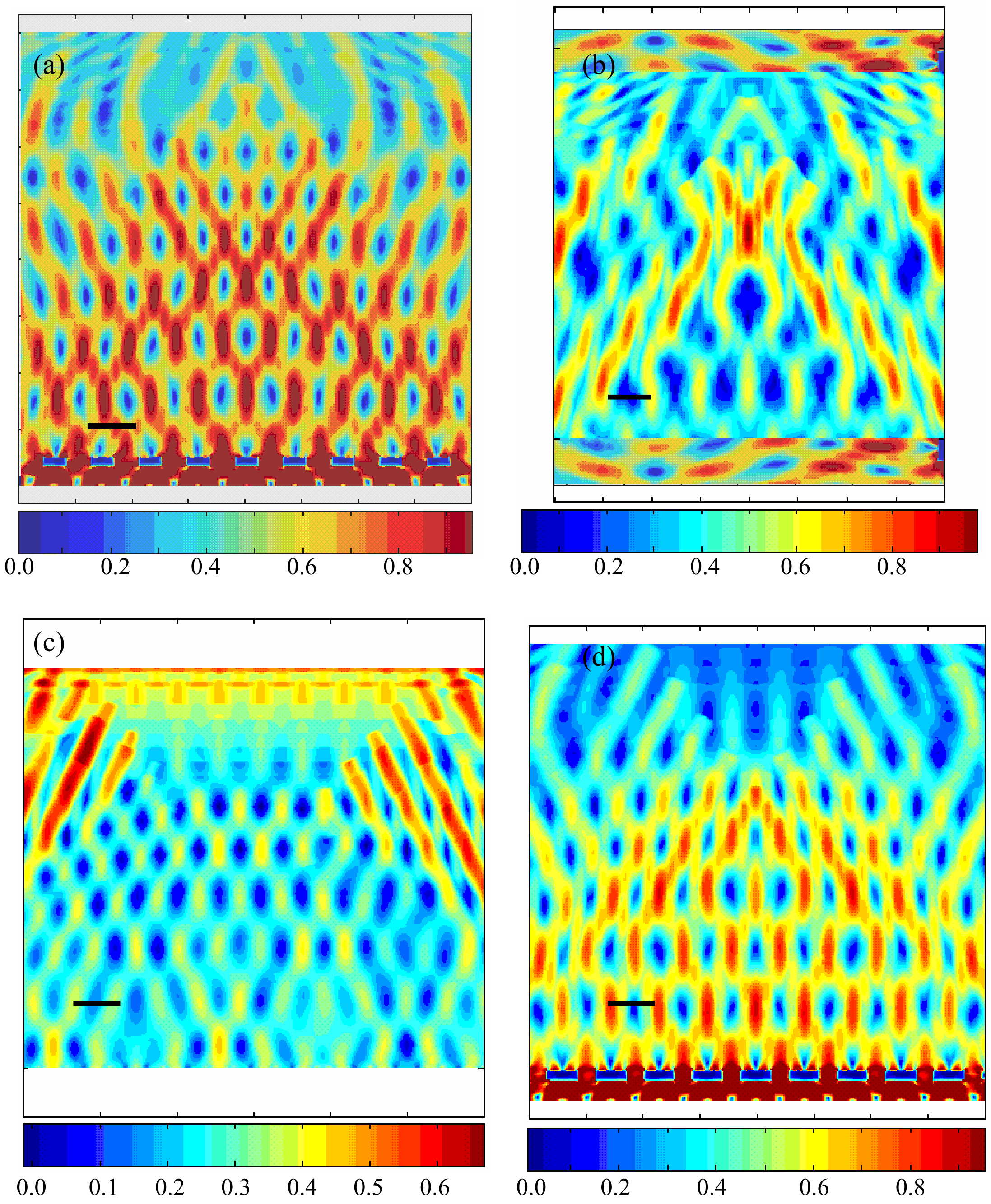

Figure 5-2: Effect of different parameters on the interference pattern and contrast. a) Al mask, period a = 300 nm, aperture width d = 150 nm; b) Al mask, a = 350 nm, d = 150

nm; c) Ag mask, a = 300 nm, d = 150 nm; d) Al mask, a = 300 nm, d = 100 nm. Scale bars = 300 nm.

Figure 5-2 shows the FDTD study of the effect of different parameters on the contrast of the near-field interference. From the simulation results it is clear that the interference pattern is sensitive to the periodicity of the grating mask and the material properties of the mask. However the tolerance of grating period is acceptable and is within the resolution of FIB lithography, making it feasible for experimental demonstration. The number of the pattern layers is dependent upon the combination of the grating mask and the resist thickness, as shown in figure 5-3. When the thickness of the photoresist and the number of the apertures are both large, the number of interference layers also increase, as compared to figure 5-2(A).

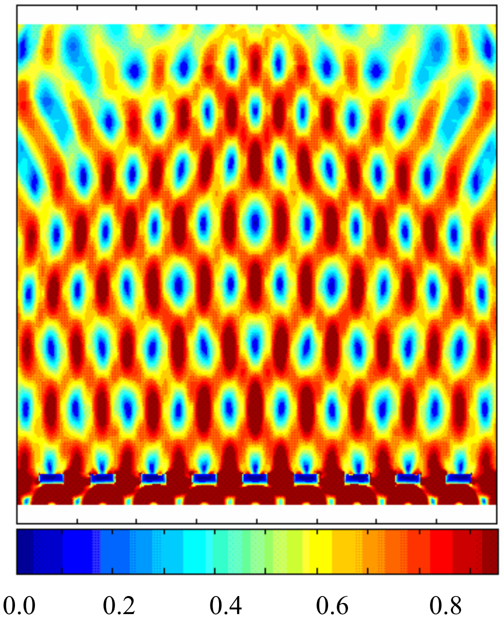

Figure 5-3: More than 8 layers of interference patterns can be seen in FDTD modeling when both the number of grating apertures and thickness of resist are large.

5.3.2 Experimental Demonstration

SU-8 (MicroChem®), a negative tone chemically amplified photoresist, is used to transfer the optical interference pattern to polymer structure. SU-8 has been widely employed in sub-micron scale lithography methods, such as holographic lithography [16] and DLW [18]. SU-8 was chosen in these studies for the following reasons: 1) SU-8 is crosslinked by acid-catalyzed photopolymerization, capable of sub-50 nm resolution patterning; 2) SU-8 has a refractive index of 1.67, relatively high and suitable for applications where contrast of refractive index is needed; 3) monomers in SU-8 do not directly polymerize during light exposure, resulting in no significant change in refractive index and optical field distribution; 4) SU-8 monomers have eight epoxy groups, capable of forming very dense crosslinked networks and bestowing high solubility contrast during the development process. These merits make SU-8 the best choice in the 3D-SPAN process.

In our experiments, we first deposited a 50-nm-thick aluminum layer on a quartz substrate by e-beam evaporation. Focused ion beam (FIB) was then used to pattern the aluminum layer. The aluminum mask patterns include the 1D grating structures, as previously explained and shown in figure 5-1. After FIB patterning, SU-8 photoresist was spin-coated onto the aluminum mask to a thickness of 3 μm. A thin layer of OmniCoat (MicroChem ®) was applied between the resist and the mask to improve adhesion. The photoresist was then exposed to UV light for three minutes through the mask using a UV aligner (HTG, 365nm). After exposure, the samples were developed in SU-8 developer for an hour and then gently air-dried. Figure 5-4(a) shows the resulting structure viewed at a 52-degree angle relative to the surface normal. FIB milling offered the accessibility to the cross-section of the 2D structure, and is shown in the SEM picture at the same 52-degree angle in figure 5-4(b). Seven layers of holes are shown in the SEM pictures. The first layer of holes relative to the bottom of the structure did not resolve very well due to the layer of OmniCoat, while the top 3 layers were partially blocked by the materials re-deposited during FIB milling. Because of the shrinkage of the SU-8 polymer, the holes are rather square instead of being elliptical, with a size of about 150 nm, and form a triangular lattice structure by self-adjustment.

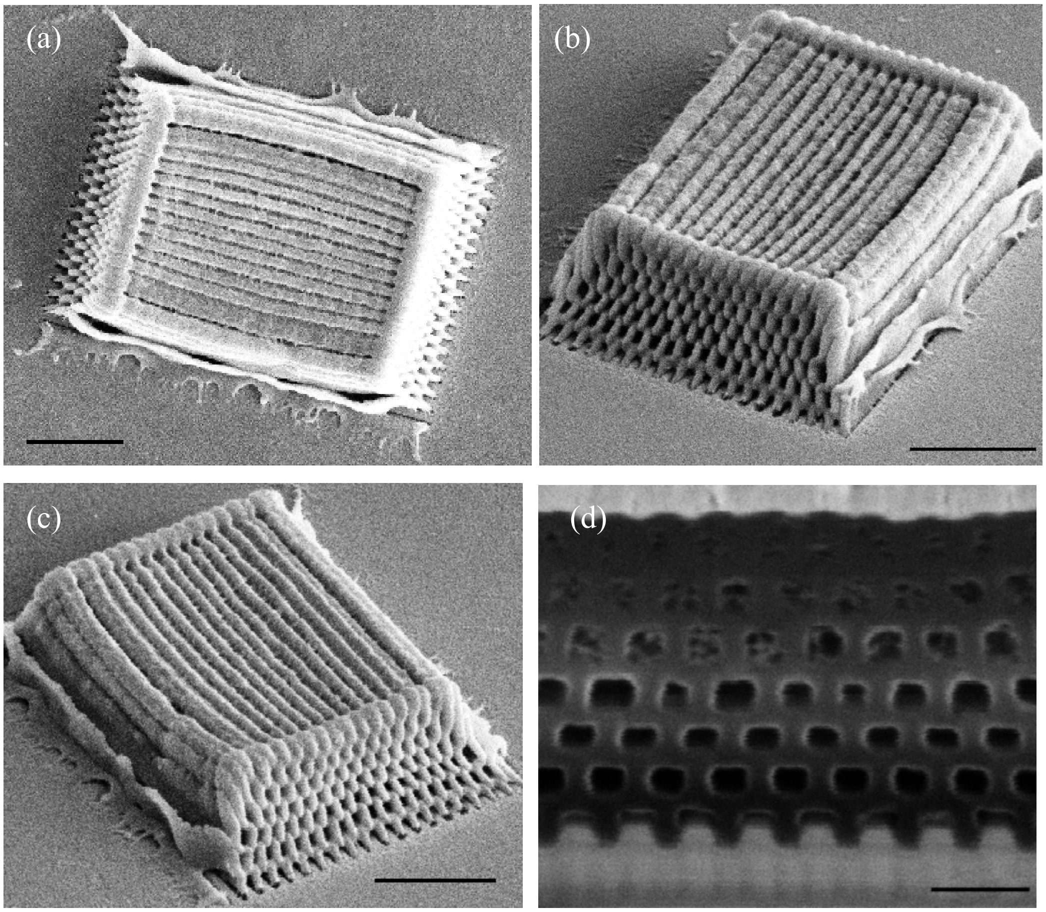

Figure 5-4: Structures fabricated by 3D-SPAN using 1D grating mask. (a-c) SEM image of the structure by 1D SPAN mask (Fig 5-8a). Scale bar = 2 μm. (d) Cross-section view of the structure. Scale bar = 500nm. (Note: Figure b, c and d are viewed at 52 degree from the normal of the sample surface)

The thickness of the polymer structure (the number of layers) is dependent upon several factors, among which the thickness of the photoresist and the number of grating apertures are the most important. In our experiments, a maximum of seven or eight layers was generated with 30 apertures and a 3-micron-thick photoresist. If thicker photoresist was used, the additional layer would tend to merge due to the decrease in intensity contrast because of both diffraction and scattering in the photoresist. By optimizing the process parameters and materials used, more layers could be fabricated.

One of the direct applications of 3D-SPAN could be the fabrication of photonic crystal structures. The lattice constants of the 2D structures are about 300 nm, as shown in figure 5-4, which implies that the structures may have a band gap in the visible/IR range. Fig. 5-5 shows the band structures calculated by a plane wave expansion technique [27] based on the geometry shown in Fig 5-4(b). The results show that band-gap exists for both TE and TM modes for the 2D structure shown in figure 5-4.

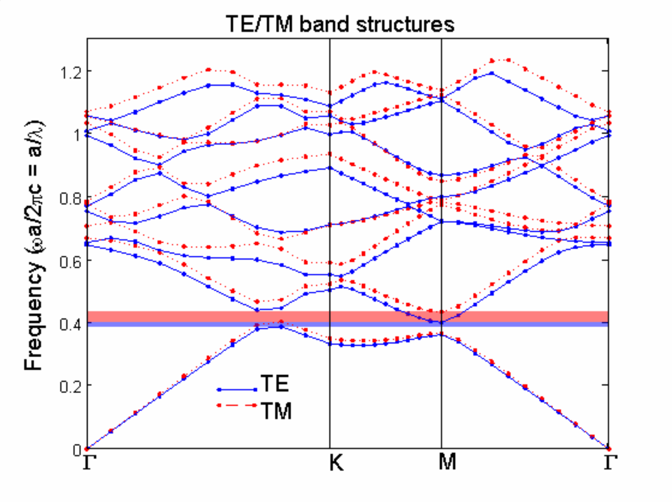

Figure 5-5: TE and TM mode band diagram of the 2D structure in Fig 5-4(d) calculated by plane wave expansion technique.

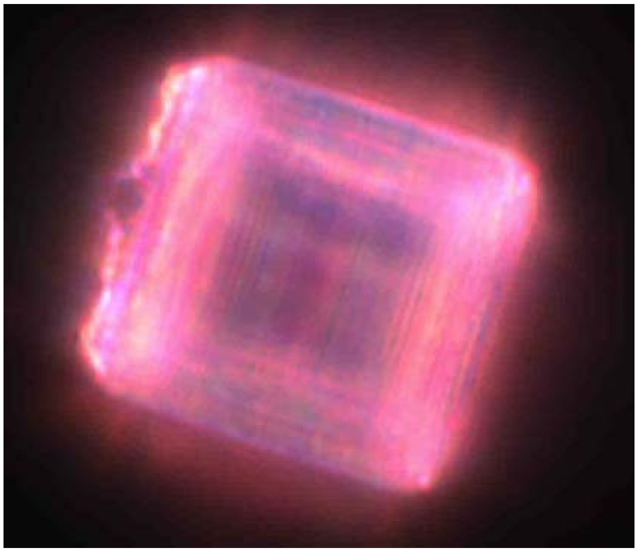

Figure 5-6: Dark field optical image of the 2D structure at the reflection mode. The sample has a size of about 4 μm.

In fact, the 2D structures exhibit interesting colors under a microscope, which can be observed with bare eyes. Only after development was completed did the samples exhibit such colors, which were used to determine if the development time in SU-8 developer was enough. Apparently the structures with different qualities have different colors and according to my experience the structures with best quality (close to seen in figure 5-4) have a color close to mauve (or pink). Figure 5-6 shows the optical images of the 2D structure under a microscope at reflection or transmission mode captured by a charge coupled device (CCD) camera. However it is believed that the CCD camera can introduce certain amount of artificial wavelength shift effect. Since the presence of the metallic mask underneath the structure, the exact contribution from the mask to the color we observed is unknown. However, using the same microscope and CCD camera, the images of a bare grating mask or a mask coated with a photoresist layer of the same thickness before photolithography were not able to show such interesting colors. Due to the unavailability of spectrum analyzer at visible range with the capability to handle a micro-size sample, the optical spectrum characterization of our 2D structure was not conducted.

The side-view of the 2D structure in figure 5-4 matches fairly well with our FDTD simulation (Fig. 5-1). However, interestingly, our lithography is done using UV light from a mercury lamp, while in the FDTD simulation the light source is assumed to be monochromatic, polarized, and coherent. The discrepancies can be explained by the following reasons. First, the ultraviolet light from the mercury lamp has a spectrum with the maximum peak centred at 365 nm with a full width at half maximum (FWHM) of about 20 nm. The optical properties of the materials used in 3D-SPAN, especially the aluminium mask (table 4-1), do not vary significantly across this UV spectrum [28]. Thus the optical fields responding to each incoming wavelength are similar. As a result, the use of a multi-chromatic UV light does not significantly alter the 3D-SPAN results from what we predict by FDTD simulation. Secondly, the un-polarized light source can be thought of as the superposition of its TM and TE components. It was found that the transmission through sub-wavelength metallic apertures at TE mode is prohibited due to the absence of SP involvement [22]; thus, the contribution from the TE mode component of UV light is either trivial or over-shadowed by the TM mode counterpart. Finally, although the light source is incoherent, the photons are not emitted at exactly the same time. For each photon, the electrons on the aluminum mask 'see' a coherent incoming EM field and cope with it accordingly. This is somewhat similar to the classical two-slit interference effect concerning white light. However without effects from SPs, transmission through the sub-wavelength apertures would be too low and near-field interference patterns would not be generated.

The use of UV light rather than polarized coherent light offers advantages in terms of design flexibility. Although the pattern can only be generated with TM mode light, the unpolarized light can provide the TM component no matter how the mask pattern is oriented. What's more, the mask pattern can even be rotated and superimposed. For example, by bending the SPAN mask pattern, the structure patterned in the photoresist will bend the same way, as shown in figure 5-7. On the other hand, a cross-mask pattern, which is the superposition of two sets of 1D gratings (1 μm periodicity) that are perpendicular to each other, can be used to produce 3D structures (Fig 5-8a). Such 1D grating cannot produce linked structures by itself; however, the combination of them can form elegant 3D networks. By using a thinner photoresist layer, the cross-section in the z-plane can be revealed, as shown in Fig 5-8(b).

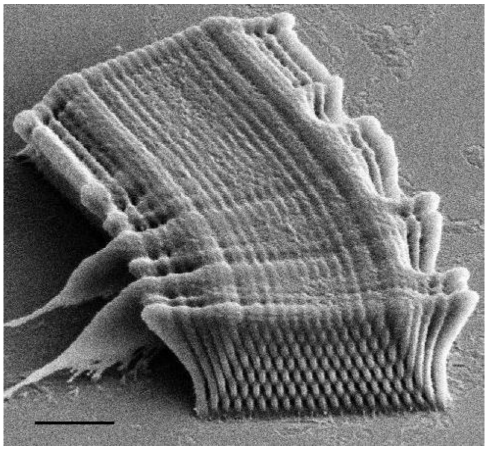

Figure 5-7: SEM pictures of a curved 2D structure fabricated using a curved 1D SPAN mask (Fig 5-9b, 5-9c). Scale bar = 2μm.

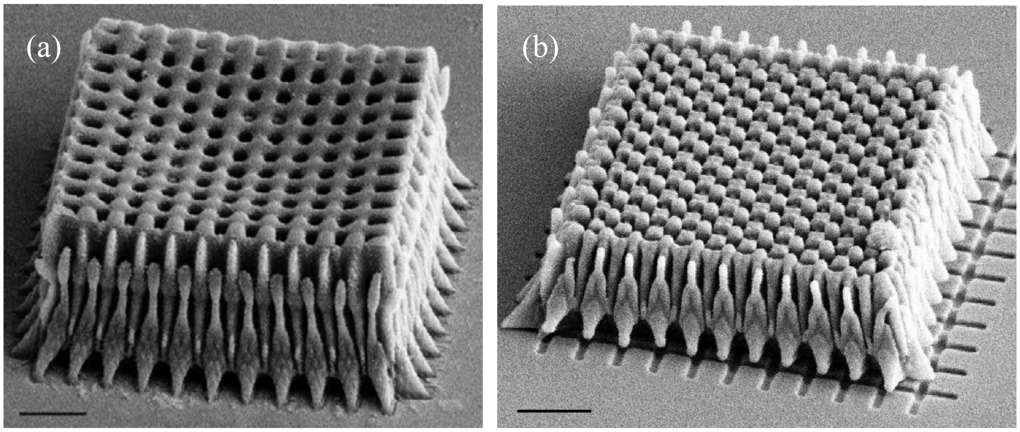

Figure 5-8: SEM pictures of 3D structures fabricated using 2D SPAN mask (Fig 5-9d). Scale bar = 2μm.

The SEM images of the SPAN masks fabricated by FIB are illustrated in figure 5-9. The qualities of the mask pattern, namely the dimension of the apertures as well as the gratings and the sharpness and cleanness of the apertures, are the important factors in determining the quality of final multilayer nanostructure.

Defects intentionally fabricated in periodic structures have been studied with great interest [14]. In fact, 3D-SPAN can easily introduce defects into the 3D nanostructures because of its intrinsic near-field approach. Figure 5-10 shows the nanostructures fabricated with 3D-SPAN masks having one or two missing apertures. We also include in the figure our FDTD modelling predictions. Considering the fact that unfastened structures will be washed away during develop, we feel the simulation is very successful in guiding our experiments. Although line and point defects may not be precisely controlled by 3D-SPAN, defects can be engineered and optimized to some extent by designing them in the SPAN mask.

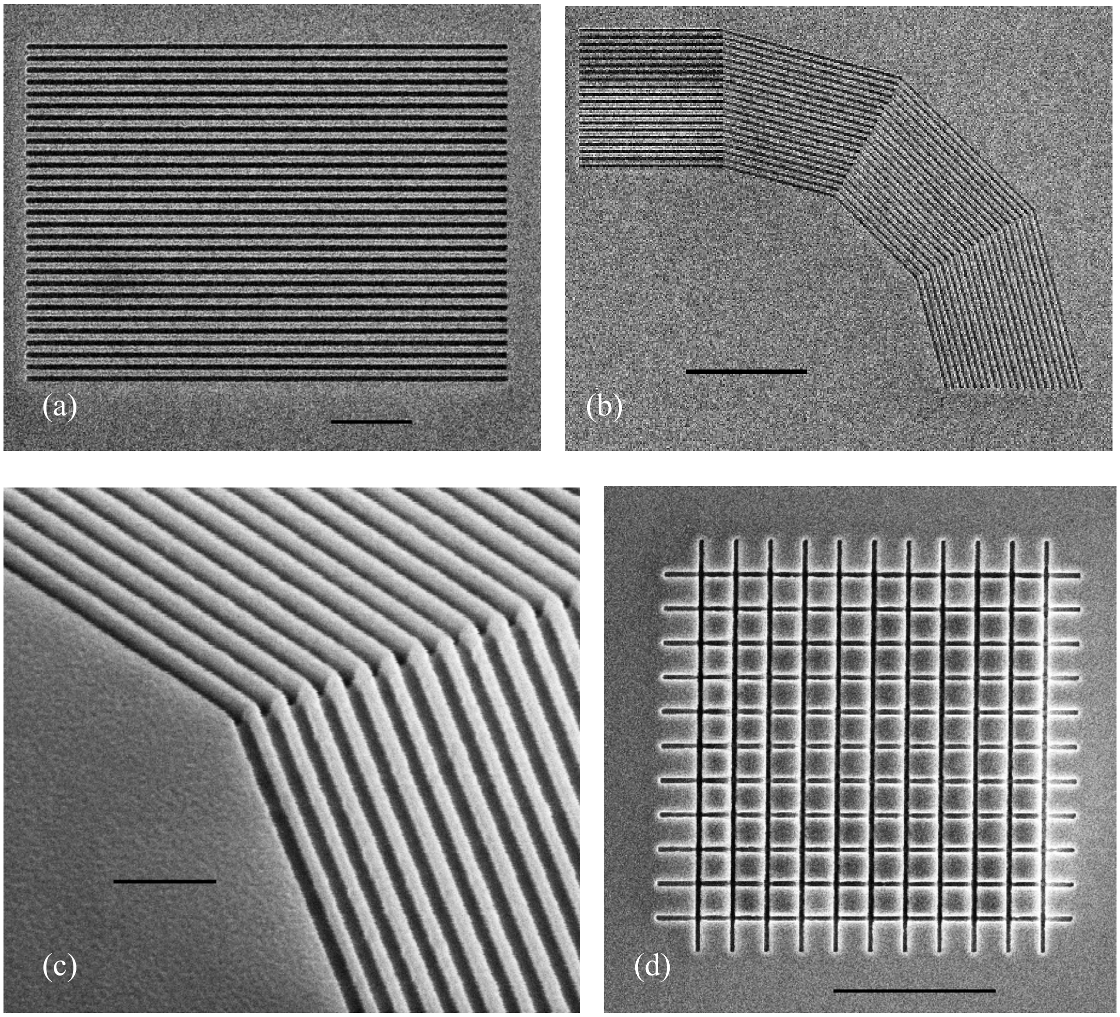

Figure 5-9: 3D-SPAN mask patterns. Scale bars: 2μm, 5μm, 1μm, 5μm for (a), (b), (c), (d) respectively.

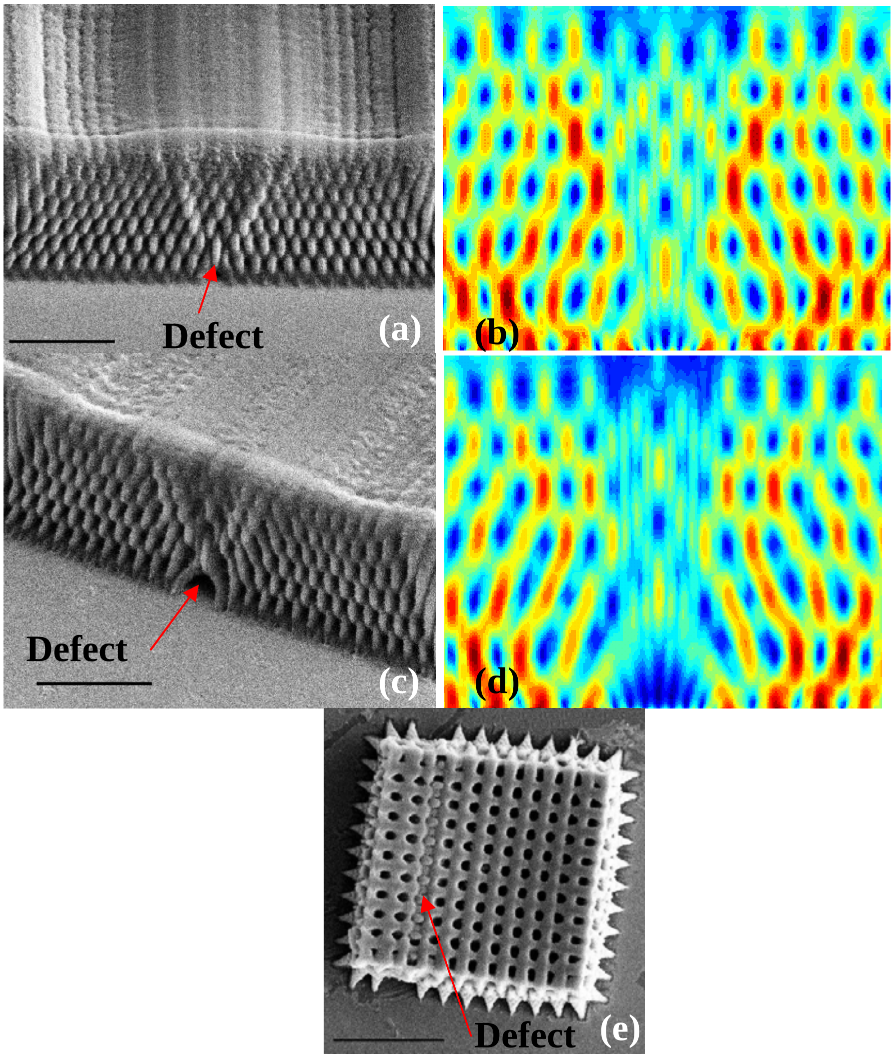

Figure 5-10: Different defects designed locally in the nanostructures. (a) A 2D structure fabricated using a SPAN mask with one aperture missing. Scale bar = 2μm. (b) FDTD simulation of corresponding condition in (a). (c) A 2D structure fabricated using a SPAN mask with two aperture missing. Scale bar = 2μm. (d) FDTD simulation of corresponding condition in (c). (e) A 3D structure fabricated using a SPAN mask with one aperture missing. Scale bar = 5μm.

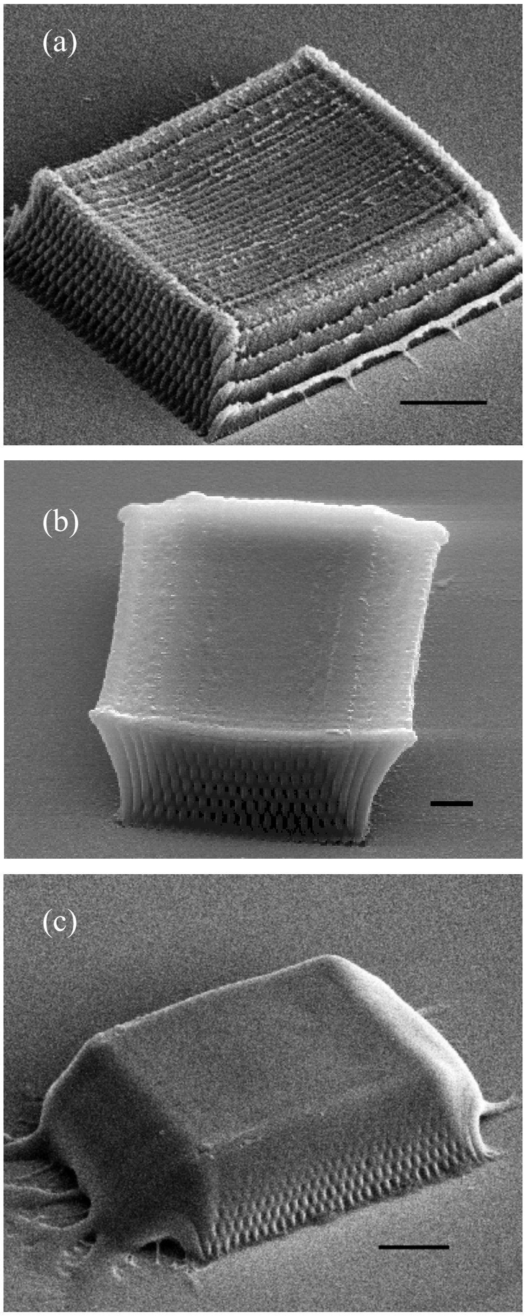

Figure 5-11: Unsuccessful structures fabricated by 3D-SPAN due to bad process parameters. Scale bars: a) 2 μm, b) 1μm, c) 2μm.

5.3.3 Discussion

Among the many process parameters during the experiments, the UV exposure time and development time are the most important ones. For example, when the UV dose were not enough, the structure tended to shrink and be concave in the center, as shown in figure 5-11(a). If UV dose was further reduced, the structure became very weak and easily destroyed in following processes. On the other hand, if the UV exposure was over-dosed, the structure would have unwanted feature on the sides, as could be seen in figure 5-11(b). The development time was also critical. If the time was not enough, the structure seemed to be covered with a layer of polymer, as shown in figure 5-11(c). If over-developed, the structure may simply be washed away due to the adhesion problem, even with the adhesion promoter.

The post exposure bake (PEB) is not implemented in the 3D-SPAN process. PEB is often used either to minimize the standing wave effect [29] or to drive the acid-catalyzed photoreaction for increased photosensitivity. For DLW [18], the two-photon reaction rate is low so PEB must be employed. However, the elevated temperatures cause the photo-product to diffuse and the polymer lines start merging when the distance between them is approximately a half micron [18]. The 3D-SPAN technique harnesses the high density high contrast interference patterns generated by SPs. As seen in our simulation, the light intensity can depreciate from 1 (incident light intensity) to zero within a distance of about 150 nm. Such an intrinsically high contrast facilitates the 3D-SPAN process. Thus PEB is not just unnecessary, but rather destructive.

Our lithography approach resembles four-beam holographic lithography [16] in that optical interference patterns are combined with photolithography technique to produce periodic nanostructures. However, holographic lithography creates interference by maintaining phase differences among the four beams by optical path differences, while in our case the interference pattern is created by an aluminum mask through which SP-light coupling occurs. The optical path difference control can only be achieved by a coherent light source with good directivity, which excludes the use of light from a UV lamp. In addition, the 3D-SPAN process utilizes near-field interference rather than far-field interference. While the far-field interference is more suitable for large scale patterning of periodic structures, our approach is ideal for its nano- and micro-scale patterning capabilities. The outer dimension of the structures that we have shown can be produced as small as a few microns in size, which we believe can not be achieved with equivalent quality, especially at the boundaries, by simply combining the four beam holographic lithography with a shadow mask due to the near-field effect. Furthermore, by designing the mask layout, the 3D-SPAN technique can easily pattern nanostructures with complex outer geometry and opens possibility of fabricating integrated nano-photonic circuits, analogous to the microelectronic circuits patterned by photolithography. Moreover, 3D SPAN can easily engineer defects to some extent, which is impossible for 4 beam holographic lithography.

The 3D-SPAN process is completely compatible with microelectronics fabrication processes. We believe the principle of our technology can be extended to pattern photoresist film on a substrate and to pattern 3D nanostructures with outer dimension much larger and more complex provided that appropriate mask pattern with desired dimension and quality is available. The 3D-SPAN technology can then easily allow one to replicate the 3D structures by re-using the mask. We envision our technique being used as a processing step in fabrication to manufacture components in photonics and optoelectronics. These structures can either be directly used or used as a template [15-16, 18] to meet the fabrication needs in nanophotonics.

SUMMARY

In this chapter, optical near-field interference patterns enhanced by SP-light coupling via different metallic grating mask were combined with photolithography technique to generate different 2D/3D nanostructures. The 2D structure has a lattice constant of about 300 nm, and the structure is an untraditional out-of-plane multilayer structure that can not be achieved easily by traditional nanofabrication methods. The 3D structure has a periodicity on the order of 1 μm. All the structures were fabricated in a single lithography step. We believe other 2D/3D structures can be fabricated by exploring the 2D mask patterns and the principle of our approach can be extended to pattern photoresist film on a substrate. We have also preliminarily demonstrated that by designing our SPAN mask pattern, periodic 3D nanostructures with arbitrary outer geometry and controllable defects can be easily fabricated. 3D-SPAN can be either used as a processing step to fabricate components in photonics, or be used to generate a template to meet the fabrication needs in the nanophotonics.

Reference

1. E. Yablonovitch, "Inhibited Spontaneous Emission in Solid-State Physics and Electronics," *Physical Review Letters*, **58**, pp.2059-2062 (1987).
2. S. John, "Strong Localization of Photons in Certain Disordered Dielectric Superlattices," *Physical Review Letters*, **58**, pp.2486-2489 (1987).
3. S. Y. Lin, E. Chow, V. Hietala, P. R. Villeneuve, J. D. Joannopoulos, "Experimental demonstration of guiding and bending of electromagnetic waves in a photonic crystal," *Science*, **282**, pp.274-276 (1998).
4. J. S. Foresi *et al.*, "Photonic-bandgap microcavities in optical waveguides," *Nature*, **390**, pp.143-145 (1997).

5. S. H. Fan, P. R. Villeneuve, J. D. Joannopoulos, E. F. Schubert, "High extraction efficiency of spontaneous emission from slabs of photonic crystals," *Physical Review Letters*, **78**, pp.3294-3297 (1997).
6. S. John, J. Wang, "Quantum Optics of Localized Light in a Photonic Band-Gap," *Physical Review B*, **43**, pp.12772-12789 (1991).
7. T. J. Yen *et al.*, "Terahertz magnetic response from artificial materials," *Science*, **303**, pp.1494-1496 (2004).
8. V. G. Veselago, "The electrodynamics of substances with simultaneously negative values of eps and mu," *Soviet Physics Uspekhi*, **10**, 509 (1968).
9. E. Cubukcu, K. Aydin, E. Ozbay, S. Foteinopoulou, C. M. Soukoulis, "Negative refraction by photonic crystals," *Nature*, **423**, pp.604-605 (2003).
10. P. V. Parimi, W. T. T. Lu, P. Vodo, S. Sridhar, "Photonic crystals - Imaging by flat lens using negative refraction," *Nature*, **426**, pp.404-404 (2003).
11. V. M. Shalaev *et al.*, "Negative index of refraction in optical metamaterials," *Optics Letters*, **30**, pp.3356-3358 (2005).
12. K. M. Ho, C. T. Chan, C. M. Soukoulis, R. Biswas, M. Sigalas, "Photonic Band-Gaps in 3-Dimensions - New Layer-by-Layer Periodic Structures," *Solid State Communications*, **89**, pp.413-416 (1994).
13. S. Y. Lin *et al.*, "A three-dimensional photonic crystal operating at infrared wavelengths," *Nature*, **394**, pp.251-253 (1998).
14. M. H. Qi *et al.*, "A three-dimensional optical photonic crystal with designed point defects," *Nature*, **429**, pp.538-542 (2004).
15. A. Blanco *et al.*, "Large-scale synthesis of a silicon photonic crystal with a complete three-dimensional bandgap near 1.5 micrometres," *Nature*, **405**, pp.437-440 (2000).

16. M. Campbell, D. N. Sharp, M. T. Harrison, R. G. Denning, A. J. Turberfield, "Fabrication of photonic crystals for the visible spectrum by holographic lithography," *Nature*, **404**, pp.53-56 (2000).
17. S. Kawata, H. B. Sun, T. Tanaka, K. Takada, "Finer features for functional microdevices - Micromachines can be created with higher resolution using two-photon absorption.," *Nature*, **412**, pp.697-698 (2001).
18. M. Deubel *et al.*, "Direct laser writing of three-dimensional photonic-crystal templates for telecommunications," *Nature Materials*, **3**, pp.444-447 (2004).
19. S. Jeon *et al.*, "Fabricating complex three-dimensional nanostructures with high-resolution conformable phase masks," *Proceedings of the National Academy of Sciences of the United States of America*, **101**, pp.12428-12433 (2004).
20. W. L. Barnes, A. Dereux, T. W. Ebbesen, "Surface plasmon subwavelength optics," *Nature*, **424**, pp.824-830 (2003).
21. H. Raether, *Surface plasmons on smooth and rough surfaces and on gratings*, Springer tracts in modern physics; 111. (Springer-Verlag, Berlin ; New York, 1988).
22. T. W. Ebbesen, H. J. Lezec, H. F. Ghaemi, T. Thio, P. A. Wolff, "Extraordinary optical transmission through sub-wavelength hole arrays," *Nature*, **391**, pp.667-669 (1998).
23. X. G. Luo, T. Ishihara, "Surface plasmon resonant interference nanolithography technique," *Applied Physics Letters*, **84**, pp.4780-4782 (2004).
24. W. Srituravanich, N. Fang, C. Sun, Q. Luo, X. Zhang, "Plasmonic nanolithography," *Nano Letters*, **4**, pp.1085-1088 (2004).
25. D. B. Shao, S. C. Chen, "Surface-plasmon-assisted nanoscale photolithography by polarized light," *Applied Physics Letters*, **86**, pp. 253107 (2005).

26. S. Collin, F. Pardo, R. Teissier, J. L. Pelouard, "Horizontal and vertical surface resonances in transmission metallic gratings," *Journal of Optics a-Pure and Applied Optics*, **4**, pp.S154-S160 (2002).
27. H. S. Sozuer, J. W. Haus, R. Inguva, "Photonic Bands - Convergence Problems with the Plane-Wave Method," *Physical Review B*, **45**, pp.13962-13972 (1992).
28. E. D. Palik, *Handbook of optical constants of solids*, Academic Press handbook series. (Academic Press, Orlando, 1985).
29. M. J. Madou, *Fundamentals of microfabrication : the science of miniaturization* (CRC Press, Boca Raton, Fla., ed. 2nd, 2002).

Chapter 6: Conclusion

This dissertation includes both extensive numerical modeling work and three topics of study of nanoscale patterning/fabrication techniques utilizing optical near-field.

The FDTD method to study EM phenomena was first investigated and a 2D TM mode numerical modeling code based on this method was built to investigate the light interaction with sub-wavelength scale structures. The modeling code, although simplified, addresses the basic issues associated with the FDTD method, such as boundary condition, plane wave formation and metallic material handling. The model was benchmarked and used later as a tool for this dissertation study.

A direct surface nanopatterning technique called 'near-field-enhanced mold-assisted direct patterning' was investigated. Optical near-field enhancement around the nanostructures, for example nano tips, was utilized to locally ablate a thin metallic layer on a substrate. I studied and proposed a scheme in which the whole patterning area was under illumination and parallel patterning can be achieved utilizing such phenomena. Efforts were devoted to develop fabrication procedures of a nano ridge structure using standard semiconductor fabrication techniques. The near-field around such nano ridge was utilized to directly pattern lines in a single laser shot without the need to scan a nano tip. The resulting lines and dots pattern have a width or size ranging from 200 nm to 100 nm with depth on the order of 20 nm. The near-field enhancement factors were studied and optimized by numerical modeling and demonstrated in experiments. Smaller features size and better quality can be achieved.

Sub-wavelength scale light confinement by utilizing SP-light coupling was studied and achieved. The finding was applied in nanolithography. The patterning resolution was demonstrated to be able to extend to a sub-wavelength scale by exciting surface plasmons simultaneously on both a metallic mask and a substrate. Nanoscale one-to-one pattern transfer has been achieved in this Surface Plasmon Assisted Nanolithography (SPAN) without any additional equipment or added complexity to mask design. Both polarized laser beam of 355 nm wavelength and UV light source were used as light source to photoinitiate an 80 nm thick photoresist on a silicon substrate coated with a thin titanium layer of 80 nm thickness. Simulation results by finite difference time domain method have predicted the results and also revealed the contribution of surface plasmons excited on both the metallic mask and the Ti shield in helping to spatially confine the light. The lithography scheme discussed in this chapter offers a convenient, low cost, and massive pattern transfer method for nanofabrication needs. The feature size using such method could be further scaled down, limited theoretically by the validity of the dielectric function of the material, and practically by the fabrication of the mask.

The SPAN technique was extended to multi-layer patterning, in which optical near-field interference patterns enhanced by SP-light coupling were combined with photolithography technique to generate different 2D/3D nanostructures. The 2D structure has a lattice constant of about 300 nm, and such a multilayer structure was achieved in a single fabrication step. The 3D structures fabricated using 3D-SPAN has a periodicity on the order of 1 μm, predefined by the 2D SPAN mask. We believe other 2D/3D structures can be fabricated by exploring different 2D mask patterns and the principle of 3D-SPAN can be extended to pattern photoresist film on a substrate. Also, we preliminarily demonstrated that periodic 3D nanostructures with arbitrary outer geometry and controllable defects can be incorporated by designing the SPAN mask patterns. 3D-SPAN can be either used as a processing step to fabricate components in photonics, or be used as a template to meet the fabrication needs in the nanophotonics.

Appendix

```
// FDTD solver, C++ code
// FDTD with Drude model, 2D TE mode
// PML implemented, Plane wave excited

#include "stdafx.h"
#include <math.h>
#include <stdio.h>
#include <stdlib.h>
#include <fstream.h>
#include <string.h>
#include <time.h>


#define C0 299792458.0
#define MU0 1.256637061435917295385057353311801153678867759 75e-6
#define EPS0 8.854187817620389850536563031710750260608370e-12
#define PI 3.14159265358979323846 26

#define nPML 12
#define PML_max 1e-7
#define PML_odr 2.
#define PML_itf 0.25

#define TTSC 8

#define MAX_char 50

struct ndv1 {
public:
        double v;
        double c2;
```

```
        ndv1& operator+=(double);
};

inline ndv1& ndv1::operator +=(double x) {
        v = v + c2*x;
        return *this;
}

struct ndv2 {
public:
        double v;
        double c1;
        double c2;

        ndv2& operator+=(double);
};

inline ndv2& ndv2::operator +=(double x) {
        v = c1*v + c2*x;
        return *this;
}

double FREQ, LAMBDA;
int nx, ny, opt1, opt2, opt3;
int MAX_N, OPT_FQ, CELLS_PER_WL;
double **hz, **Ae;
ndv1 **ex, **ey;
ndv2 **jx, **jy;
ndv2 **hzxF, **hzyF, **exF, **eyF;
ndv2 **hzxB, **hzyB, **exB, **eyB;
ndv2 **hzxL, **hzyL, **exL, **eyL;
ndv2 **hzxR, **hzyR, **exR, **eyR;
double dx, dt, CA;
```

```
int ntpd;
char *file1="mFDTDpara.txt", file2[20], name[50];



double **init_arrD(int n1, int n2, double v, char *name)
{
        int i, j;
        double **v1;

        if ((v1 = (double **)malloc((n1)*sizeof(double *))) == NULL)
        {
                printf("Cannot allocate memory for %s\n", name);
                exit(1);
        }
        else
        {
                for(i=0; i<n1; i++)
                        if ((v1[i] = (double *)malloc((n2)*sizeof(double))) == NULL)
                        {
                                printf("cannot allocate memory for %s\n", name);
                                exit(1);
                        }
                        else
                                for(j=0; j<n2; j++)
                                {
                                        v1[i][j] = v;
                                }
        }

        if(name[0] != 0)
                printf("    Memory allocated for %s\n", name);

        return(v1);
}
```

```
ndv1 **init_arrNDV1(int n1, int n2, double v, double c2, char *name)
{
        int i, j;
        ndv1 **v1;

        if ((v1 = (ndv1 **)malloc((n1)*sizeof(ndv1 *))) == NULL)
        {
                printf("Cannot allocate memory for %s\n", name);
                exit(1);
        }
        else
        {
                for(i=0; i<n1; i++)
                        if ((v1[i] = (ndv1 *)malloc((n2)*sizeof(ndv1))) == NULL)
                        {
                                printf("cannot allocate memory for %s\n", name);
                                exit(1);
                        }
                        else
                                for(j=0; j<n2; j++)
                                {
                                        v1[i][j].v = v;
                                        v1[i][j].c2=c2;
                                }
        }

        if(name[0] != 0)
                printf("    Memory allocated for %s\n", name);

        return(v1);
}

ndv2 **init_arrNDV2(int n1, int n2, double v, double c1, double c2, char *name)
```

```
{
        int i, j;
        ndv2 **v1;

        if ((v1 = (ndv2 **)malloc((n1)*sizeof(ndv2 *))) == NULL)
        {
                printf("Cannot allocate memory for %s\n", name);
                exit(1);
        }
        else
        {
                for(i=0; i<n1; i++)
                        if ((v1[i] = (ndv2 *)malloc((n2)*sizeof(ndv2))) == NULL)
                        {
                                printf("cannot allocate memory for %s\n", name);
                                exit(1);
                        }
                        else
                                for(j=0; j<n2; j++)
                                {
                                        v1[i][j].v = v;
                                        v1[i][j].c1=c1;
                                        v1[i][j].c2=c2;
                                }
        }

        if(name[0] != 0)
                printf("    Memory allocated for %s\n", name);

        return(v1);
}

void header(char *n1, char *n2, int n)
{
```

```
	if(!strstr(n1, n2))
	{
		printf("!!! Need info about %s as input %d !!!", n2, n);
		exit(1);
	}
}

void init()
{
	hz = init_arrD(nx, ny, 0.0, "hz");
	ex = init_arrNDV1(nx, ny+1, 0.0, 0.0, "ex");
	ey = init_arrNDV1(nx+1, ny, 0.0, 0.0, "ey");
	jx = init_arrNDV2(nx, ny+1, 0.0, 0.0, 0.0, "jx");
	jy = init_arrNDV2(nx+1, ny, 0.0, 0.0, 0.0, "jy");
	Ae = init_arrD(nx, ny, 0.0, "Ae");
}

void ParaRead()
{
	char lnstr[MAX_char];
	int i,j;
	//double val;

	ifstream FileObj(file1);
	if (FileObj == NULL)
	{
		printf("!!! File Not Found !!!");
		exit(1);
	}

	FileObj.getline(lnstr,MAX_char);
	header(lnstr, "### OPT", 0);
	if(!sscanf(lnstr, "%*s %*s %d %d %d", &opt1, &opt2, &opt3))
	{	printf("!!! ERROR reading Output Options !!!");
```

```
		exit(1);
	}

	//Output Options:
	// opt1:		0: pulse		1: plane wave
	// opt2:	0: ex(t)		1: Ae
	// opt3:		OPT_FREQ				MAX_ITER-2*ntpd

	FileObj.getline(lnstr,MAX_char);
	if (!strstr(lnstr, "### NAME"))
		exit(1);
	sscanf(lnstr, "%*s %*s %[]s", name);

	FileObj.getline(lnstr,MAX_char);
	header(lnstr, "### LAMBDA", 2);
	if(!sscanf(lnstr, "%*s %*s %lf", &LAMBDA))
	{	printf("!!! ERROR reading LAMBDA !!!");
		exit(1);
	}
	FREQ=C0/LAMBDA;

	FileObj.getline(lnstr,MAX_char);
	header(lnstr, "### NX", 3);
	if(!sscanf(lnstr, "%*s %*s %d", &nx))
	{	printf("!!! ERROR reading NX !!!");
		exit(1);
	}

	FileObj.getline(lnstr,MAX_char);
	header(lnstr, "### NY", 4);
	if(!sscanf(lnstr, "%*s %*s %d", &ny))
	{	printf("!!! ERROR reading NY !!!");
		exit(1);
	}
```

```
FileObj.getline(lnstr,MAX_char);
header(lnstr, "### MAX_N", 5);
if(!sscanf(lnstr, "%*s %*s %d", &MAX_N))
{           printf("!!! ERROR reading MAX_N !!!");
            exit(1);
}

FileObj.getline(lnstr,MAX_char);
header(lnstr, "### OPT_FQ", 6);
if(!sscanf(lnstr, "%*s %*s %d", &OPT_FQ))
{           printf("!!! ERROR reading OPT_FQ !!!");
            exit(1);
}

FileObj.getline(lnstr,MAX_char);
header(lnstr, "### CELLS_PER_WL", 7);
if(!sscanf(lnstr, "%*s %*s %d", &CELLS_PER_WL))
{           printf("!!! ERROR reading CELLS_PER_WL !!!");
            exit(1);
}

FileObj.getline(lnstr,MAX_char);
header(lnstr, "### DX", 8);
if(!sscanf(lnstr, "%*s %*s %lf", &dx))
{           printf("!!! ERROR reading DX !!!");
            exit(1);
}

dt=dx/2/C0;
ntpd=int(2*C0/FREQ/dx);

init();
```

```
FileObj.getline(lnstr,MAX_char);
header(lnstr, "### CEXB", 9);
for(i=0; i<nx; i++)
        for(j=0; j<ny+1; j++)
        {       if(!(FileObj>>ex[i][j].c2))
                {       printf("!!! Error reading CEXB !!!");
                        exit(1);
                }
        }

FileObj.getline(lnstr,MAX_char);
FileObj.getline(lnstr,MAX_char);
header(lnstr, "### CEYB", 10);
for(i=0; i<nx+1; i++)
        for(j=0; j<ny; j++)
        {       if(!(FileObj>>ey[i][j].c2))
                {       printf("!!! Error reading CEYB !!!");
                        exit(1);
                }
        }

FileObj.getline(lnstr,MAX_char);
FileObj.getline(lnstr,MAX_char);
header(lnstr, "### CJXA", 11);
for(i=0; i<nx; i++)
        for(j=0; j<ny+1; j++)
        {       if(!(FileObj>>jx[i][j].c1))
                {       printf("!!! Error reading CJXA !!!");
                        exit(1);
                }
        }

FileObj.getline(lnstr,MAX_char);
FileObj.getline(lnstr,MAX_char);
```

```
	header(lnstr, "### CJXB", 12);
	for(i=0; i<nx; i++)
		for(j=0; j<ny+1; j++)
		{	if(!(FileObj>>jx[i][j].c2))
			{	printf("!!! Error reading CJXB !!!");
				exit(1);
			}
		}

	FileObj.getline(lnstr,MAX_char);
	FileObj.getline(lnstr,MAX_char);
	header(lnstr, "### CJYA", 13);
	for(i=0; i<nx+1; i++)
		for(j=0; j<ny; j++)
		{	if(!(FileObj>>jy[i][j].c1))
			{	printf("!!! Error reading CJYA !!!");
				exit(1);
			}
		}

	FileObj.getline(lnstr,MAX_char);
	FileObj.getline(lnstr,MAX_char);
	header(lnstr, "### CJYB", 14);
	for(i=0; i<nx+1; i++)
		for(j=0; j<ny; j++)
		{	if(!(FileObj>>jy[i][j].c2))
			{	printf("!!! Error reading CJYB !!!");
				exit(1);
			}
		}

	FileObj.close();
}
```

```
void freeall()
{
            free(hz);
            free(ex);
            free(jx);
            free(ey);
            free(jy);
            free(Ae);
            free(hzxF);
            free(hzyF);
            free(exF);
            free(eyF);
            free(hzxB);
            free(hzyB);
            free(exB);
            free(eyB);
            free(hzxL);
            free(hzyL);
            free(exL);
            free(eyL);
            free(hzxR);
            free(hzyR);
            free(exR);
            free(eyR);
}

double Fcexa(int i, int j)
{
            if ((j==0) | (j==ny))
                        return CA;
            else
      return 1.;
}
```

```
double Fceya(int i, int j)
{
        if ((i==0) | (i==nx))
                return CA;
        else
    return 1.;
}

void PML_Coeff()
{
        double thk, sigm, sigy, sigy2, sigx, sigx2, eafh, eafe, ca1, cb1;
        int i, j;

        thk=nPML*dx;
        sigm=-log(PML_max)*EPS0*C0*(PML_odr+1)/2/thk;

//Front region
        for (i=1; i<=nPML; i++)
        {
                sigy=sigm*pow((i-.5)*dx/thk, PML_odr);
                sigy2=sigy*MU0/EPS0;
                eafh=sigy2*dt/2/MU0;
                for (j=1; j<=nx+2*nPML; j++)
                {
                        hzyF[j-1][nPML-i].c1=(1-eafh)/(1+eafh);
                        hzyF[j-1][nPML-i].c2=.5/(1+eafh);
                }
                sigy=sigm*pow(i*dx/thk, PML_odr);
                eafe=sigy*dt/2/EPS0;
                for (j=1; j<=nx+2*nPML; j++)
                {
                        exF[j-1][nPML-i].c1=(1-eafe)/(1+eafe);
                        exF[j-1][nPML-i].c2=.5/(1+eafe);
```

```
		}
	}

//Back region
	for (i=1; i<=nPML; i++)
	{
		sigy=sigm*pow((i-.5)*dx/thk, PML_odr);
		sigy2=sigy*MU0/EPS0;
		eafh=sigy2*dt/2/MU0;
		for (j=1; j<=nx+2*nPML; j++)
		{
			hzyB[j-1][i-1].c1=(1-eafh)/(1+eafh);
			hzyB[j-1][i-1].c2=.5/(1+eafh);
		}
		sigy=sigm*pow(i*dx/thk, PML_odr);
		eafe=sigy*dt/2/EPS0;
		for (j=1; j<=nx+2*nPML; j++)
		{
			exB[j-1][i-1].c1=(1-eafe)/(1+eafe);
			exB[j-1][i-1].c2=.5/(1+eafe);
		}
	}

//Left region
	for (i=1; i<=nPML; i++)
	{
		sigx=sigm*pow((i-.5)*dx/thk, PML_odr);
		sigx2=sigx*MU0/EPS0;
		eafh=sigx2*dt/2/MU0;
		ca1=(1-eafh)/(1+eafh);
		cb1=.5/(1+eafh);
		for (j=1; j<=ny; j++)
		{
			hzxL[nPML-i][j-1].c1=ca1;
```

```
                    hzxL[nPML-i][j-1].c2=cb1;
                }
                for (j=1; j<=nPML; j++)
                {
                    hzxF[nPML-i][j-1].c1=ca1;
                    hzxF[nPML-i][j-1].c2=cb1;
                    hzxB[nPML-i][j-1].c1=ca1;
                    hzxB[nPML-i][j-1].c2=cb1;
                }

                sigx=sigm*pow(i*dx/thk, PML_odr);
                eafe=sigx*dt/2/EPS0;
                ca1=(1-eafe)/(1+eafe);
                cb1=.5/(1+eafe);
                for (j=1; j<=ny; j++)
                {
                    eyL[nPML-i][j-1].c1=ca1;
                    eyL[nPML-i][j-1].c2=cb1;
                }
                for (j=1; j<=nPML; j++)
                {
                    eyF[nPML-i][j-1].c1=ca1;
                    eyF[nPML-i][j-1].c2=cb1;
                    eyB[nPML-i][j-1].c1=ca1;
                    eyB[nPML-i][j-1].c2=cb1;
                }
            }

//Right region
   for (i=1; i<=nPML; i++)
        {
                sigx=sigm*pow((i-.5)*dx/thk, PML_odr);
                sigx2=sigx*MU0/EPS0;
                eafh=sigx2*dt/2/MU0;
```

```
ca1=(1-eafh)/(1+eafh);
cb1=.5/(1+eafh);
            for (j=1; j<=ny; j++)
            {
                    hzxR[i-1][j-1].c1=ca1;
                    hzxR[i-1][j-1].c2=cb1;
            }
            for (j=1; j<=nPML; j++)
            {
                    hzxF[nx+nPML+i-1][j-1].c1=ca1;
                    hzxF[nx+nPML+i-1][j-1].c2=cb1;
                    hzxB[nx+nPML+i-1][j-1].c1=ca1;
                    hzxB[nx+nPML+i-1][j-1].c2=cb1;
            }

            sigx=sigm*pow(i*dx/thk, PML_odr);
            eafe=sigx*dt/2/EPS0;
            ca1=(1-eafe)/(1+eafe);
cb1=.5/(1+eafe);
for (j=1; j<=ny; j++)
            {
                    eyR[i-1][j-1].c1=ca1;
                    eyR[i-1][j-1].c2=cb1;
            }
            for (j=1; j<=nPML; j++)
            {
                    eyF[nx+nPML+i][j-1].c1=ca1;
                    eyF[nx+nPML+i][j-1].c2=cb1;
                    eyB[nx+nPML+i][j-1].c1=ca1;
                    eyB[nx+nPML+i][j-1].c2=cb1;
            }
    }

    //WHY cexL and cexR is not updated??????
```

```
//Interface
sigy=sigm*pow(PML_itf*dx/thk, PML_odr);
eafe=sigy*dt/2/EPS0;
ca1=(1-eafe)/(1+eafe);
cb1=.5/(1+eafe);
CA=ca1;

for (j=1; j<=nx; j++)
        ex[j-1][0].c2=cb1;
for (j=1; j<=nPML; j++)
{
        exL[j-1][0].c1=ca1;
        exL[j-1][0].c2=cb1;
        exR[j-1][0].c1=ca1;
        exR[j-1][0].c2=cb1;
}

//cex1[][ny]=ca1;
for (j=1; j<=nx; j++)
        ex[j-1][ny].c2=cb1;
for (j=1; j<=nPML; j++)
{
        exL[j-1][ny].c1=ca1;
        exL[j-1][ny].c2=cb1;
        exR[j-1][ny].c1=ca1;
        exR[j-1][ny].c2=cb1;
}

//cey1[0][]=ca1;
for (j=1; j<=ny; j++)
        ey[0][j-1].c2=cb1;
for (j=1; j<=nPML; j++)
{
```

```
			eyF[nPML][j-1].c1=ca1;
			eyF[nPML][j-1].c2=cb1;
			eyB[nPML][j-1].c1=ca1;
			eyB[nPML][j-1].c2=cb1;
		}

		//cey1[nx][]=ca1;
		for (j=1; j<=ny; j++)
			ey[nx][j-1].c2=cb1;
		for (j=1; j<=nPML; j++)
		{
			eyF[nPML+nx][j-1].c1=ca1;
			eyF[nPML+nx][j-1].c2=cb1;
			eyB[nPML+nx][j-1].c1=ca1;
			eyB[nPML+nx][j-1].c2=cb1;
		}

}

void main()
{
	printf("==========================================================\n");
	printf("Generalized FDTD solver using Drude model\n");
	printf("2D, TE mode, PML implemented\n");
//	printf("For dielectric material and metal\n");
	printf("To study near-field enhancement effect\n");
	printf("By Dongbing, Dec 2003\n, Version 2.0");
//	printf("Version 2.0, changes made in Ae calculation\n");
	printf("==========================================================\n");
	printf("\n\n");

	int i, j, npct, n, ia, ib, ja, jb;
	double *hz1, *ex1, hz1e1[2]={0., 0.}, hz1e2[2]={0., 0.}, ct, pulse, pfq, tmpx, tmpy, tmp;
	char tmpbuf[128];
```

```
	//Read Parameters
	ParaRead();

	//Initialize arrays
	hz1 = (double *)malloc((ny)*sizeof(double));
	for (i=0; i<ny; i++)
		hz1[i]=0.0;
	ex1 = (double *)malloc((ny+1)*sizeof(double));
	for (i=0; i<ny+1; i++)
		ex1[i]=0.0;

	//Total and Scattered Field
	ia=TTSC;
	ib=nx-ia+1;
	ja=TTSC;
	jb=ny-ja+1;

//PML
	hzxF = init_arrNDV2(nx+2*nPML, nPML, 0.0, 1., .5, "");
	hzyF = init_arrNDV2(nx+2*nPML, nPML, 0.0, 1., .5, "");
	exF  = init_arrNDV2(nx+2*nPML, nPML, 0.0, 1., .5, "");
	eyF  = init_arrNDV2(nx+2*nPML+1, nPML, 0.0, 1., .5, "F_PML");

	hzxB = init_arrNDV2(nx+2*nPML, nPML, 0.0, 1., .5, "");
	hzyB = init_arrNDV2(nx+2*nPML, nPML, 0.0, 1., .5, "");
	exB  = init_arrNDV2(nx+2*nPML, nPML, 0.0, 1., .5, "");
	eyB  = init_arrNDV2(nx+2*nPML+1, nPML, 0.0, 1., .5, "B_PML");

	hzxL = init_arrNDV2(nPML, ny, 0.0, 1., .5, "");
	hzyL = init_arrNDV2(nPML, ny, 0.0, 1., .5, "");
	exL  = init_arrNDV2(nPML, ny+1, 0.0, 1., .5, "");
	eyL  = init_arrNDV2(nPML, ny, 0.0, 1., .5, "L_PML");
```

```
            hzxR = init_arrNDV2(nPML, ny, 0.0, 1., .5, "");
            hzyR = init_arrNDV2(nPML, ny, 0.0, 1., .5, "");
            exR  = init_arrNDV2(nPML, ny+1, 0.0, 1., .5, "");
            eyR  = init_arrNDV2(nPML, ny, 0.0, 1., .5, "R_PML");


            PML_Coeff();

            //_tzset();

   /* Display operating system-style date and time. */
   _strtime( tmpbuf );

            npct=1;
            printf("\n\nMain Updating Loop\n");
            printf("    started at \t\t%s\n", tmpbuf );
            pfq=C0/((ny/2)*dx/2.5);


//Main Updating Loop
            for (n=1; n<=MAX_N; n++)
            {
                        ct=n*dt;
                        if (n*100/MAX_N > npct)
                        {
                                    printf("%c%c%c%c%c%c%c%c%c%c%c%c%c", 8, 8, 8, 8, 8, 8, 8, 8, 8, 8, 8, 8, 8);
                                    printf("%2d%% completed", npct);
                                    npct=npct+1;
                        }

                        //plane wave buffer, ex1         TTSC
                        for (i=1; i<=ny-1; i++)
                                    ex1[i]=ex1[i]+.5*(hz1[i]-hz1[i-1]);
```

```
//ex in main grid
for (i=0; i<=nx-1; i++)       {
            for (j=1; j<=ny-1; j++)
                        ex[i][j] += (hz[i][j]-hz[i][j-1]-dx*jx[i][j].v);
}

//incident ex        TTSC
if (opt1 == 1) {
            for (i=ia; i<=ib; i++) {
                        ex[i-1][ja-1].v=ex[i-1][ja-1].v+.5*hz1[ja-1];
                        ex[i-1][jb].v=ex[i-1][jb].v-0.5*hz1[jb-1];
            }
}

//ey in main grid
for(i=1; i<=nx-1; i++) {
            for (j=0; j<=ny-1; j++)
                        ey[i][j] += (hz[i-1][j]-hz[i][j]-dx*jy[i][j].v);
}

//incident ey        TTSC
if (opt1 == 1) {
            for (j=ja; j<=jb; j++) {
                        ey[ia-1][j-1].v=ey[ia-1][j-1].v-0.5*hz1[j-1];
                        ey[ib][j-1].v=ey[ib][j-1].v+0.5*hz1[j-1];
            }
}

//ex in PML
//   FRONT
for (i=0; i<=nx+2*nPML-1; i++)
{
            for (j=1; j<=nPML-1; j++)
                        exF[i][j] += (-hzxF[i][j-1].v+hzxF[i][j].v-hzyF[i][j-1].v+hzyF[i][j].v);
```

```
}
for (i=0; i<=nx-1; i++)
    ex[i][0] += (-hzxF[nPML+i][nPML-1].v-hzyF[nPML+i][nPML-1].v+hz[i][0]);

//  BACK
for (i=0; i<=nx+2*nPML-1; i++)
{
    for (j=0; j<=nPML-2; j++)
        exB[i][j] += (-hzxB[i][j].v+hzxB[i][j+1].v-hzyB[i][j].v+hzyB[i][j+1].v);
}
for (i=0; i<=nx-1; i++)
    ex[i][ny] += (-hz[i][ny-1]+hzxB[nPML+i][0].v+hzyB[nPML+i][0].v);

//  LEFT
for (i=0; i<=nPML-1; i++) {
    for (j=1; j<=ny-1; j++)
        exL[i][j] += (-hzxL[i][j-1].v+hzxL[i][j].v-hzyL[i][j-1].v+hzyL[i][j].v);
    exL[i][0] += (-hzxF[i][nPML-1].v+hzxL[i][0].v-hzyF[i][nPML-1].v+hzyL[i][0].v);
    exL[i][ny] += (-hzxL[i][ny-1].v+hzxB[i][0].v-hzyL[i][ny-1].v+hzyB[i][0].v);
}

//  RIGHT
for (i=0; i<=nPML-1; i++)
{
    for (j=1; j<=ny-1; j++)
        exR[i][j] += (-hzxR[i][j-1].v+hzxR[i][j].v-hzyR[i][j-1].v+hzyR[i][j].v);
    exR[i][0] += (-hzxF[nx+nPML+i][nPML-1].v+hzxR[i][0].v-hzyF[nx+nPML+i][nPML-1].v+hzyR[i][0].v);
    exR[i][ny] += (-hzxR[i][ny-1].v+hzxB[nx+nPML+i][0].v-hzyR[i][ny-1].v+hzyB[nx+nPML+i][0].v);
}

//ey in PML
//  FRONT
for (i=1; i<=nx+2*nPML-1; i++) {
```

```
        for (j=0; j<=nPML-1; j++)
                eyF[i][j] += (-hzxF[i][j].v+hzxF[i-1][j].v-hzyF[i][j].v+hzyF[i-1][j].v);
}

//   BACK
for (i=1; i<=nx+2*nPML-1; i++) {
        for (j=0; j<=nPML-1; j++)
                eyB[i][j] += (-hzxB[i][j].v+hzxB[i-1][j].v-hzyB[i][j].v+hzyB[i-1][j].v);
}

//   LEFT
for (i=1; i<=nPML-1; i++) {
        for (j=0; j<=ny-1; j++)
                eyL[i][j] += (-hzxL[i][j].v+hzxL[i-1][j].v-hzyL[i][j].v+hzyL[i-1][j].v);
}
for (j=0; j<=ny-1; j++)
        ey[0][j] += (-hz[0][j]+hzxL[nPML-1][j].v+hzyL[nPML-1][j].v);

//   RIGHT
for (i=0; i<=nPML-2; i++) {
        for (j=0; j<=ny-1; j++)
                eyR[i][j] += (-hzxR[i+1][j].v+hzxR[i][j].v-hzyR[i+1][j].v+hzyR[i][j].v);
}
for (j=0; j<=ny-1; j++)
        ey[nx][j] += (-hzxR[0][j].v-hzyR[0][j].v+hz[nx-1][j]);

//Plane wave buffer, hz1        TTSC
for (i=0; i<=ny-1; i++)
        hz1[i]=hz1[i]+.5*(ex1[i+1]-ex1[i]);

//ABC for plane wave buffer     TTSC
hz1[0]   = hz1e1[0];
hz1e1[0] = hz1e1[1];
hz1e1[1] = hz1[1];
```

```
hz1[ny-1] = hz1e2[0];
hz1e2[0]  = hz1e2[1];
hz1e2[1]  = hz1[ny-2];

//hz in main grid
for (i=0; i<=nx-1; i++) {
        for (j=0; j<=ny-1; j++)
                hz[i][j] += 0.5*(-ey[i+1][j].v+ey[i][j].v+ex[i][j+1].v-ex[i][j].v);
}

//a pulse in buffer          TTSC
if (opt1 == 1) {
        pulse=sin(2*PI*FREQ*ct);
        hz1[2]=pulse;                                           //hz1[2]+

        //Incident hz        TTSC
        for (i=ia-1; i<=ib-1; i++) {
                hz[i][ja-1] += .5*ex1[ja-1];
                hz[i][jb-1] -= .5*ex1[jb];
        }
}
else if (opt1 == 0) {
        //A pulse in the domain
        //pulse=20.*exp(-.5*pow((n-40)/12,2.));
        pulse=sin(2*PI*pfq*ct);
        hz[int(nx/2)][int(ny/2)] += pulse;
}

//hzX in PML
//   FRONT
for (i=0; i<=nx+2*nPML-1; i++) {
        for (j=0; j<=nPML-1; j++)
                hzxF[i][j] += (-eyF[i+1][j].v+eyF[i][j].v);
```

```
}

//   BACK
for (i=0; i<=nx+2*nPML-1; i++) {
        for (j=0; j<=nPML-1; j++)
                hzxB[i][j] += (-eyB[i+1][j].v+eyB[i][j].v);
}

//   LEFT
for (i=0; i<=nPML-2; i++) {
        for (j=0; j<=ny-1; j++)
                hzxL[i][j] += (-eyL[i+1][j].v+eyL[i][j].v);
}
for (j=0; j<=ny-1; j++)
        hzxL[nPML-1][j] += (-ey[0][j].v+eyL[nPML-1][j].v);

//   RIGHT
for (i=1; i<=nPML-1; i++) {
        for (j=0; j<=ny-1; j++)
                hzxR[i][j] += (-eyR[i][j].v+eyR[i-1][j].v);
}
for (j=0; j<=ny-1; j++)
        hzxR[0][j] += (-eyR[0][j].v+ey[nx][j].v);

//hzY in PML
//   FRONT nx+2*nPML, nPML
for (i=0; i<=nx+2*nPML-1; i++) {
        for (j=0; j<=nPML-2; j++)
                hzyF[i][j] += (-exF[i][j].v+exF[i][j+1].v);
}
for (i=0; i<=nPML-1; i++)
        hzyF[i][nPML-1] += (-exF[i][nPML-1].v+exL[i][0].v);
for (i=nPML; i<=nPML+nx-1; i++)
        hzyF[i][nPML-1] += (-exF[i][nPML-1].v+ex[i-nPML][0].v);
```

```
for (i=nPML+nx; i<=nx+2*nPML-1; i++)
        hzyF[i][nPML-1] += (-exF[i][nPML-1].v+exR[i-nPML-nx][0].v);

//   BACK nx+2*nPML, nPML
for (i=0; i<=nx+2*nPML-1; i++) {
        for (j=1; j<=nPML-1; j++)
                hzyB[i][j] += (-exB[i][j-1].v+exB[i][j].v);
}
for (i=0; i<=nPML-1; i++)
        hzyB[i][0] += (-exL[i][ny].v+exB[i][0].v);
for (i=nPML; i<=nPML+nx-1; i++)
        hzyB[i][0] += (-ex[i-nPML][ny].v+exB[i][0].v);
for (i=nPML+nx; i<=nx+2*nPML-1; i++)
        hzyB[i][0] += (-exR[i-nPML-nx][ny].v+exB[i][0].v);

//   LEFT   nPML, ny
for (i=0; i<=nPML-1; i++) {
        for (j=0; j<=ny-1; j++)
                hzyL[i][j] += (-exL[i][j].v+exL[i][j+1].v);
}

//RIGHT
for (i=0; i<=nPML-1; i++) {
        for (j=0; j<=ny-1; j++)
                hzyR[i][j] += (-exR[i][j].v+exR[i][j+1].v);
}

//Jx in main grid                nx, ny+1
for (i=0; i<=nx-1; i++) {
        for (j=0; j<=ny; j++)
                jx[i][j] += ex[i][j].v;
}

//Jy in main grid                nx+1, ny
```

```
for (i=0; i<=nx; i++) {
        for (j=0; j<=ny-1; j++)
                jy[i][j] += ey[i][j].v;
}

// opt2:       0: ex(t)                1: Ae
// opt3:            OPT_FREQ                              MAX_ITER-2*ntpd
if ((opt2 == 1) & (n>opt3)) {
        for (i=0; i<=nx-1; i++) {
                for (j=0; j<=ny-1; j++) {
                        tmpx=(ex[i][j].v+ex[i][j+1].v)/2;
                        tmpy=(ey[i][j].v+ey[i+1][j].v)/2;
                        tmp=sqrt(tmpx*tmpx+tmpy*tmpy);
                        if (tmp > Ae[i][j])
                                Ae[i][j] = tmp;
                }
        }
}
else if ((opt2 == 0) & (n-int(n/opt3)*opt3 == 0)) {
        //output ex
        sprintf(file2, "ex%d.txt", n);
        ofstream FileObj2(file2);
        if (FileObj2 == NULL) {
                printf("!!! Error exporting ex%d.txt !!!", n);
                exit(1);
        }
        for(i=0; i<nx; i++) {
                for(j=0; j<ny+1; j++)
                        //FileObj2 << ex[i][j].v << ' ';
                        FileObj2 << hz[i][j] << ' ';
                FileObj2<<'\n';
        }
        FileObj2.close();
}
```

```
	}
	//Main updating loop ends

	if (opt2 == 1) {
		//output Ae;
		sprintf(file2, "Ae.txt");
		ofstream FileObj2(file2);
		if (FileObj2 == NULL) {
			printf("!!! Error exporting Ae.txt !!!");
			exit(1);
		}
		for(i=0; i<nx; i++) {
			for(j=0; j<ny; j++)
				FileObj2 << ' ' << Ae[i][j];
			FileObj2<<'\n';
		}
		FileObj2.close();
	}

	_strtime( tmpbuf );
	printf("\n    ended at \t\t%s\n", tmpbuf );



	freeall();
}
```

Bibliography

Alkaisi, M. M., Blaikie, R. J., McNab, S. J., Cheung, R., Cumming, D. R. S., "Sub-diffraction-limited patterning using evanescent near-field optical lithography," *Applied Physics Letters*, **75**, pp.3560-3562 (1999).

Ambrose, W. P., Goodwin, P. M., Martin, J. C., Keller, R. A., "Single-Molecule Detection and Photochemistry on a Surface Using near-Field Optical-Excitation," *Physical Review Letters*, **72**, pp.160-163 (1994).

Barber, P. W., Hill, S. C., *Light scattering by particles : computational methods* (World Scientific, Singapore ; Teaneck, N.J., 1990).

Barnes, W. L., Dereux, A., Ebbesen, T. W., "Surface plasmon subwavelength optics," *Nature*, **424**, pp.824-830 (2003).

Barnes, W. L., Murray, W. A., Dintinger, J., Devaux, E., Ebbesen, T. W., "Surface plasmon polaritons and their role in the enhanced transmission of light through periodic arrays of subwavelength holes in a metal film," *Physical Review Letters*, **92**, pp.- (2004).

Bass, M., *Laser materials processing* (North-Holland; New York, N.Y., 1983).

Berenger, J. P., "A Perfectly Matched Layer for the Absorption of Electromagnetic-Waves," *Journal of Computational Physics*, **114**, pp.185-200 (1994).

Berkowitz, B., *Basic microwaves* (Hayden Book Co., New York,, 1966).

Betzig, E., Trautman, J. K., "Near-Field Optics - Microscopy, Spectroscopy, and Surface Modification Beyond the Diffraction Limit," *Science*, **257**, pp.189-195 (1992).

Betzig, E., Trautman, J. K., Wolfe, R., Gyorgy, E. M., Finn, P. L., Kryder, M. H., Chang, C. H., "Near-Field Magnetooptics and High-Density Data-Storage," *Applied Physics Letters*, **61**, pp.142-144 (1992).

Betzig, E., Chichester, R. J., "Single Molecules Observed by near-Field Scanning Optical Microscopy," *Science*, **262**, pp.1422-1425 (1993).

Binnig, G., Rohrer, H., Gerber, C., Weibel, E., "Tunneling through a Controllable Vacuum Gap," *Applied Physics Letters*, **40**, pp.178-180 (1982).

Binnig, G., Rohrer, H., Gerber, C., Weibel, E., "7x7 Reconstruction on Si(111) Resolved in Real Space," *Physical Review Letters*, **50**, pp.120-123 (1983).

Binnig, G., Frank, K. H., Fuchs, H., Garcia, N., Reihl, B., Rohrer, H., Salvan, F., Williams, A. R., "Tunneling Spectroscopy and Inverse Photoemission - Image and Field States," *Physical Review Letters*, **55**, pp.991-994 (1985).

Blanco, A., Chomski, E., Grabtchak, S., Ibisate, M., John, S., Leonard, S. W., Lopez, C., Meseguer, F., Miguez, H., Mondia, J. P., Ozin, G. A., Toader, O., van Driel, H. M., "Large-scale synthesis of a silicon photonic crystal with a complete three-dimensional bandgap near 1.5 micrometres," *Nature*, **405**, pp.437-440 (2000).

Born, M., Wolf, E., *Principles of optics : electromagnetic theory of propagation, interference and diffraction of light* (Cambridge University Press, New York, ed. 7th expanded, 1999).

Boyd, I. W., *Laser processing of thin films and microstructures : oxidation, deposition, and etching of insulators* (Springer-Verlag, Berlin ; New York, 1987).

Campbell, M., Sharp, D. N., Harrison, M. T., Denning, R. G., Turberfield, A. J., "Fabrication of photonic crystals for the visible spectrum by holographic lithography," *Nature*, **404**, pp.53-56 (2000).

Chimmalgi, A., Choi, T. Y., Grigoropoulos, C. P., Komvopoulos, K., "Femtosecond laser aperturless near-field nanomachining of metals assisted by scanning probe microscopy," *Applied Physics Letters*, **82**, pp.1146-1148 (2003).

Collin, S., Pardo, F., Teissier, R., Pelouard, J. L., "Strong discontinuities in the complex photonic band structure of transmission metallic gratings," *Physical Review B*, **63**, (2001).

Collin, S., Pardo, F., Teissier, R., Pelouard, J. L., "Horizontal and vertical surface resonances in transmission metallic gratings," *Journal of Optics a-Pure and Applied Optics*, **4**, pp.S154-S160 (2002).

Cooper, E. B., Manalis, S. R., Fang, H., Dai, H., Matsumoto, K., Minne, S. C., Hunt, T., Quate, C. F., "Terabit-per-square-inch data storage with the atomic force microscope," *Applied Physics Letters*, **75**, pp.3566-3568 (1999).

Cubukcu, E., Aydin, K., Ozbay, E., Foteinopoulou, S., Soukoulis, C. M., "Negative refraction by photonic crystals," *Nature*, **423**, pp.604-605 (2003).

Deubel, M., Von Freymann, G., Wegener, M., Pereira, S., Busch, K., Soukoulis, C. M., "Direct laser writing of three-dimensional photonic-crystal templates for telecommunications," *Nature Materials*, **3**, pp.444-447 (2004).

Ebbesen, T. W., Lezec, H. J., Ghaemi, H. F., Thio, T., Wolff, P. A., "Extraordinary optical transmission through sub-wavelength hole arrays," *Nature*, **391**, pp.667-669 (1998).

Fan, S. H., Villeneuve, P. R., Joannopoulos, J. D., Schubert, E. F., "High extraction efficiency of spontaneous emission from slabs of photonic crystals," *Physical Review Letters*, **78**, pp.3294-3297 (1997).

Foresi, J. S., Villeneuve, P. R., Ferrera, J., Thoen, E. R., Steinmeyer, G., Fan, S., Joannopoulos, J. D., Kimerling, L. C., Smith, H. I., Ippen, E. P., "Photonic-bandgap microcavities in optical waveguides," *Nature*, **390**, pp.143-145 (1997).

Frey, H. G., Witt, S., Felderer, K., Guckenberger, R., "High-resolution imaging of single fluorescent molecules with the optical near-field of a metal tip," *Physical Review Letters*, **93**, pp.- (2004).

Gerton, J. M., Wade, L. A., Lessard, G. A., Ma, Z., Quake, S. R., "Tip-enhanced fluorescence microscopy at 10 nanometer resolution," *Physical Review Letters*, **93**, pp.- (2004).

Ghaemi, H. F., Thio, T., Grupp, D. E., Ebbesen, T. W., Lezec, H. J., "Surface plasmons enhance optical transmission through subwavelength holes," *Physical Review B*, **58**, pp.6779-6782 (1998).

Goodberlet, J. G., Kavak, H., "Patterning Sub-50 nm features with near-field embedded-amplitude masks," *Applied Physics Letters*, **81**, pp.1315-1317 (2002).

Gorbunov, A. A., Pompe, W., "Thin-Film Nanoprocessing by Laser Stm Combination," *Physica Status Solidi a-Applied Research*, **145**, pp.333-338 (1994).

Gray, S. K., Kupka, T., "Propagation of light in metallic nanowire arrays: Finite-difference time-domain studies of silver cylinders," *Physical Review B*, **68**, pp.- (2003).

H'dhili, F., Bachelot, R., Lerondel, G., Barchiesi, D., Royer, P., "Near-field optics: Direct observation of the field enhancement below an apertureless probe using a photosensitive polymer," *Applied Physics Letters*, **79**, pp.4019-4021 (2001).

Haefliger, D., Plitzko, J. M., Hillenbrand, R., "Contrast and scattering efficiency of scattering-type near-field optical probes," *Applied Physics Letters*, **85**, pp.4466-4468 (2004).

Hafner, C., *The generalized multipole technique for computational electromagnetics* (Artech House, Boston, 1990).

Ho, K. M., Chan, C. T., Soukoulis, C. M., Biswas, R., Sigalas, M., "Photonic Band-Gaps in 3-Dimensions - New Layer-by-Layer Periodic Structures," *Solid State Communications*, **89**, pp.413-416 (1994).

Jeon, S., Park, J. U., Cirelli, R., Yang, S., Heitzman, C. E., Braun, P. V., Kenis, P. J. A., Rogers, J. A., "Fabricating complex three-dimensional nanostructures with high-resolution conformable phase masks," *Proceedings of the National Academy of Sciences of the United States of America*, **101**, pp.12428-12433 (2004).

Jersch, J., Dickmann, K., "Nanostructure fabrication using laser field enhancement in the near field of a scanning tunneling microscope tip," *Applied Physics Letters*, **68**, pp.868-870 (1996).

John, S., "Strong Localization of Photons in Certain Disordered Dielectric Superlattices," *Physical Review Letters*, **58**, pp.2486-2489 (1987).

John, S., Wang, J., "Quantum Optics of Localized Light in a Photonic Band-Gap," *Physical Review B*, **43**, pp.12772-12789 (1991).

Kawata, S., Sun, H. B., Tanaka, T., Takada, K., "Finer features for functional microdevices - Micromachines can be created with higher resolution using two-photon absorption.," *Nature*, **412**, pp.697-698 (2001).

Kerker, M., *The scattering of light, and other electromagnetic radiation* (Academic Press, New York,, 1969).

Kraus, J. D., *Antennas* (McGraw-Hill, New York,, ed. 1st, 1950).

Krug, J. T., Sanchez, E. J., Xie, X. S., "Design of near-field optical probes with optimal field enhancement by finite difference time domain electromagnetic simulation," *Journal of Chemical Physics*, **116**, pp.10895-10901 (2002).

Kunz, K. S., Luebbers, R. J., *The finite difference time domain method for electromagnetics* (CRC Press, Boca Raton, 1993).

Kunz, R. R., Rothschild, M., Yeung, M. S., "Large-area patterning of similar to 50 nm structures on flexible substrates using near-field 193 nm radiation," *Journal of Vacuum Science & Technology B*, **21**, pp.78-81 (2003).

Lin, S. Y., Fleming, J. G., Hetherington, D. L., Smith, B. K., Biswas, R., Ho, K. M., Sigalas, M. M., Zubrzycki, W., Kurtz, S. R., Bur, J., "A three-dimensional photonic crystal operating at infrared wavelengths," *Nature*, **394**, pp.251-253 (1998).

Lin, S. Y., Chow, E., Hietala, V., Villeneuve, P. R., Joannopoulos, J. D., "Experimental demonstration of guiding and bending of electromagnetic waves in a photonic crystal," *Science*, **282**, pp.274-276 (1998).

Lu, Y., Theppakuttai, S., Chen, S. C., "Marangoni effect in nanosphere-enhanced laser nanopatterning of silicon," *Applied Physics Letters*, **82**, pp.4143-4145 (2003).

Luo, X. G., Ishihara, T., "Surface plasmon resonant interference nanolithography technique," *Applied Physics Letters*, **84**, pp.4780-4782 (2004).

Lynch, D. R., Paulsen, K. D., "Origin of Vector Parasites in Numerical Maxwell Solutions," *Ieee Transactions on Microwave Theory and Techniques*, **39**, pp.383-394 (1991).

Madou, M. J., *Fundamentals of microfabrication : the science of miniaturization* (CRC Press, Boca Raton, Fla., ed. 2nd, 2002).

Martin, O. J. F., Girard, C., "Controlling and tuning strong optical field gradients at a local probe microscope tip apex," *Applied Physics Letters*, **70**, pp.705-707 (1997).

Martin-Moreno, L., Garcia-Vidal, F. J., Lezec, H. J., Pellerin, K. M., Thio, T., Pendry, J. B., Ebbesen, T. W., "Theory of extraordinary optical transmission through subwavelength hole arrays," *Physical Review Letters*, **86**, pp.1114-1117 (2001).

Moharam, M. G., Gaylord, T. K., "Diffraction Analysis of Dielectric Surface-Relief Gratings," *Journal of the Optical Society of America*, **72**, pp.1385-1392 (1982).

Munzer, H. J., Mosbacher, M., Bertsch, M., Zimmermann, J., Leiderer, P., Boneberg, J., "Local held enhancement effects for nanostructuring of surfaces," *Journal of Microscopy-Oxford*, **202**, pp.129-135 (2001).

Novotny, L., Pohl, D. W., Hecht, B., "Scanning near-Field Optical Probe with Ultrasmall Spot Size," *Optics Letters*, **20**, pp.970-972 (1995).

Novotny, L., Bian, R. X., Xie, X. S., "Theory of nanometric optical tweezers," *Physical Review Letters*, **79**, pp.645-648 (1997).

Palik, E. D., *Handbook of optical constants of solids*, Academic Press handbook series. (Academic Press, Orlando, 1985).

Parimi, P. V., Lu, W. T. T., Vodo, P., Sridhar, S., "Photonic crystals - Imaging by flat lens using negative refraction," *Nature*, **426**, pp.404-404 (2003).

Paulsen, K. D., Lynch, D. R., "Elimination of Vector Parasites in Finite-Element Maxwell Solutions," *Ieee Transactions on Microwave Theory and Techniques*, **39**, pp.395-404 (1991).

Pendry, J., "Applied physics - Playing tricks with light," *Science*, **285**, pp.1687-1688 (1999).

Pohl, D. W., Denk, W., Lanz, M., "Optical Stethoscopy - Image Recording with Resolution Lambda/20," *Applied Physics Letters*, **44**, pp.651-653 (1984).

Popov, E., Neviere, M., Enoch, S., Reinisch, R., "Theory of light transmission through subwavelength periodic hole arrays," *Physical Review B*, **62**, pp.16100-16108 (2000).

Qi, M. H., Lidorikis, E., Rakich, P. T., Johnson, S. G., Joannopoulos, J. D., Ippen, E. P., Smith, H. I., "A three-dimensional optical photonic crystal with designed point defects," *Nature*, **429**, pp.538-542 (2004).

Raether, H., *Surface plasmons on smooth and rough surfaces and on gratings*, Springer tracts in modern physics ; 111. (Springer-Verlag, Berlin ; New York, 1988).

Sanchez, E. J., Novotny, L., Xie, X. S., "Near-field fluorescence microscopy based on two-photon excitation with metal tips," *Physical Review Letters*, **82**, pp.4014-4017 (1999).

Schmid, H., Biebuyck, H., Michel, B., Martin, O. J. F., "Light-coupling masks for lensless, sub-wavelength optical lithography," *Applied Physics Letters*, **72**, pp.2379-2381 (1998).

Shalaev, V. M., Cai, W. S., Chettiar, U. K., Yuan, H. K., Sarychev, A. K., Drachev, V. P., Kildishev, A. V., "Negative index of refraction in optical metamaterials," *Optics Letters*, **30**, pp.3356-3358 (2005).

Shao, D. B., Chen, S. C., "Surface-plasmon-assisted nanoscale photolithography by polarized light," *Applied Physics Letters*, **86**, pp.- (2005).

Shi, L., Plyasunov, S., Bachtold, A., McEuen, P. L., Majumdar, A., "Scanning thermal microscopy of carbon nanotubes using batch-fabricated probes," *Applied Physics Letters*, **77**, pp.4295-4297 (2000).

Silva, T. J., Schultz, S., Weller, D., "Scanning near-Field Optical Microscope for the Imaging of Magnetic Domains in Optically Opaque Materials," *Applied Physics Letters*, **65**, pp.658-660 (1994).

Sozuer, H. S., Haus, J. W., Inguva, R., "Photonic Bands - Convergence Problems with the Plane-Wave Method," *Physical Review B*, **45**, pp.13962-13972 (1992).

Srituravanich, W., Fang, N., Sun, C., Luo, Q., Zhang, X., "Plasmonic nanolithography," *Nano Letters*, **4**, pp.1085-1088 (2004).

Sullivan, D. M., IEEE Microwave Theory and Techniques Society., *Electromagnetic simulation using the FDTD method*, IEEE Press series on RF and microwave technology. (IEEE Press, New York, 2000).

Sun, W. X., Shen, Z. X., "Optimizing the near field around silver tips," *Journal of the Optical Society of America a-Optics Image Science and Vision*, **20**, pp.2254-2259 (2003).

Taflove, A., *Computational electrodynamics : the finite-difference time-domain method* (Artech House, Boston, 1995).

Tarun, A., Daza, M. R. H., Hayazawa, N., Inouye, Y., Kawata, S., "Apertureless optical near-field fabrication using an atomic force microscope on photoresists," *Applied Physics Letters*, **80**, pp.3400-3402 (2002).

Theppakuttai, S., Chen, S., "Nanoscale surface modification of glass using a 1064 nm pulsed laser," *Applied Physics Letters*, **83**, pp.758-760 (2003).

Wessel, J., "Surface-Enhanced Optical Microscopy," *Journal of the Optical Society of America B-Optical Physics*, **2**, pp.1538-1541 (1985).

Yablonovitch, E., "Inhibited Spontaneous Emission in Solid-State Physics and Electronics," *Physical Review Letters*, **58**, pp.2059-2062 (1987).

Yen, T. J., Padilla, W. J., Fang, N., Vier, D. C., Smith, D. R., Pendry, J. B., Basov, D. N., Zhang, X., "Terahertz magnetic response from artificial materials," *Science*, **303**, pp.1494-1496 (2004).

Yin, X. B., Fang, N., Zhang, X., Martini, I. B., Schwartz, B. J., "Near-field two-photon nanolithography using an apertureless optical probe," *Applied Physics Letters*, **81**, pp.3663-3665 (2002).

Zenhausern, F., Martin, Y., Wickramasinghe, H. K., "Scanning Interferometric Apertureless Microscopy - Optical Imaging at 10 Angstrom Resolution," *Science*, **269**, pp.1083-1085 (1995).

Vita

Dongbing Shao was born in Dongzhi County, Anhui Province, P. R. China on May 3rd, 1975, the son of Shiying Shao and Juzhen Zhao. After completing his education at the No.1 High School in Hefei City 1993, he enrolled in Engineering Mechanics Department of Tsinghua University in Beijing, China and received his degree of Bachelor of Engineering in June 1998. After spending two years of study in 501 Institute in Beijing, China, Dongbing decided to study abroad and attended The University of Colorado at Boulder from September 2000 to December 2002. In January 2003 he joined the Graduate School of The University of Texas at Austin for his PhD study. He married Xueqing Zhu in 2000 and their daughter, Carolyn Shao, came into their lives in 2005.

Permanent address: P.O.Box 208, Anhui Agriculture University, Hefei, Anhui, P. R. China 230036

This dissertation was typed by Dongbing Shao.